FISSION STUDIES WITH ^{252}CF: HALF-LIVES OF EXCITED STATES, ISOMERIC STRUCTURES IN ^{113,115,117}PD, AND NEUTRON MULTIPLICITIES

By

Dennis Ji-Bin Fong

Dissertation

submitted to the Faculty of the

graduate School of Vanderbilt University

in partial fulfillment of the requirements

for the degree of

DOCTOR OF PHILOSOPHY

in

Physics

May, 2005

Nashville, Tennessee

Approved:

Joseph H. Hamilton

Akunuri V. Ramayya

Senta Victoria Greene

Robert A. Knop Jr.

Sait A. Umar

To Caroline

ACKNOWLEDGEMENTS

My research has been aided at every step of the way by my advisors Dr. Joseph Hamilton and Dr. Akunuri Ramayya. Their experience and encouragement has been invaluable during the past four years. I'd like to thank them deeply for teaching me about physics and helping me get through my studies during graduate school.

I'd also like to extend my gratitude to Dr. Jae-Kwang Hwang for teaching me how to use our analysis software and discussing aspects of my research. Carol Soren has also been very helpful with keeping everything organized and running smoothly for experiments and analysis. My graduate committee, consisting of Dr. Umar, Dr. Greene, and Dr. Knop, has been helpful in advancing my progress towards my degree.

During my graduate studies, I was able to spend a lot of time at Oak Ridge National Laboratory to gain experience with electronics systems and detector development. I want to thank Dr. Krzysztof Rykaczewski for helping me with this and allowing me a great deal of hands-on training. Other people at ORNL who were very helpful to me were Robert Grzywacz, Chiara Mazzocchi, Noor Tantawy, and Jon Batchelder, among many others.

The support and motivation provided by my parents and sister have helped me through the years. Most importantly, I want to thank my wonderful future wife, Caroline Lim for always being there for me. None of this could have been possible without all of these people.

The work at Vanderbilt was supported in part by the U.S. Department of Energy under Grant No. DE-FG05-88ER40407. The Joint Institute for Heavy Ion Research at

ORNL is supported by the University of Tennessee, Vanderbilt University, ORNL, and the U.S. DOE under Contract No. DE-FG05-87ER40311.

TABLE OF CONTENTS

Page

DEDICATION ii

ACKNOWLEDGEMENTS iii

LIST OF TABLES viii

LIST OF FIGURES ix

Chapter

I. INTRODUCTION 1

II. EXPERIMENTAL TECHNIQUES 3

Introduction 3
Spontaneous fission of ^{252}Cf 4
Gamma ray detection 8
Gammasphere 9
Ternary fission 11
Experimental details 19
1995 binary fission at LBNL 19
2000 binary fission at LBNL 19
2001 ternary fission at LBNL 20
2005 binary and ternary fission at ANL 20
Experimental experience at ORNL 22
Double sided silicon strip detectors 22
Digital signal processing 23
Molecular ion beam purification 23
Ranging out gas cell 24

III. ANALYTICAL TECHNIQUES 26

Introduction 26
Compton suppression 27
Calibration 30
Coincident γ-ray measurement 33
Level scheme construction 37
Previously known experimental results 37
Fission partner identification 38
Cascade versus parallel 39

X-ray information 40
Assigning J^{π} 40
Transition intensity 44
Coincident LCP – γ-ray measurement 44
Timing analysis 46

IV. HALF-LIFE MEASUREMENTS OF NUCLEAR STATES 49

Introduction 49
Existing measurements 49
Triple γ coincidence technique 52
New measurements 55
Discussion 59
Correction function 60
Necessity of correction function 60
Exponential correction function 61
Linear correction function 63
Comparison 64
Deformation measurements 64
Conclusions 66

V. EXCITED LEVELS IN ^{113,115,117}PD 71

Introduction 71
Previous studies 71
^{113}Pd 72
^{115}Pd 73
^{117}Pd 74
Systematics 75
Experimental details 76
Discrepancy with concurrent paper 78
New level schemes 79
^{113}Pd 80
^{115}Pd 81
^{117}Pd 83
Re-examination of ground states 84
^{113}Pd 84
^{115}Pd 84
^{117}Pd 87
High spin side bands 88
Conclusions 89

VI. NEUTRON YIELDS IN BINARY AND TERNARY FISSION 90

Introduction 90
Previous ^{252}Cf neutron studies 91

Hot fission mode 94
Measuring neutron multiplicities 96
New binary fission results 98
Discussion of new binary fission neutron yield results 102
Ternary fission studies 103
New ternary fission results 104
Discussion 107
Normalization problems 108
Ba-α-Zr discussion 108
Xe-α-Mo discussion 109
Te-α-Ru discussion 109
Ternary fission versus binary fission 109
Source of excess neutrons 110
Conclusions 111

VII. SUMMARY 112

REFERENCES 115

LIST OF TABLES

Table Page

1. Energies and intensities of transitions from ^{56}Co and ^{152}Eu 31
2. Tabulated previous half-life measurements (in ns).....50
3. Exponential correction function half-life results 62
4. Linear correction function half-life results 63
5. Deformation parameter calculations.....66
6. Neutron yield matrix for Xe-Ru.....99
7. Neutron yield matrix for Ba-Mo.....101
8. Neutron yield matrix for Ba-α-Zr.....105
9. Neutron yield matrix for Xe-α-Mo.....106
10. Neutron yield matrix for Te-α-Ru 107

LIST OF FIGURES

Figure Page

1. Chart of nuclides 4
2. Fragment yield distribution for SF of ^{252}Cf [Wah88] 6
3. Spontaneous fission schematic 7
4. Gammasphere in the open position. The two halves can slide together to close the sphere. 10
5. Resolving power of Gammasphere 11
6. Ternary fission schematic 12
7. ΔE - E telescope schematic 14
8. ΔE vs. E two dimensional plot 16
9. Projection of α-gated γ-γ matrix 17
10. Projection of α-gated γ-γ matrix (high energy) 18
11. Detector array for 2005 ANL experiment 21
12. Gammasphere cross-section schematic [GAM] 28
13. Compton suppression comparison spectra [GAM] 29
14. Calibration spectra from ^{56}Co and ^{152}Eu sources 32
15. Gammasphere efficiency curve in arbitrary units 33
16. ^{144}Ba ground state band 34
17. Triple coincidence gating series in ^{144}Ba 36
18. Fission partner identification in ^{106}Mo 39
19. Internal conversion coefficient curve [Fir96] 43

20. Comparison of γ-γ-γ spectrum with α-gated spectrum showing 212.6 keV transition in ^{100}Zr.....46

21. Decay curve of 9/2$^-$ state in ^{143}Ba [Sch79].....51

22. Sample γ-ray cascade.....53

23. ^{143}Ba peaks (117.7 and 493.3 keV) in 8, 16, 20, 28, 48, 72 ns time windows.....55

24. ^{98}Sr half-life curve fitting (E_γ = 144.3keV, $2^+ \rightarrow 0^+$).....56

25. ^{102}Zr half-life curve fitting (E_γ = 151.8 keV, $2^+ \rightarrow 0^+$).....57

26. ^{104}Zr half-life curve fitting (E_γ = 140.3 keV, $2^+ \rightarrow 0^+$).....57

27. ^{137}Xe half-life curve fitting (E_γ = 314.1 keV, $17/2^- \rightarrow 13/2^-$).....58

28. ^{143}Ba half-life curve fitting (E_γ = 117.7 keV, $9/2^- \rightarrow 5/2^-$).....58

29. ^{152}Ce half-life curve fitting (E_γ = 81.7 keV, $2^+ \rightarrow 0^+$).....59

30. Quadrupole deformation schematic.....66

31. Single particle energy levels showing shell gaps at high deformation (Z = 38, 40 and N = 60, 62, 64) [Ham89].....69

32. Beta decay of ^{113}Pd [Fog87].....73

33. Beta decay of ^{115}Pd [Fog90].....74

34. Beta decay of ^{117}Rh [Pen91].....75

35. Previous odd-A Pd negative parity systematics.....76

36. Top spectrum has a double gate on two known transitions in the negative parity band of ^{117}Pd. Note the strong new 63.7 keV transition. The bottom spectrum has a double gate with one common transition and the new 63.7 keV transition.....77

37. Double gate in ^{115}Pd showing coincidence relation between 39.0 and 49.0 keV transitions.....79

38. New scheme of negative parity levels in ^{113}Pd.....81

39. New scheme of negative parity levels in ^{115}Pd, with inset from [Urb04].....82

40. New scheme of negative parity levels in ^{117}Pd 83
41. Level systematics in odd-A Pd nuclei [Pen93] 85
42. Comparison of negative parity levels in ^{123}Xe and ^{115}Pd.....86
43. Negative parity levels in odd-A $^{107-117}$Pd 87
44. High spin negative parity side bands in ^{113,115,117}Pd.....88
45. Previous neutron multiplicity measurements [Ter97].....92
46. Previous Ba-Mo neutron multiplicity measurement [Ter97].....93
47. Ba-Mo neutron multiplicity measurement from [Wu00].....94
48. Schematic of two coexisting fission modes in ^{252}Cf 95
49. Sample spectrum gated on ^{138}Xe showing partner Ru nuclei 97
50. Xe-Ru neutron multiplicities.....100
51. Ba-Mo neutron multiplicities.....101
52. 3D yield intensity plot for a selected energy range in ternary fission of ^{252}Cf ..104
53. Ba-α-Zr neutron multiplicities.....105
54. Xe-α-Mo neutron multiplicities.....106
55. Te-α-Ru neutron multiplicities 107

CHAPTER I

INTRODUCTION

The trend of scientific research has always been towards more and more exotic fields. In nuclear structure, this trend is towards nuclei with a greater excess of protons or neutrons than the stable isotopes. These exotic nuclei often exhibit unusual features that allow us to probe rare nuclear processes. We produce many of these neutron-rich nuclei in the spontaneous fission of ^{252}Cf. Performing prompt γ-ray spectroscopy on the fission fragments allows us to study the behavior of these excited nuclei as they de-excite to their ground states.

With sophisticated experimental equipment and data analysis techniques, we are able to measure the timing relationships between transitions to find the half-lives of some of these states. A new technique allows us to use our fission γ-ray data to measure the half-lives without the need for a separate experiment for each nucleus. The half-lives of excited levels in many of these neutron-rich nuclei have not been previously measured, while others with existing measurements have large uncertainties. Our results will improve the accuracy and precision of these measurements. The resulting half-life data also allow us to calculate the ground state deformations of these nuclei. We are especially interested in nuclei in the A~100 region known to have large deformations.

The timing of the detected γ-rays allows us to sort the data into coincidence measurements. This allows us to identify the specific fission fragment nuclei by the γ-rays they emit and determine the structure of their excited levels. These levels can be

arranged into detailed level schemes that show the relative position of levels in a nucleus. Nuclei can often be excited into bands of transitions that are closely associated with one another. Understanding the nature of these bands from the basis of the deformed shell model is an important aspect of nuclear structure. The band structure and ground state spin and parity of ^{113,115,117}Pd are re-examined with higher statistics and a larger energy range. New transitions are discovered, and level spin and parity assignments are re-assigned.

Another aspect of the fission process we can study is inferred from the population of specific fission fragments. During the spontaneous fission, the fragment nuclei are created in an excited deformed shape. They evaporate neutrons to become more stable and subsequently emit γ-rays as they de-excite to the ground state. The number of neutrons emitted is expected to follow a Gaussian distribution, but one fission pairing was reported to undergo a bimodal fission that can be observed in the neutron emission data. Our new data allow us to re-examine this study and extend the work to ternary fission. This allows us to re-measure the hot fission mode with more accuracy and observe the ternary fission process to see if the hot mode is present.

CHAPTER II

EXPERIMENTAL TECHNIQUES

Introduction

New developments in technology have made for powerful advancements in our ability to design and perform experiments. We are able to probe more exotic nuclei and discover much more detailed information about them. High statistics studies of rare events such as ternary fission are now possible. The development and construction of large γ-ray detector arrays have made available coincidence measurements previously inaccessible. Such new measurements allow us to sort through the available data with greater selectivity. It is incumbent on the experimentalist to take full advantage of these new tools and use them well.

A useful method of creating exotic neutron-rich nuclei is to take advantage of basic nuclear physics. As the Coulomb force grows stronger with atomic number Z, the chart of nuclides in Figure 1 bends towards the neutron-rich side of the N=Z line. The heavy elements that undergo spontaneous fission lie in this neutron-rich region. The fission products thus preferentially populate nuclei on the neutron-rich side of that line.

The black dots in Figure 1 represent stable nuclei in the "valley of stability". Outside this valley, the colored squares represent unstable nuclei. Red nuclei are proton-rich and decay by β^+ or electron capture. Blue nuclei are neutron-rich and undergo β^- decay. Yellow nuclei undergo α decay, and green nuclei undergo spontaneous fission. The vertical and horizontal lines mark nuclear "magic numbers" from spherical shell

model calculations and experimental results that indicate stronger binding energies and separation energies at these closed shells. The dashed line indicates the N=Z line.

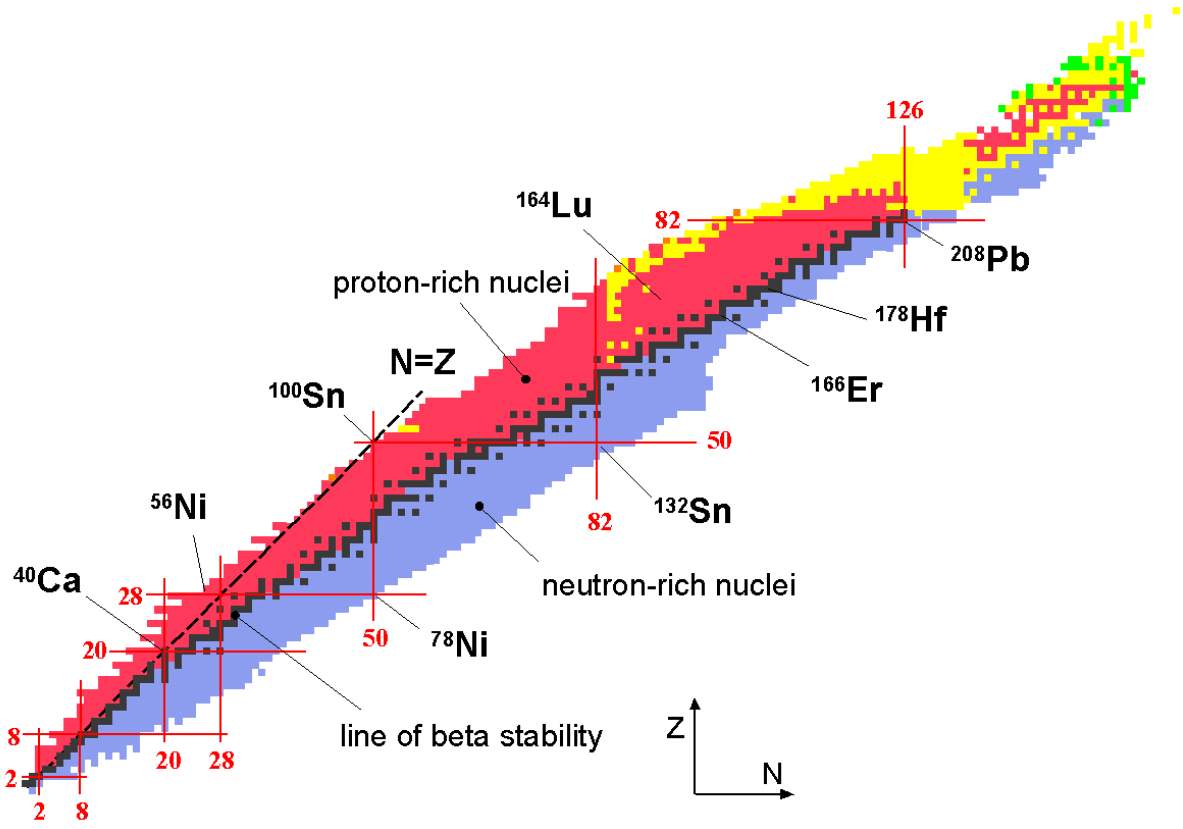

Figure 1: Chart of nuclides

Spontaneous Fission of ^{252}Cf

A spontaneously fissioning (SF) source of ^{252}Cf populates over 100 different nuclei. A distribution of yields as a function of mass number is shown in Figure 2 [Wah88]. The double peaked distribution reflects the fission into a lighter and a heavier fragment. This is a powerful and convenient laboratory tool for nuclear structure. We are spared the trouble of designing reactions to produce specific isotopes. Ion beam

experiments are limited to a few nuclei of interest created in any given reaction. Accelerator time is also costly and difficult to obtain. More importantly, heavy ion reactions can only create nuclei with one or two more neutrons beyond the nuclei in the valley of stability. A fission source creates many of the same nuclei that could be formed with a series of dedicated ion beam experiments and extend the range to more neutron-rich nuclei. A high statistics ^{252}Cf γ-γ-γ, fission fragment-γ-γ, or light charged particle-γ-γ experiment provides years of data for analysis.

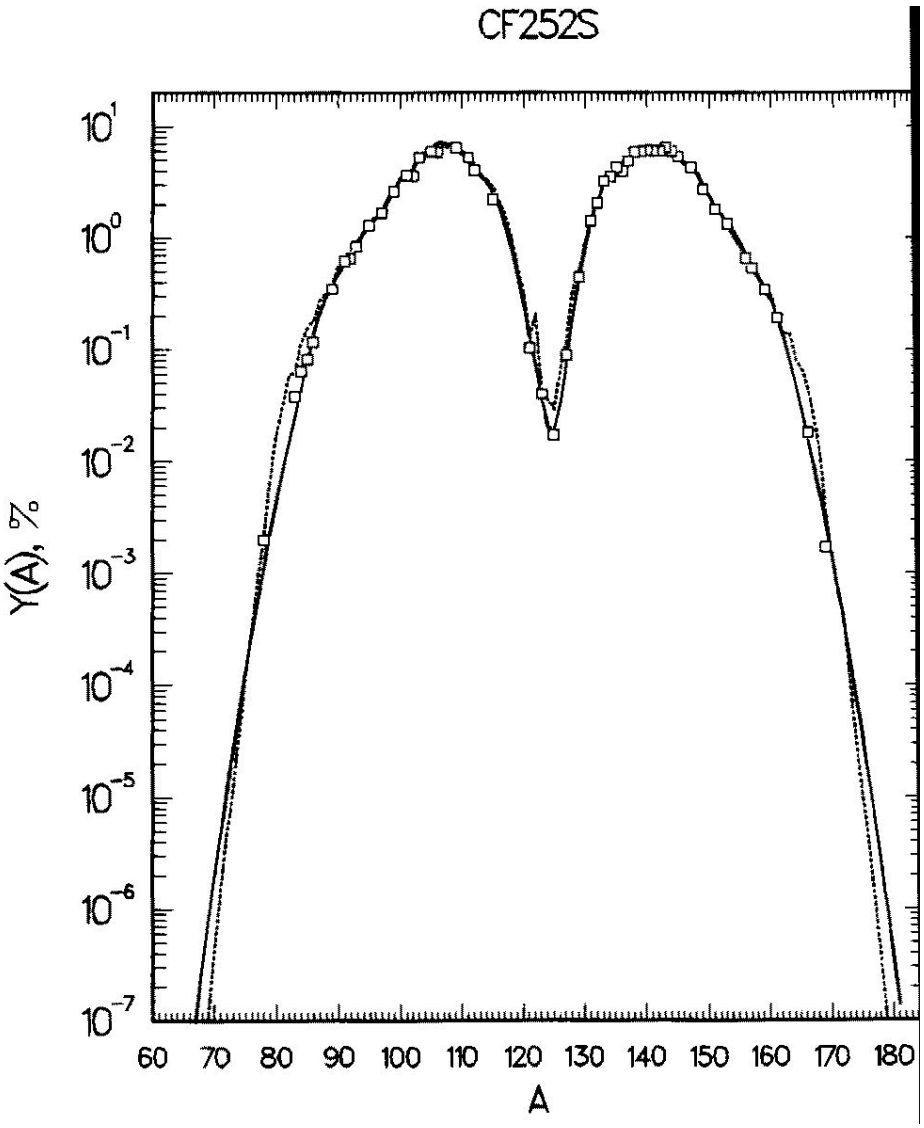

Figure 2: Fragment yield distribution for SF of ^{252}Cf [Wah88]

In the fission process, the parent nucleus splits into two (or more) daughter nuclei with roughly a 1.4:1 ratio of masses between the heavy and light fragment. These primary fission fragments then evaporate some number of neutrons, usually around four for SF of ^{252}Cf. These nuclei are now secondary fragments that promptly emit γ-rays if they were formed in an excited state. Almost all of the fragments are unstable to β^- decay when they reach the ground state until a stable nucleus is reached. The first and second

stages of the fission occur very quickly, with most neutrons evaporated in 10^{-18} to 10^{-15} seconds. A brief schematic of the timescales in SF is shown in Figure 3.

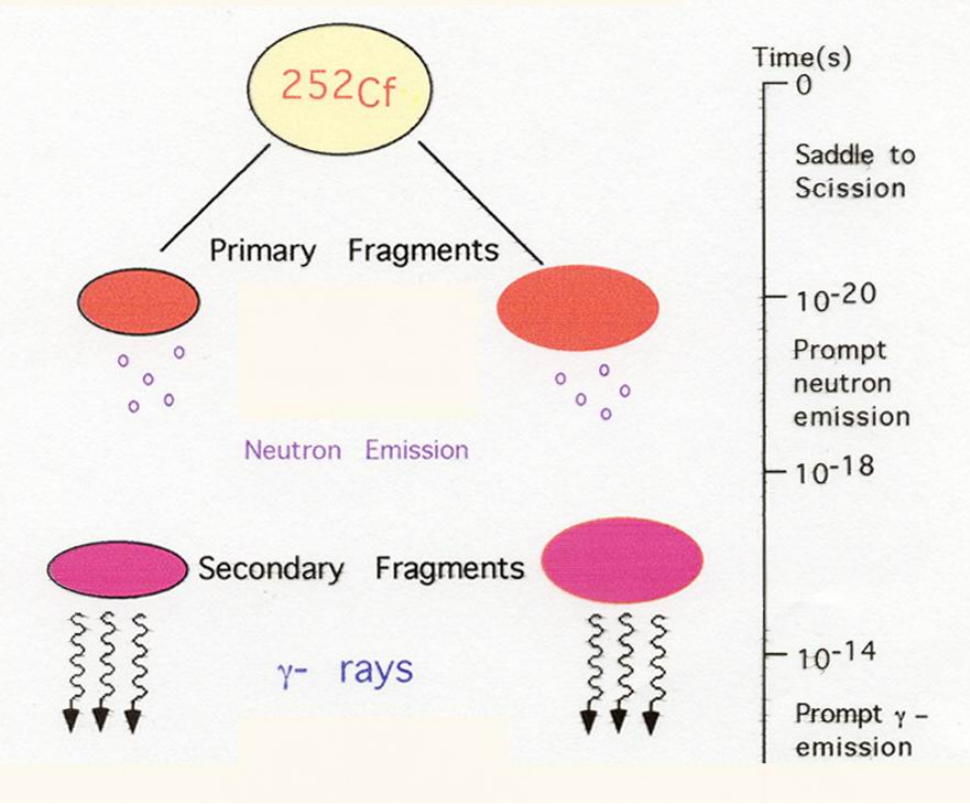

Figure 3: Spontaneous fission schematic

The drawback of using a fission source such as ^{252}Cf is that we populate many nuclei as well as their fission partner nuclei. For a nucleus such as ^{104}Mo, the partner nuclei $^{138\text{-}148}$Ba will also be created in coincidence. Each excited nucleus undergoes de-excitation according to its particular nuclear structure. These particles and γ-rays are all emitted within the same time period, giving us overlapping energy signals that can obscure the signatures of any one nucleus of interest. An experiment studying a ^{252}Cf

source will only see the strongest of signals emerging from an intense continuous background.

This problem is addressed by taking advantage of the high multiplicity of emitted γ-rays from an excited nucleus. The fission process results in nuclei created with high angular momentum. In order for the nucleus to reach the ground state, it must undergo a series of transitions, with a γ-ray emitted at each step. For each created nucleus, we can observe numerous emitted γ-rays belonging to one nucleus along with those associated with the various partner nuclei. With proper data analysis techniques, we can sort through the forest of signals to isolate peaks of interest.

Gamma Ray Detection

Detection of γ-rays has improved considerably over the years. The three key principles are energy resolution, granularity, and detection efficiency. We would like to detect the full energy of the γ-ray with as much accuracy and precision as possible. Granularity allows us to do two things: detect simultaneous events and determine the trajectory of the detected radiation. We must also have as many counts as possible from detection efficiency to study rare nuclear processes. The solution to maximize these three factors is to use an advanced array of solid-state detectors.

Modern germanium crystal (Ge) detectors provide us with the best energy resolution. The γ-ray passing through the semi-conductor crystal creates electron-hole pairs by exciting an electron that subsequently creates many other electron-hole pairs. When a bias voltage is applied across the crystal, the charge can be collected in proportion to the energy deposited in the detector. A cooled Ge detector requires only

2.96 eV to create an electron-hole pair. Ionizing radiation thus creates a large amount of charge, which results in much better resolution than previous generations of detectors such as NaI scintillators that collect photons.

In order to achieve strong granularity, we use an array of many independent Ge detectors. Instead of a single detector crystal, it is preferrable to have several small detectors covering the detection area. The benefit of this is that multiple separate events can be separated with increased granularity. If two γ-rays are emitted close together in space, a single large detector will detect both of them as a single event. This will lead to an incorrect multiplicity measurement and an incorrect energy measurement. Many of these events would have to be discarded as pile-up, greatly reducing the number of observed events.

Fission events occur uniformly in space, and the γ-rays are emitted isotropically. The detection efficiency is maximized by covering as much solid angle as possible. We could theoretically cover the entire 4π solid angle with a single detector, but that would provide poor granularity. Instead, over a hundred individual Ge detectors can be arrayed in a sphere to surround the source and provide a large detection solid angle.

Gammasphere

The array of detectors used in our ^{252}Cf experiments is called Gammasphere. Gammasphere was commissioned in 1995 at the Lawrence Berkeley National Laboratory. It consists of 110 high purity Ge detectors, each surrounded with a bismuth germanate oxide (BGO) suppression shield. The detectors are oriented in a sphere facing the target chamber, inside of which is the source. The Ge detectors are kept cool with an

automated liquid nitrogen delivery system. Figure 4 shows the target chamber on the beamline, along with the face of one half of the sphere. The entire half slides inwards to close on the chamber and form a complete sphere.

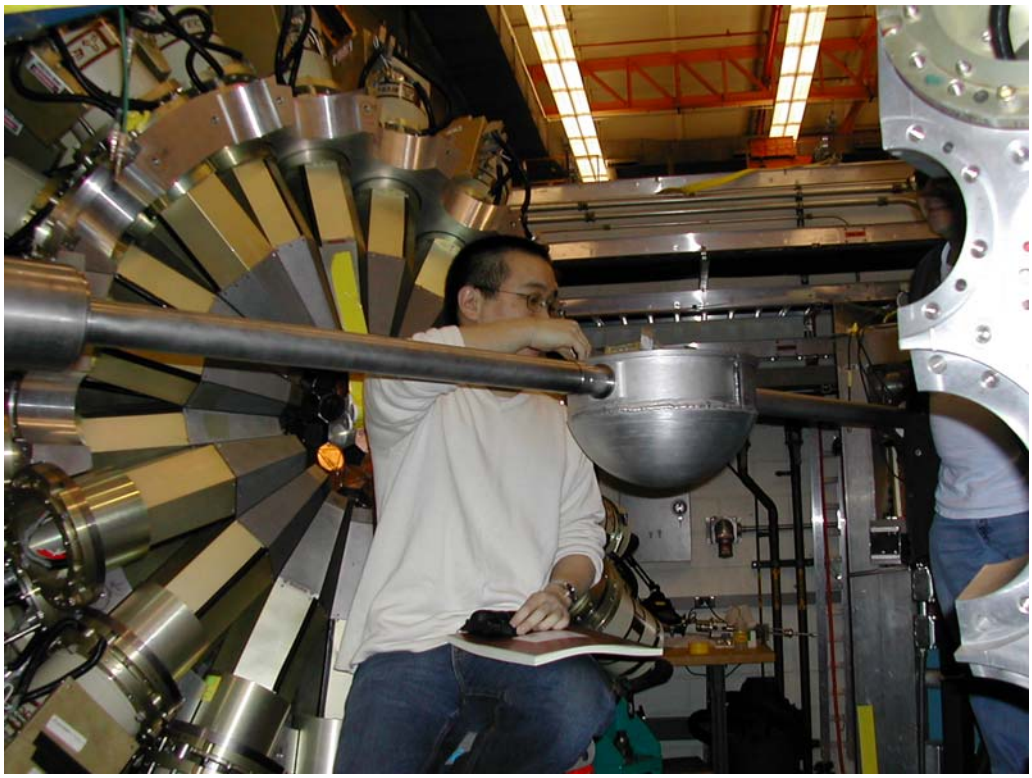

Figure 4: Gammasphere in the open position. The two halves can slide together to close the sphere.

Gammasphere is one of the most powerful γ-ray detector arrays in the world. The Ge detectors provide energy resolution of less than 3 keV at 1 MeV. Photopeak efficiency is around 10% at 1 MeV which is quite good for γ-ray detection. A broad metric of the resolving power increase available with Gammasphere can be seen in Figure 5. The increasing slope section represents the gradual installation of the detectors that comprise Gammasphere. The final resolving power is two orders of magnitude

higher than previously available detector arrays. This is further improved by using segmented detector crystals for 70 of the Ge detectors. These are split into two halves, making Gammasphere effectively 180 independent Ge detectors.

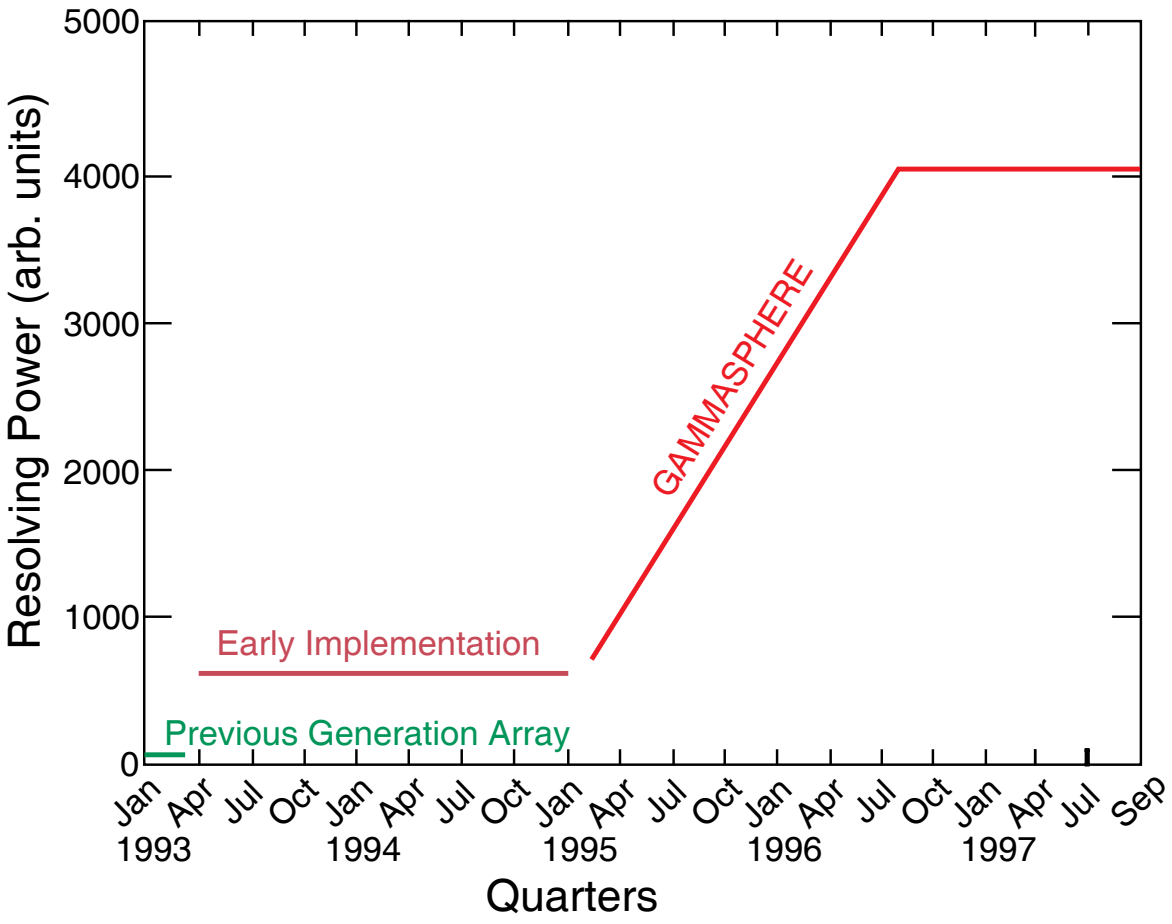

Figure 5: Resolving power of Gammasphere

Ternary Fission

The process of spontaneous fission produces two large binary daughter nuclei in the large majority of events. But sometimes, instead of two fragments, the nucleus splits into three fragments. Two of these are large primary fragments and one is a much lighter

ternary fragment. The most common ternary particles are α particles, which are emitted in approximately 1 in 500 fission events. Heavier particles are also emitted, such as Li, Be, B, and C nuclei. The distribution of daughter fragments is different in ternary fission, due to the nucleons and energy carried away by the ternary, light charged particle (LCP). A schematic of the ternary fission process is shown in Figure 6.

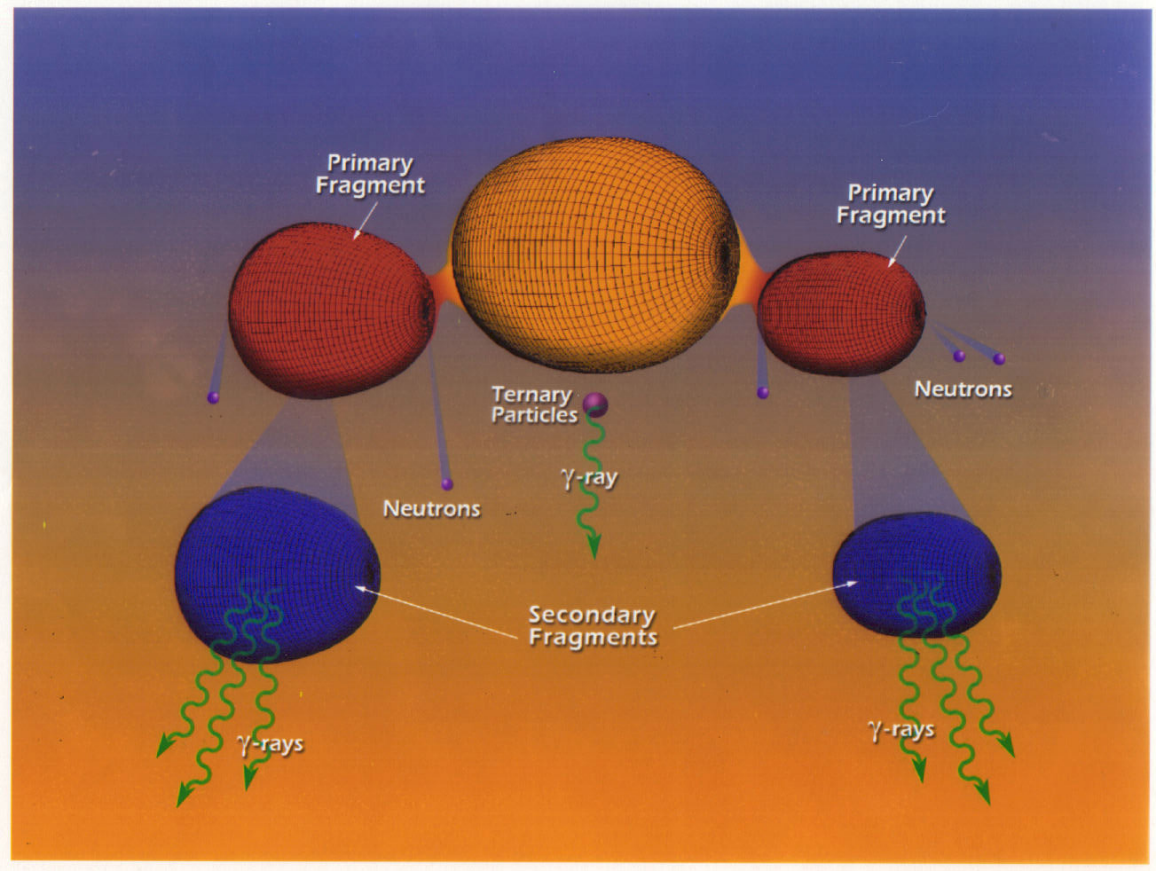

Figure 6: Ternary fission schematic

The ternary fission events require more careful study. The pairs of primary fragments will be different due to the subtraction of the ternary particle from the available nucleons. The corresponding γ-ray spectra will be accordingly different. We may also see unusual nuclear processes in these fission events, since the shape and deformation of the fissioning nucleus is much different in ternary fission.

These LCPs can be detected with a specialized detector array. Of course any solid state detector would allow us to detect the particles and measure their energies. In order to identify the specific type of LCP, we use a pair of silicon detectors acting in concert. One detector is a thin sheet of silicon called the ΔE detector. The ΔE detectors are thin, only 10 μm, and allow the LCPs to pass completely through. The second detector is a thicker silicon detector called the E detector. This detector is thicker, 400 μm, such that it completely stops the LCPs. Together, the pair is called a ΔE-E telescope. A schematic of the detectors and their orientation is in Figure 7. The detectors are aligned to face the source in a collinear arrangement with each E detector directly behind a ΔE detector. This detector arrangement was used in the 2001 experiment at Berkeley.

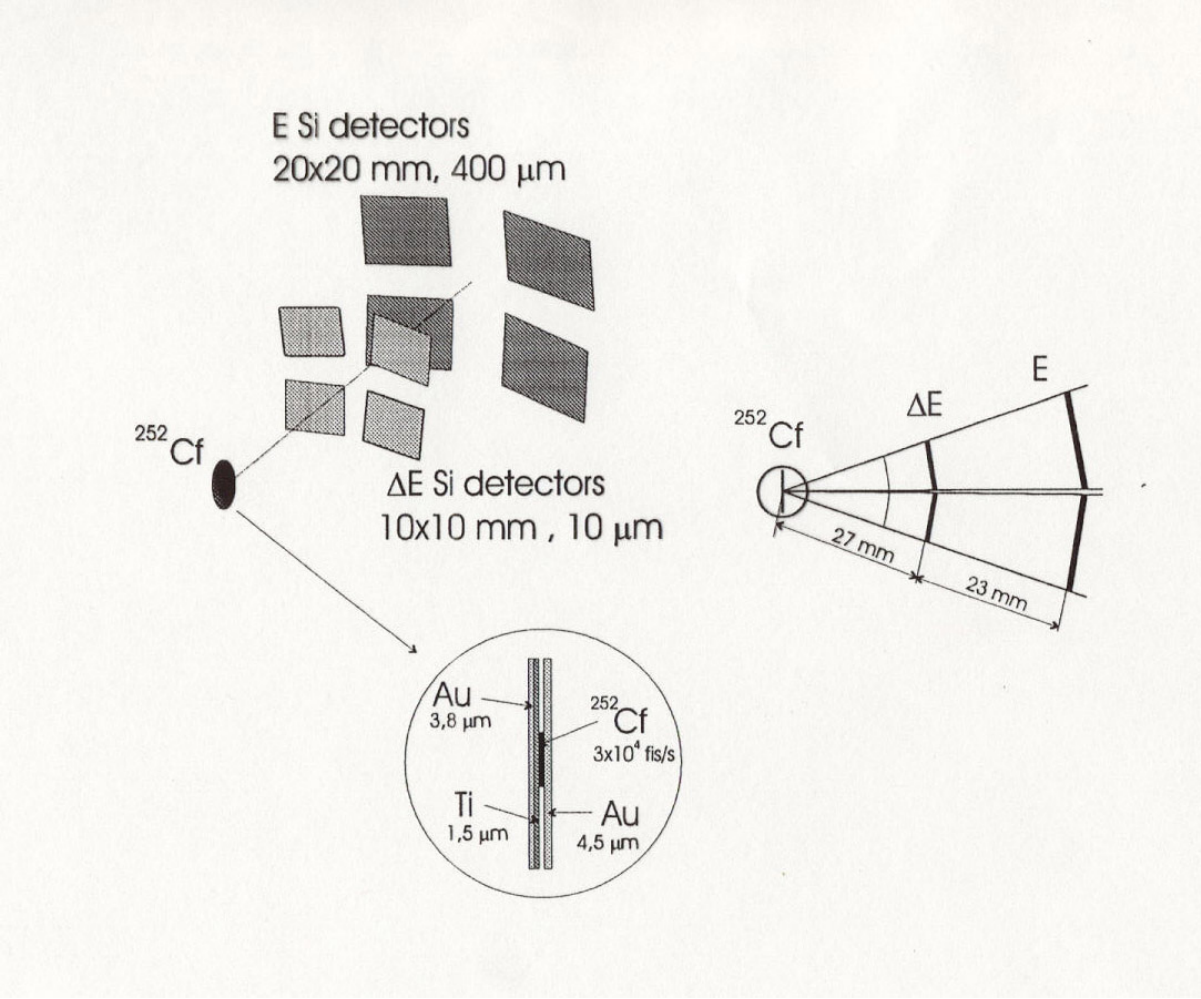

Figure 7: ΔE - E telescope schematic

The principle behind the ΔE-E telescope is that when charged particles pass through a material, the amount of energy they deposit per unit distance depends on the atomic number of the LCP. The higher Z particles deposit a greater proportion of their energy in a given thickness of the ΔE detector. This energy deposition comes mostly from inelastic collisions with atomic material and elastic scattering from nuclei. The full quantum mechanical treatment is given by the Bethe-Bloch formula here [Leo87]. The

key dependency is that the amount of energy transferred in a unit distance is strongly dependent on the charge of the nucleus.

$$\frac{dE}{dx} = -2\pi N_a r_e^{\,2} m_e c^2 \rho \frac{Z}{A} \frac{z^2}{\beta^2} [\ln(\frac{2m_e\gamma^2\nu^2 W_{maz}}{I^2}) - 2\beta^2 - \delta - 2\frac{C}{Z}]$$

N_a = Avogadro's number r_e = electron radius m_e = electron mass ρ = density
Z = atomic number of absorber A = mass of absorber z = atomic number of LCP
ν = velocity of nucleus $\beta = \nu/c$ γ = relativistic factor
I = mean excitation potential W_{max} = max energy transfer
δ = density correction C = shell correction

The ΔE and E detectors are oriented perpendicularly to the line connecting the detector and the source such that an LCP emitted must pass through first the ΔE and then the E detectors. The LCP deposits a fraction of its energy in the ΔE detector and then deposits the remainder of its energy in the E detector.

A plot of the energies in the ΔE detectors versus the energies in the E detector in coincidence with the first signal is shown in Figure 8. We can see how the different LCPs separate themselves in a two-dimensional plot. Each species of LCP falls into a banana-shaped region on the ΔE vs. E plot, allowing us to select events associated with a specific LCP. We can then analyze γ-ray spectra in coincidence with the LCP of our choice. Also clearly visible is the decreasing number of detected LCPs as the atomic number increases. There are drastically fewer Be nuclei detected than He nuclei. All the higher Z species result in very low statistics, and analysis is reserved for very specialized studies.

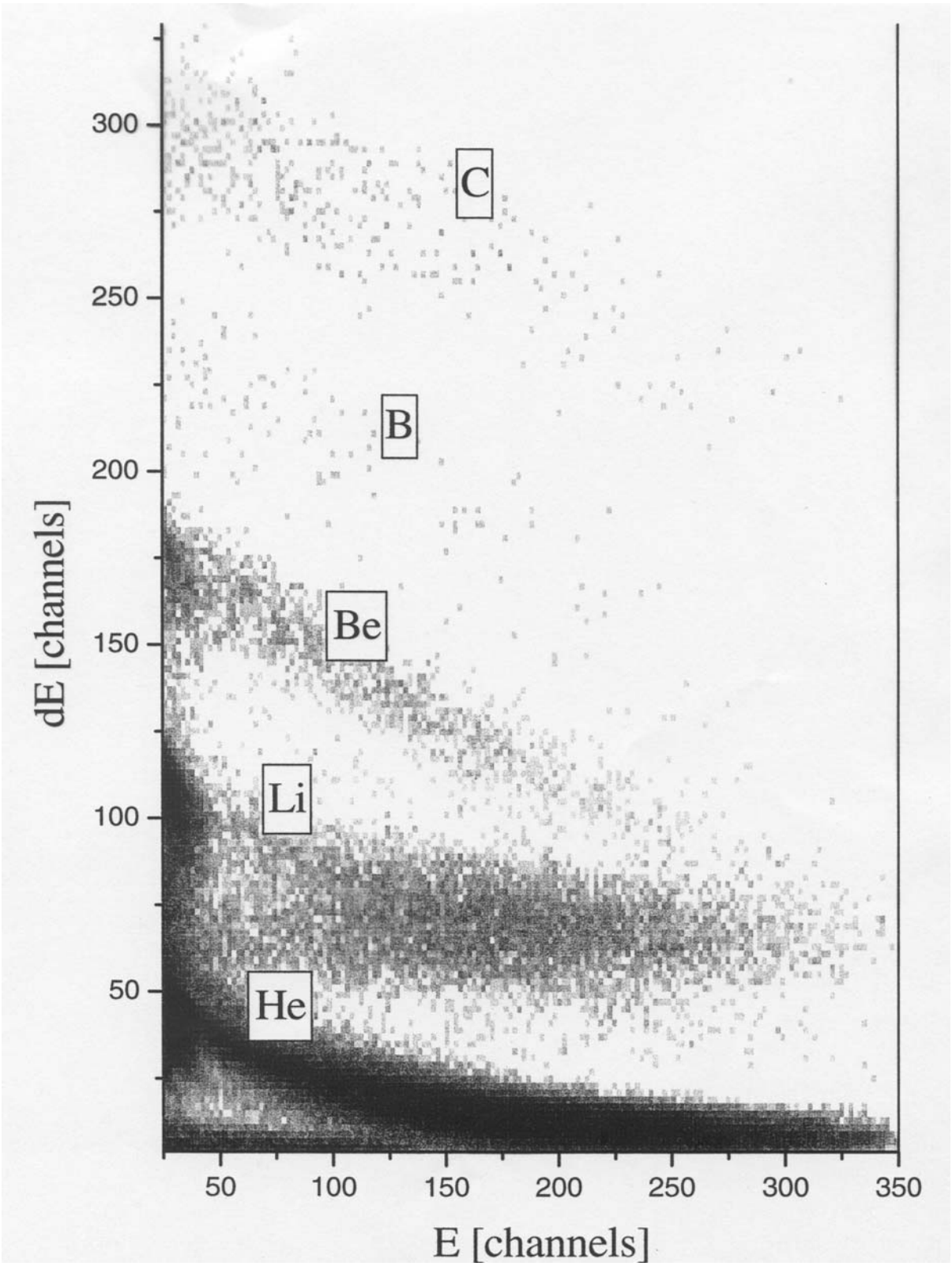

Figure 8: ΔE vs. E two dimensional plot

The projection of the γ-γ matrix in coincidence with an α is shown in Figures 9 and 10. Figure 9 shows the lower energy region while Figure 10 shows the higher energy region. Many nuclei can be identified in the spectrum by their transitions. In addition, careful coincidence gating can substantially enhance peaks of interest.

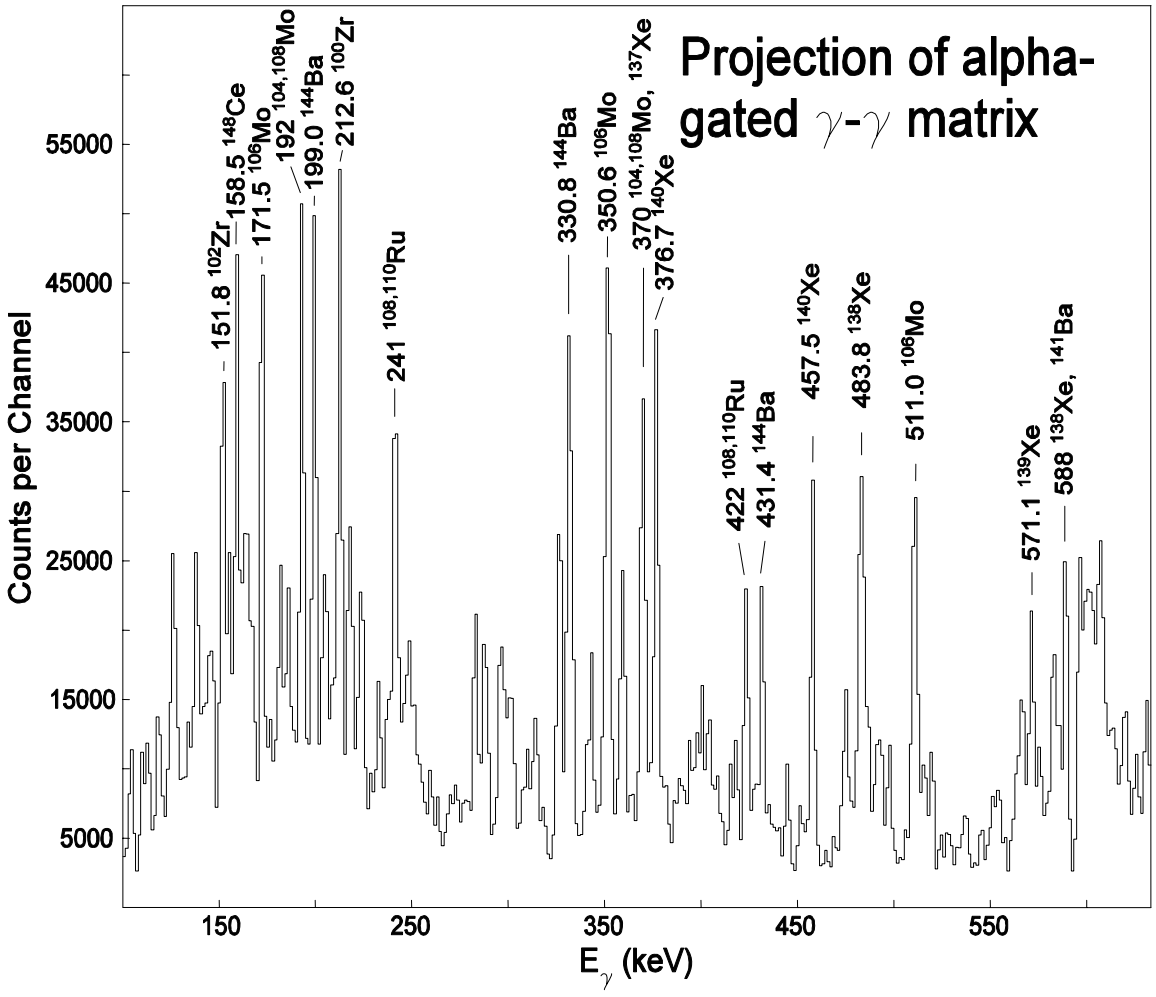

Figure 9: Projection of α-gated γ-γ matrix

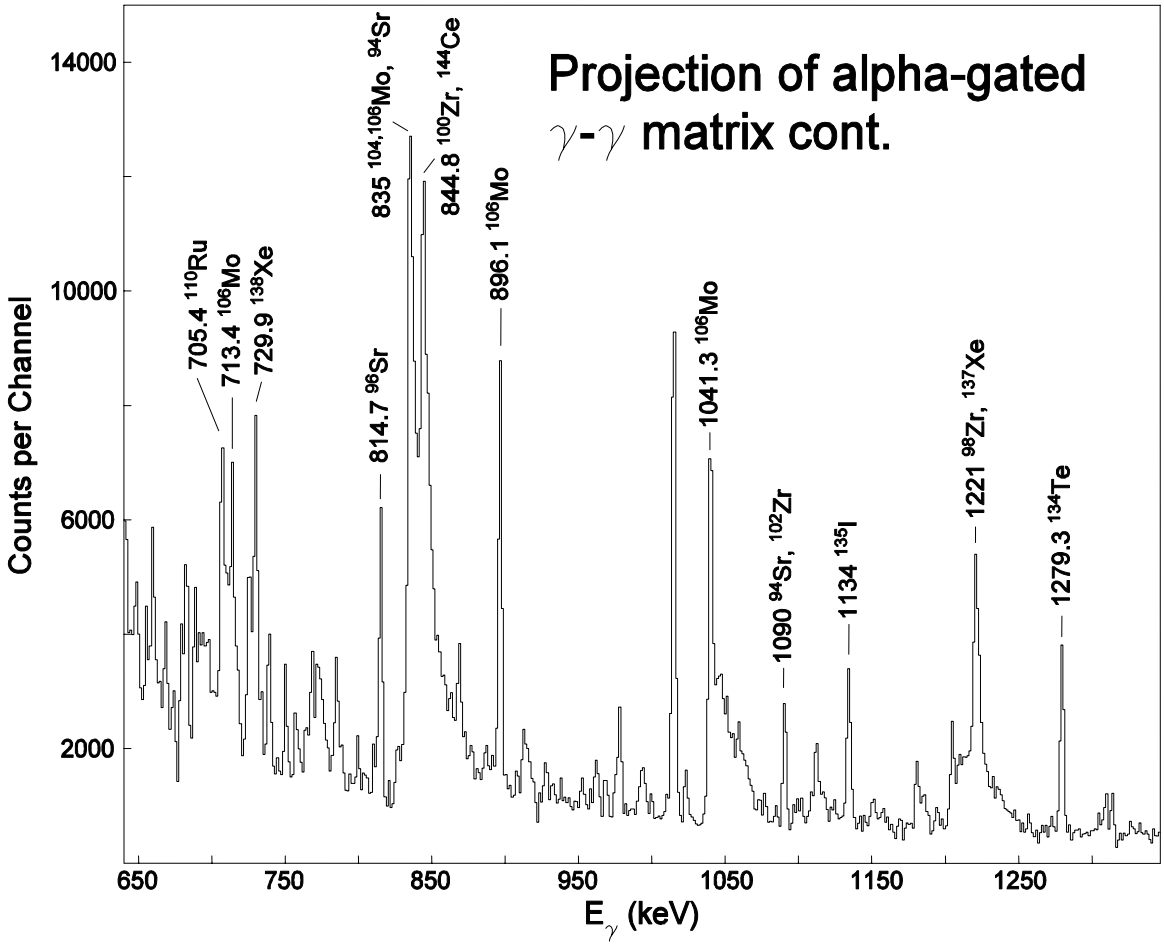

Figure 10: Projection of α-gated γ-γ matrix (high energy)

Experimental Details

Several experiments have been carried out with Gammasphere and a ^{252}Cf source. Gammasphere has moved between Lawrence Berkeley National Laboratory (LBNL) in Berkeley, CA and Argonne National Laboratory (ANL) in Chicago, IL. Data from three different experiments have been analyzed, with different source and detector details for each. I was present and participated in the two most recent experiments at LBNL and ANL, assisting in setup, testing, and data taking.

1995 binary fission at LBNL

In 1995, a 28 μCi source was sandwiched between two foils of Ni with thickness 11.3 mg/cm^2 on either side. In addition, a 13.7 mg/cm^2 Al foil was added on both sides. Gammasphere consisted of 72 Ge detectors. 9.8×10^9 triple or higher fold events were recorded.

2000 binary fission at LBNL

In 2000, a 62 μCi source was used with no LCP detectors. With no requirement for fragment identification, the entire source was sandwiched between two Fe foils with thickness 10 mg/cm^2 and encased in a 7.62 cm polyethylene ball. This experiment resulted in 5.7×10^{11} triple-fold γ-γ-γ events. This is the largest data set recorded, and was used for most triple-coincidence studies. A γ-γ-γ coincident cube was constructed with minimal compression to maximize the energy resolution in our analysis spectra.

2001 ternary fission at LBNL

In 2001, a 35 μCi source was used at LBNL with 8 LCP detectors as seen in Figure 4. The source was deposited on 1.8 μm of titanium, with gold foils on both sides. These foils stopped all primary fission fragments to minimize necessary Doppler shift corrections. The front side of the foil was 3.7 μm and the back foil was 4.6 μm. $1.6x10^7$ ternary events were recorded with the requirement of LCP-γ-γ coincidence.

The ΔE detectors were about 10 μm thick, with an area of 10 x 10 mm^2. Four of them were arranged at azimuthal angles of 45°, 135°, 225°, and 135° and a polar angle of 30°, with the other four at the same azimuthal angles and a polar angle of 150°. The E detectors were placed 13 mm directly behind each ΔE detector, with a thickness of 400 μm and an area of 20 x 20 mm^2.

2005 binary and ternary fission at ANL

In 2005, another fission experiment was performed at ANL. This experiment was focused on detecting the primary fission fragments directly. Correspondingly, the source was left barely covered. The ^{252}Cf had a strength of 35 μCi deposited on a 1.5 μm Ti foil and covered with another thin 1.5 μm layer of Ti. Two double-sided silicon strip detectors (DSSDs) were placed on either side of the source. The DSSD was 1.85 mm thick, with an area of 60 x 60 mm^2 split into 32 strips on each side. In addition, 6 ΔE-E telescopes were arranged in a ring perpendicular to the source-DSSD axis. The ΔE detectors were about 10 μm thick. The E detectors had a thickness of 1 mm with an area of 20 x 20 mm^2 split into 4 square sectors for increased granularity. A picture of the detector array is shown in Figure 11. The two DSSDs can be seen flanking the ring array

of ΔE-E detectors. The source is placed in the center of the array, so fission fragments travel towards the DSSDs and the LCPs are ejected orthogonally, towards the ΔE-E detectors. The data were recorded with fragment-fragment-γ-γ coincidence for binary fission and fragment-fragment-LCP-γ for ternary fission.

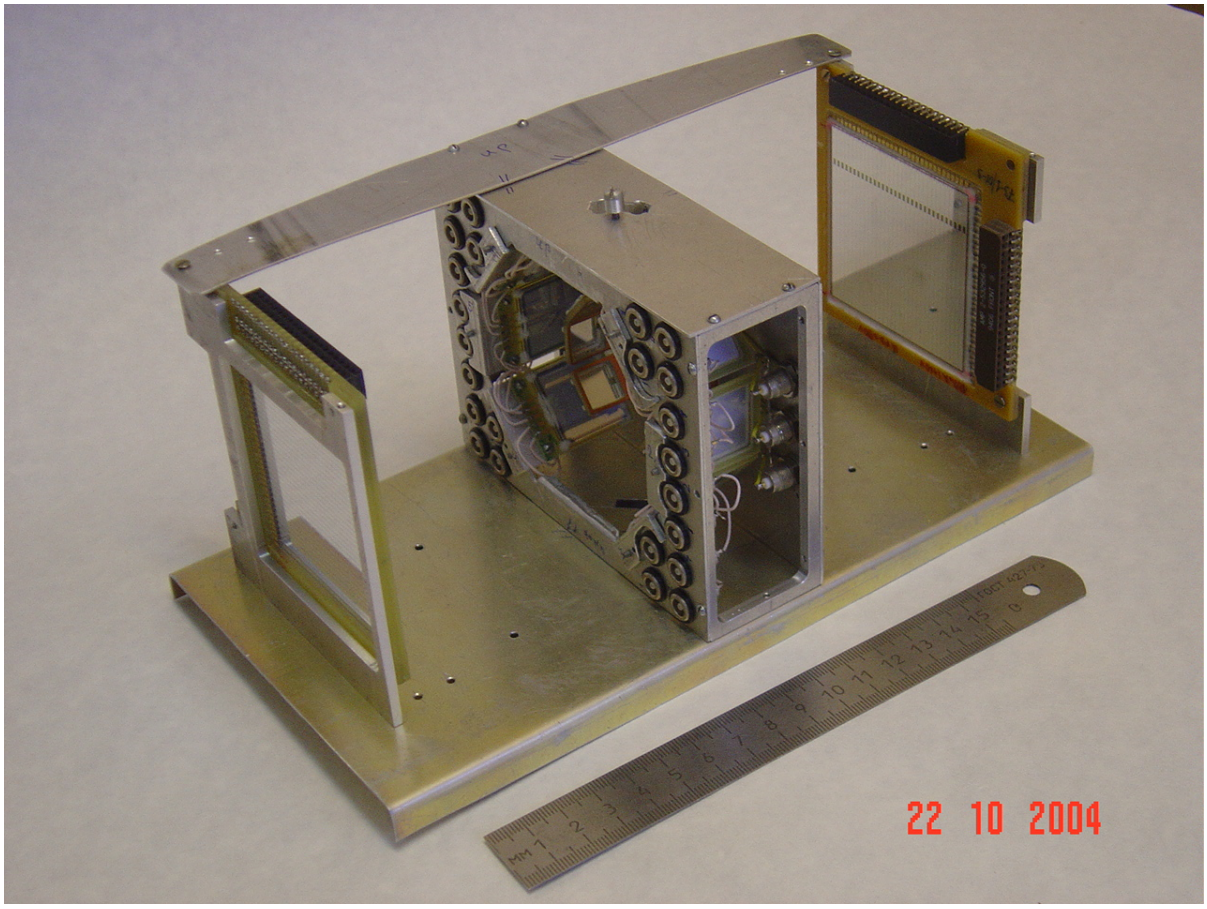

Figure 11: Detector array for 2005 ANL experiment

Experimental experience at ORNL

In addition to work carried out from the ^{252}Cf fission studies, I participated in several experiments at Oak Ridge National Laboratory (ORNL). Under the supervision of Dr. Krzysztof Rykaczewski, we developed and tested new detector systems, data acquisition setups, and innovative experimental tools. While none of these topics will directly enter this dissertation, the experiences learned there were instrumental parts of my experimental education.

Double sided silicon strip detectors

In performing studies of radioactive ion beams, detector granularity is important, just as for γ-ray detection. The best way to achieve this is to use strip detectors instead of single surface area detectors. A double sided silicon strip detector (DSSD) is a piece of silicon that has been treated to have strips of depletion zones across the front and back sides. The strips on the front run vertically while the strips on the back run horizontally. By connecting each strip to independent amplifiers and signal processors, we can identify the location of an event in space, based on the coordinates of the strips that registered the signal. For each event, we will see a strong signal in one front strip and one back strip, providing us with a "pixel" of positional information for that event.

This is useful in several ways. For a fission experiment, the direction of flight for the fragments can be detected by DSSDs. In the 2005 experiment at ANL, we expect to track individual binary and ternary fission fragments. For an ion beam experiment, various beam components may be separated out along one direction, and the position of implantation may help determine what the ion species is. In a more subtle use, proton

radioactivity signals can be filtered by requiring that the ion implantation and the proton decay signal occur in nearby strips. Events in distant pixels can be rejected as random coincidences instead of true proton radioactivity signals.

Digital signal processing

Traditional signal processing involves the use of analog electronics modules to measure the amplitude and timing of detector signals. For most circumstances, this is an acceptable setup, with fairly fast timing and decent energy resolution. However, this type of processing is limited in some more exotic types of studies. For example, in proton radioactivity, the ion implantation signal is closely followed by a much smaller proton decay signal in the same detector. Without an obvious way to discriminate between these two events, the peaks may end up summed together or rejected as pile-up.

By implementing a digital data acquisition system at ORNL with digital gamma finder (DGF) modules, this problem can be addressed. These specialized DGF modules store the entire charge collection waveform from the detectors in an onboard buffer. This allows direct analysis of the entire signal, instead of basic peak-sensing. The sensitive DSSD signals are processed with these DGF modules to maximize the resolving power of the setup at ORNL.

Molecular ion beam purification

Ion beam production at ORNL employs an ISOL (isotope separation on-line) source. In this technique, a light particle like a proton or an α particle is accelerated towards a thick target, typically uranium. The resulting fusion-fission reaction creates

many nuclear products. The source is heated to evaporate the products which are then accelerated and separated to create useful beams. Radioactive beams are highly desirable to probe exotic regions of the chart of nuclides, but they are hard to produce because of small cross-section, short half-life, and high contamination.

A method recently developed to improve beam purity takes advantage of molecular chemistry. It was discovered at ORNL that by providing sulfur ions at the source production point, some species of ions were able to evaporate out more quickly. For example, SnS^+ ions emerged much more rapidly than SbS^+ or TeS^+. Those were the strongest contaminants in tin beams, so by using the molecular separation, we were able to achieve 99% pure Sn ion beams.

Ranging out gas cell

The amount of energy an ion deposits while passing through matter depends on the atomic number of the ion, as discussed with the ΔE -E telescopes. This phenomenon can be used for beam purification. A new technique developed at ORNL takes advantage of this to selectively filter out higher Z components from an isobaric beam. By passing the ion beam through a gas cell, the higher Z ions will lose a greater portion of their energy. If the pressure of the gas is increased, eventually the higher Z ions will be completely stopped. By setting the pressure to a specific value, almost all of the contaminants can be excluded except the lowest Z component of the beam. An example of this is an A=76 cocktail beam. As created from the ion source, the beam contains copper ions as well as contamination from gallium, germanium, and arsenic. With the

right pressure in the gas cell, almost all the contaminants can be filtered out, leaving a much purer ^{76}Cu beam.

CHAPTER III

ANALYTICAL TECHNIQUES

Introduction

A wealth of data is obtained with the detectors available to study a fission source. As mentioned before, the sheer complexity of the resulting spectra presents a problem for analysis. Small peaks and rare processes can be obscured by the more intense signals. In order to examine these small peaks, we can apply sophisticated data analysis techniques to study exotic nuclei and processes.

The γ-ray spectra contain a great deal of coincidence data, thanks to the segmentation of the individual Ge detectors comprising Gammasphere. This allows us to separate γ-rays that are detected at the same time and ignore those that are detected at another random time. We can also use software analysis to examine the time spectra of various events. This can give us information about the relative timing of events.

Using the LCP detectors can also allow us to enhance certain features of interest. Recall that only 1 in 500 fission events produces a ternary fission fragment, and it becomes apparent that a coincidence measurement with the LCP detectors can greatly reduce the clutter in the observed spectra.

Once the spectra have been coincidence gated and properly calibrated, we can further isolate some of the details with more advanced gamma ray spectroscopy techniques. Examining intensity patterns, fission partner information, and gating patterns

can provide us with a way to highlight the more interesting features of our fission γ-ray spectrum.

Compton Suppression

The raw spectra generated by detectors are a complex series of signals and noise. To improve signal quality, Gammasphere signals are Compton suppressed. Each Ge crystal is surrounded by seven BGO detectors. The arrangement of the detector is seen in Figure 12.

Figure 12: Gammasphere cross-section schematic [GAM]

A γ-ray interacting with the Ge crystal only deposits its full photo-peak energy part of the time. In the majority of events, it undergoes Compton scattering, depositing part of its energy in the Ge crystal. This is depicted in the figure as the γ-ray strikes the Ge with a yellow flash and scatters out of the crystal before being detected again in the

BGO. The BGO detectors are designed to detect the scattering γ-ray to correct for this effect. By rejecting Ge events that occur simultaneously as a BGO event, we can suppress Compton events and enhance relatively the full photo-peak events. The suppression results in a significant improvement of the ratio of peak events to total events. A comparison of the unsuppressed spectrum and a Compton suppressed spectrum is shown in Figure 13.

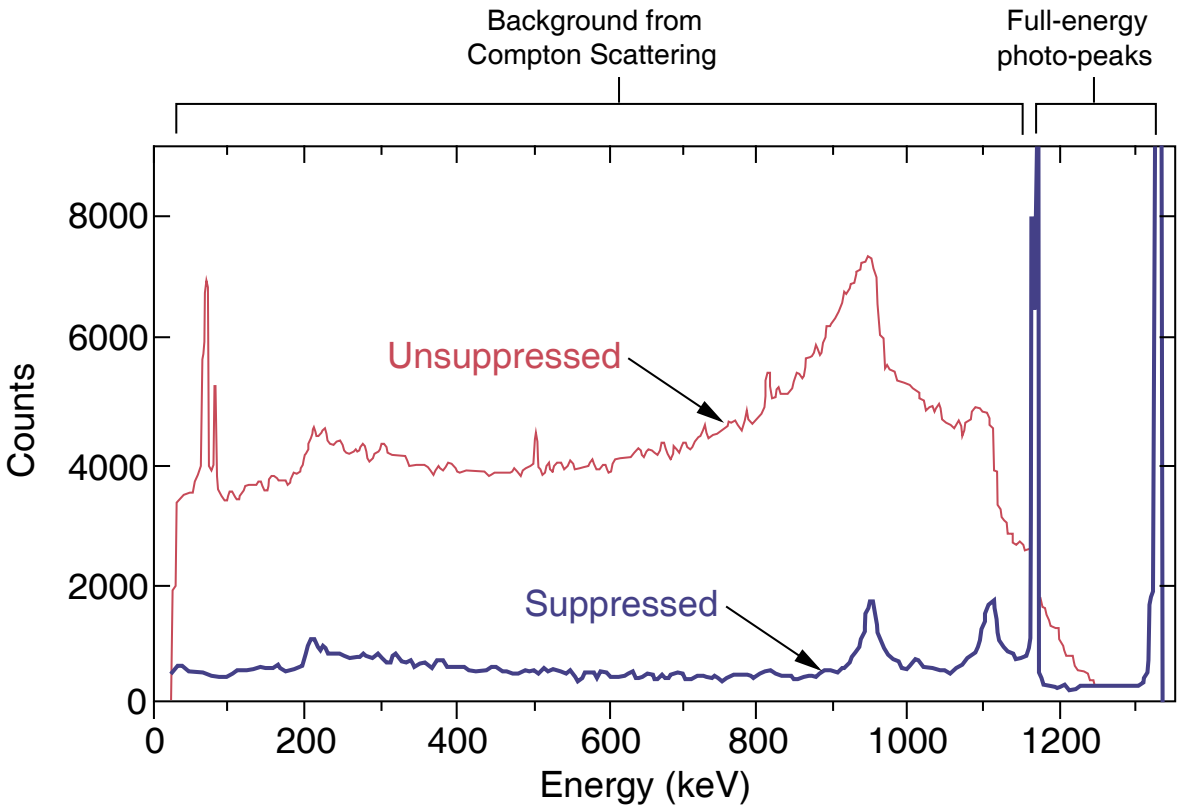

Figure 13: Compton suppression comparison spectra [GAM]

Calibration

Energy calibration of Gammasphere detectors is performed by comparing known γ-rays to the energy of measured γ-rays. This allows us to determine the relationship between true energy and electronic channel. For our ^{252}Cf experiment, the γ-ray calibration can be done online with the known peaks from the ^{252}Cf itself.

Calibrating the ΔE -E detectors required using an α source. This provided us with exactly known energies of emitted alphas from the radioactive source. A ^{229}Th + ^{148}Gd source emits alphas in a decay chain with energies of 4.8451 (^{229}Th), 5.829.6 (^{225}Ac), 6.1263 (^{221}Fr), 6.3410 (^{221}Fr), 7.0669 (^{217}At), and 8.375 (^{213}Po) MeV. The decay of ^{148}Gd provides an additional α with an energy of 3.182680 MeV. By measuring the response of the ΔE and E detectors to these energies, the absolute energy calibration can be determined.

Detection efficiency varies greatly depending on the energy of the γ-ray. For high energy γ-rays, most of them will pass through the detector. For low energy γ-rays, various thresholds and low energy cutoffs make detection difficult. In order to compare intensities of peaks at different energies, we have to calibrate the response of the Ge detectors at different energies.

This is accomplished with a standard γ-ray source. If the intensities of the calibration γ-rays are well-known, we can determine how efficient the detectors are at different energies. This then gives us an efficiency curve that can be used to analyze relative intensities in further analysis. In our Gammasphere experiments, we used ^{56}Co and ^{152}Eu sources to measure the efficiency response. A table of known transitions and energies from these sources is given in Table 1.

Table 1: Energies and intensities of transitions from ^{56}Co and ^{152}Eu

^{56}Co		^{152}Eu	
E_γ (keV)	I_γ	E_γ (keV)	I_γ
846.7638(19)	99.933(7)	121.7817(3)	28.37(13)
1037.8333(24)	14.13(5)	244.6975(8)	7.53(4)
1175.0878(22)	2.239(11)	344.2785(13)	26.57(11)
1238.2736(22)	66.07(19)	411.1165(13)	2.238(10)
1360.196(4)	4.256(15)	444.0	3.125(14)
1771.327(3)	15.49(5)	778.9045(24)	12.97(6)
2015.176(5)	3.029(13)	867.378(4)	4.214(25)
2034.752(5)	7.771(27)	964.1	14.63(6)
2113.092(6)	0.366(6)	1085.836(9)	10.13(5)
2212.898(3)	0.390(7)	1089.737(5)	1.731(9)
2598.437(4)	16.96(6)	1112.074(4)	13.54(6)
3009.558(4)	0.995(21)	1212.948(11)	1.412(8)
3201.930(11)	3.13(9)	1299.140(9)	1.626(11)
3253.402(5)	7.62(24)	1408.011(4)	20.85(9)
3272.977(6)	1.78(6)		
3451.119(4)	0.93(4)		
3548.3	0.178(9)		

The γ-ray spectra from the ^{56}Co and the ^{152}Eu are shown in Figure 14. The peaks are clear and sharp. The resulting efficiency curve can be used for all further analysis. The equation for the curve is a seven parameter function.

$$Eff = \exp[(A + Bx + Cx^2)^{-G} + (D + Ey + Fy^2)^{-G}]^{-\frac{1}{G}}$$

x = log (E_γ/100) y = log (E_γ/1000) E_γ = energy in keV

This curve in arbitrary units is shown in Figure 15. The calculated fit parameters were (A = 14.1597, B = 9.18559, C = -2.7907, D = 6.36297, E = -0.65056, F = 0.0, G = 2.09765).

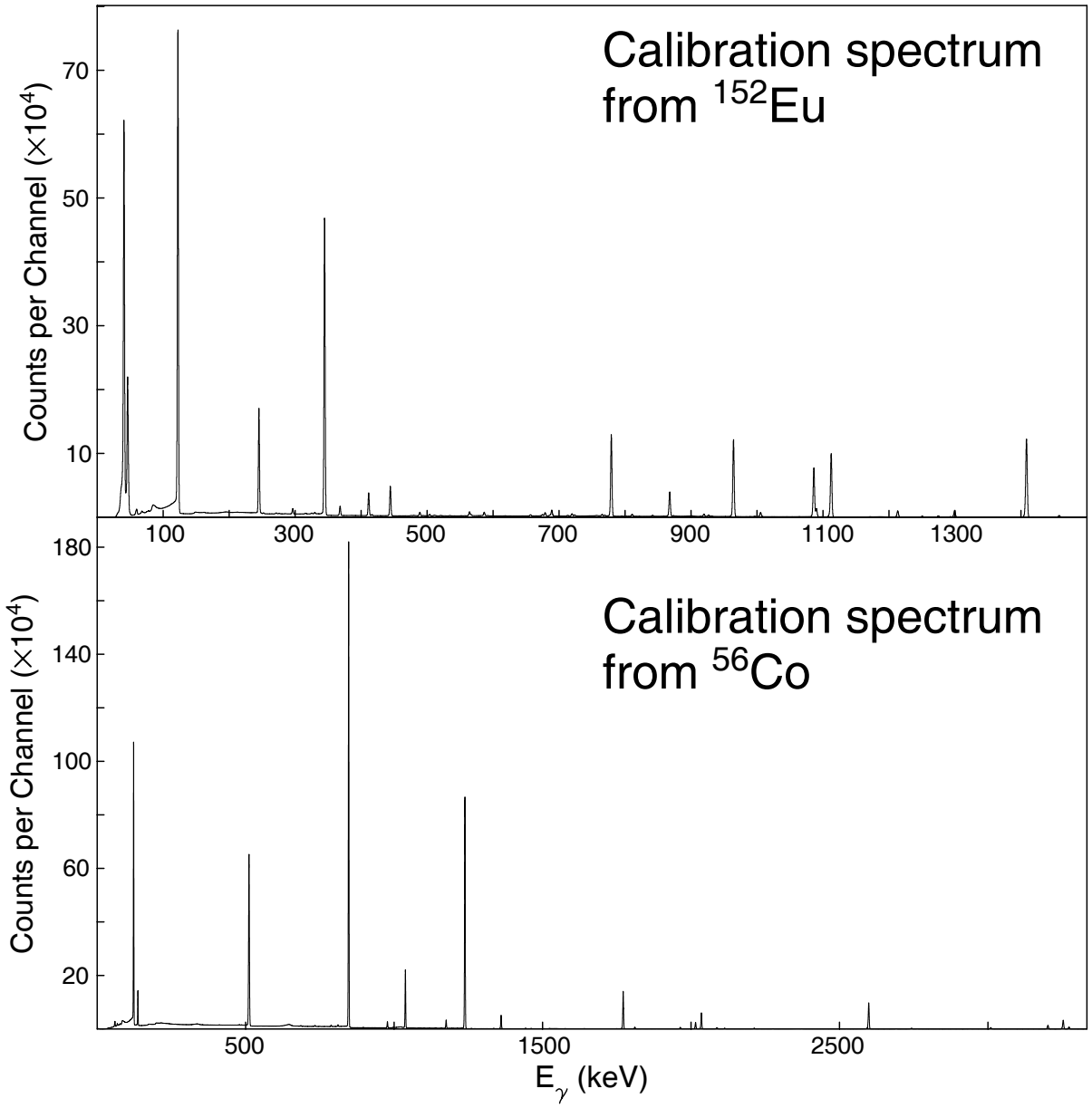

Figure 14: Calibration spectra from ^{56}Co and ^{152}Eu sources

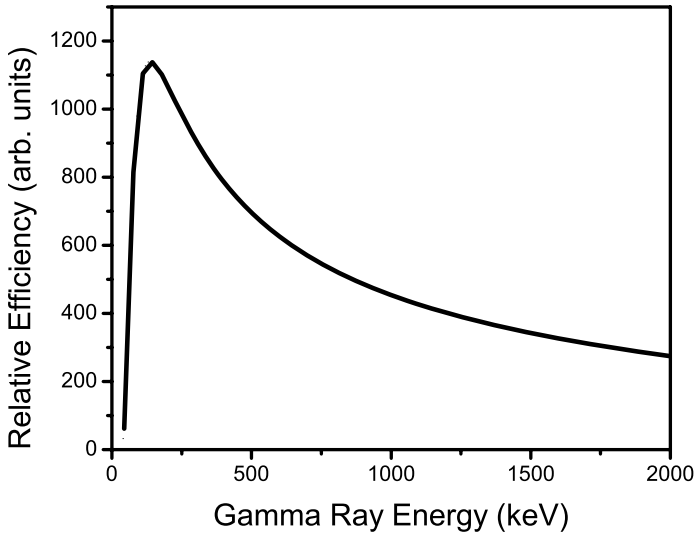

Figure 15: Gammasphere efficiency curve in arbitrary units

Coincident γ-ray measurements

The most powerful tool at our disposal for refining γ-ray spectra is to use coincidence gating. To do that, we must first construct a coincidence cube of our γ-ray events. This is done by creating three-fold coincident events from γ-rays that are detected within our coincidence time window. The energy of each of the three γ-rays is placed along an axis of the cube, and a histogram of counts is built.

As an example, consider a case where three γ-rays of energies E_1, E_2, and E_3 are detected within the time gate. In our coincidence cube, a count is added at (E_1,E_2,E_3) with a coordinate of E_1 along the first energy axis, E_2 along the second energy axis, and E_3 along the third energy axis. Every three-fold or higher event is thus sorted, creating our full γ-γ-γ cube. Each axis is constructed symmetrically, so N (E_1,E_2,E_3) = N (E_2,E_1,E_3) = N (E_3, E_2,E_1) and so on.

The analysis of the cube data was performed by the RADWARE software package [Rad95]. This software provides programs to sort data events into histogram matrices and cubes. These can then be gated to create coincidence spectra to specifications. Analysis of peak shapes and background spectra are performed with included software packages as well.

This cube is of great use because transitions that are closely associated with each other typically occur within a very short time span of each other. By setting a coincident time gate wide enough to include these events but not others, we can dramatically increase the relative strength of associated events. For example, most nuclear states de-excite in less than a nanosecond. By setting a time gate of 100 ns, we will lose virtually no true prompt coincidences, while filtering out a vast majority of random events. We will be left with transitions from the same nucleus as our gate, as well as from the corresponding fission fragment partner.

For a closer look, let's consider a test case. Looking at the excited levels in ^{144}Ba, we see a ground state band cascade as shown in Figure 16. All of these transitions should be in prompt coincidence, as a nucleus created in the 16^+ excited state will cascade through each of these levels in a very short period of time, emitting all the γ transitions down to ground.

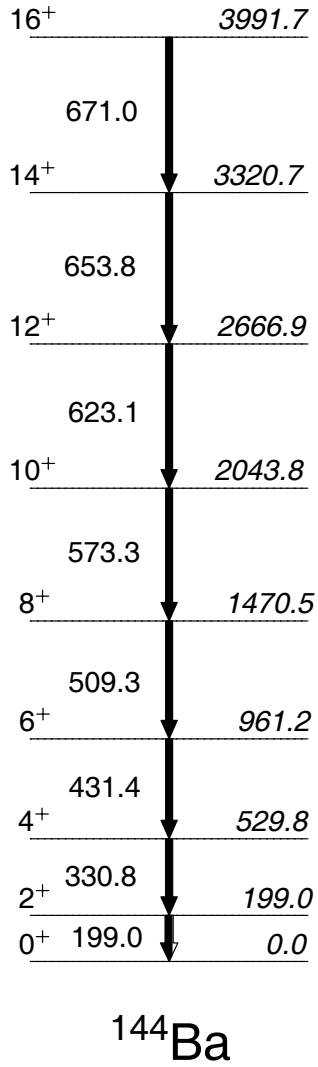

Figure 16: ^{144}Ba ground state band

Examining the γ-γ-γ cube with a series of spectra, we can observe the effect of successive coincidence gating. The bottom spectrum in Figure 17 is the full projection of the cube onto one axis. There are many strong peaks present, as well as a high level of background. Evaluating the stronger peaks is possible, but the less populated nuclei will be invisible. The second spectrum is with a single γ-ray gate of 671.0 keV. This is a transition in ^{144}Ba. We immediately see the counts are much lower, with a few peaks standing out more than others. However the true difference appears when we apply a full double gate on ^{144}Ba by using 671.0 and 199.0 keV gates in the topmost spectrum. Here, the background has been reduced to almost nothing, and several peaks stand out clearly. These peaks all belong to the same cascade in ^{144}Ba (653.8, 623.1, 573.3, 509.3, 431.4, 330.8 keV). Notice how peaks that could not even be observed in the projection spectrum are now easily identifiable as belonging to the same nucleus. Also, the intensity of the 653.8 keV peak is slightly abnormally high (stronger than the 623.1 keV transition) due to minor contamination in the 199.0 keV gate region.

Some of the weaker transitions in ^{144}Ba are also present and are labeled in smaller font. The transitions from two of the Mo partner isotopes are present (^{104,106}Mo). Transitions from ^{103}Mo (102.8 keV) and ^{105}Mo (95.3 keV) are below the energy range in this spectrum. An important note is that ^{144}Ba is one of the most strongly populated nuclei in the entire ^{252}Cf spectrum. For rare nuclei, this technique is even more important to resolve small peaks from the background.

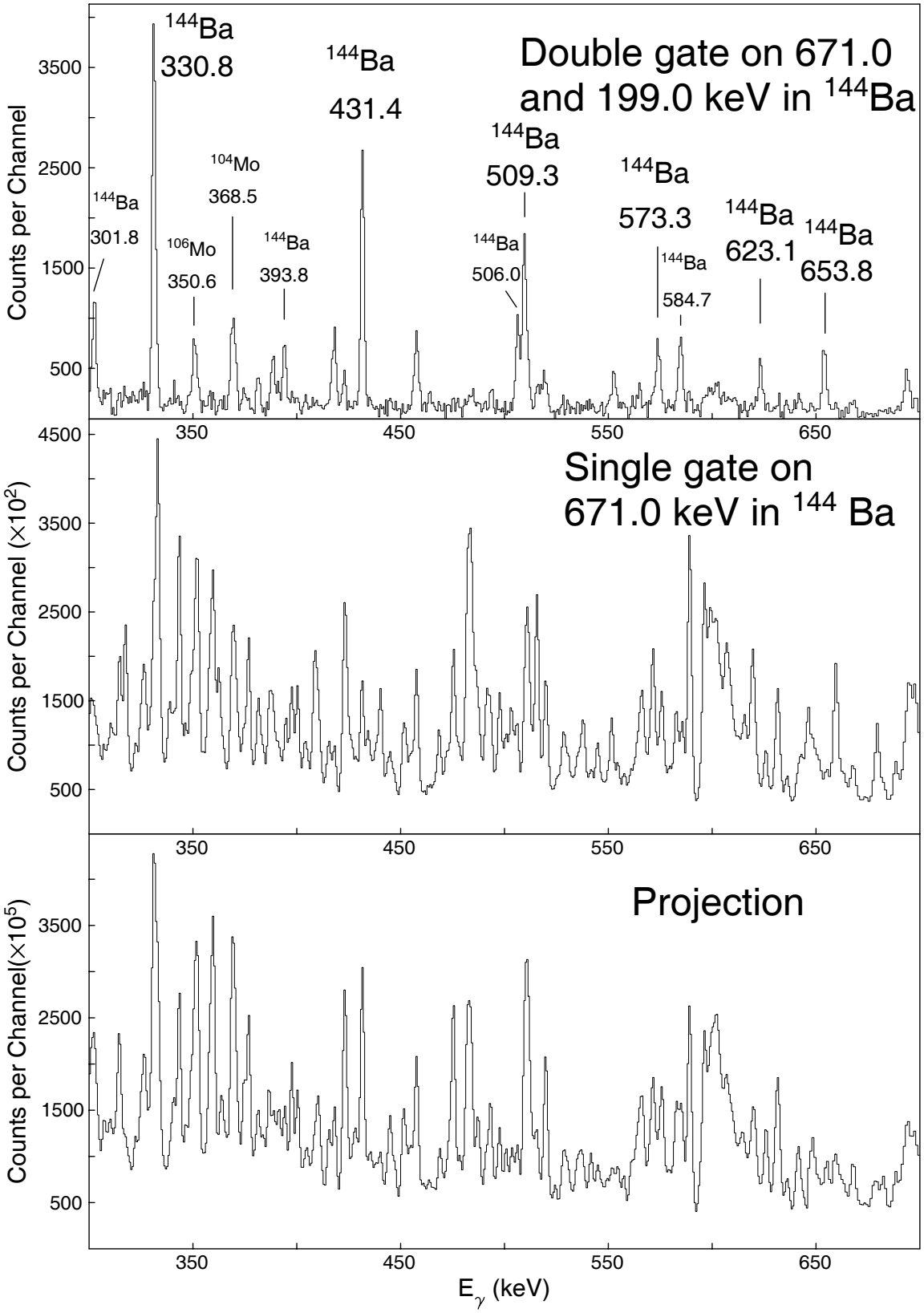

Figure 17: Triple coincidence gating series in ^{144}Ba

Level scheme construction

By systematically examining different energy gates, we can construct a clearer picture of the excited levels in a nucleus. Creating these levels schemes allows us to establish the structure of the nucleus. Without an organized level scheme, we only have a list of gamma ray transitions coming from a specific nucleus. Once these transitions are ordered with respect to one another, we can identify important band structures and understand the behavior of the nucleus in terms of nuclear models. Sorting out the spectra into complex level schemes requires many analytical tools that have been developed for gamma ray spectroscopy.

Previously known experimental results

In order to begin the analysis, we must have something on which to build. Without any known γ-rays in a nucleus on which to gate, it is difficult to assign coincident spectra to that nucleus. The simplest occurs when another experiment has identified one or more γ-rays in the nucleus of interest. In many cases, β^- decay experiments have identified the low energy excited levels and their γ-ray decay energies. In other cases, ion beam γ-ray studies have identified transitions associated with a particular nucleus. With these levels in hand, we have a set of gating partners for our γ-γ-γ cube. With our new higher statistics data, it is then possible to identify new higher energy levels and new bands in the level scheme.

Starting from the few known transitions, we can set gates on these transitions and look for a self-consistent set of new transitions that appear in coincidence with these and each other. For a well-populated nucleus, this can sometimes be simple, as a well-gated

spectrum will show intense peaks from several of the transitions from higher spin states. More exotic nuclei can be more difficult, as the lower population makes the peaks harder to identify.

Fission partner identification

The other way to identify new isotopes is to rely on their fission partner. The corresponding fission partner is created in coincidence with the fragment of interest. This is a straightforward consequence of the finite and conserved number of nucleons involved in the fission. So in a spectrum gated on transitions in one element, the transitions from the partner nuclei will be visible as well. These will be less intense than the transitions from the gated nucleus. Also, every possible partner will be present in the spectrum. Several different partner fragments can be created in coincidence with any isotope depending on the number of neutrons evaporated in the fission. As an example, double-gating on transitions in ^{106}Mo in Figure 18, we can see various barium partner transitions in addition to those in ^{106}Mo (small font). Weaker transitions are also visible from the fission partner barium isotopes. One can now gate on the barium transitions from each isotope to study the nucleus. We can check the assignment of transitions to a particular isotope by gating in transitions in other Mo isotopes and comparing intensities with the expected yields for each partner.

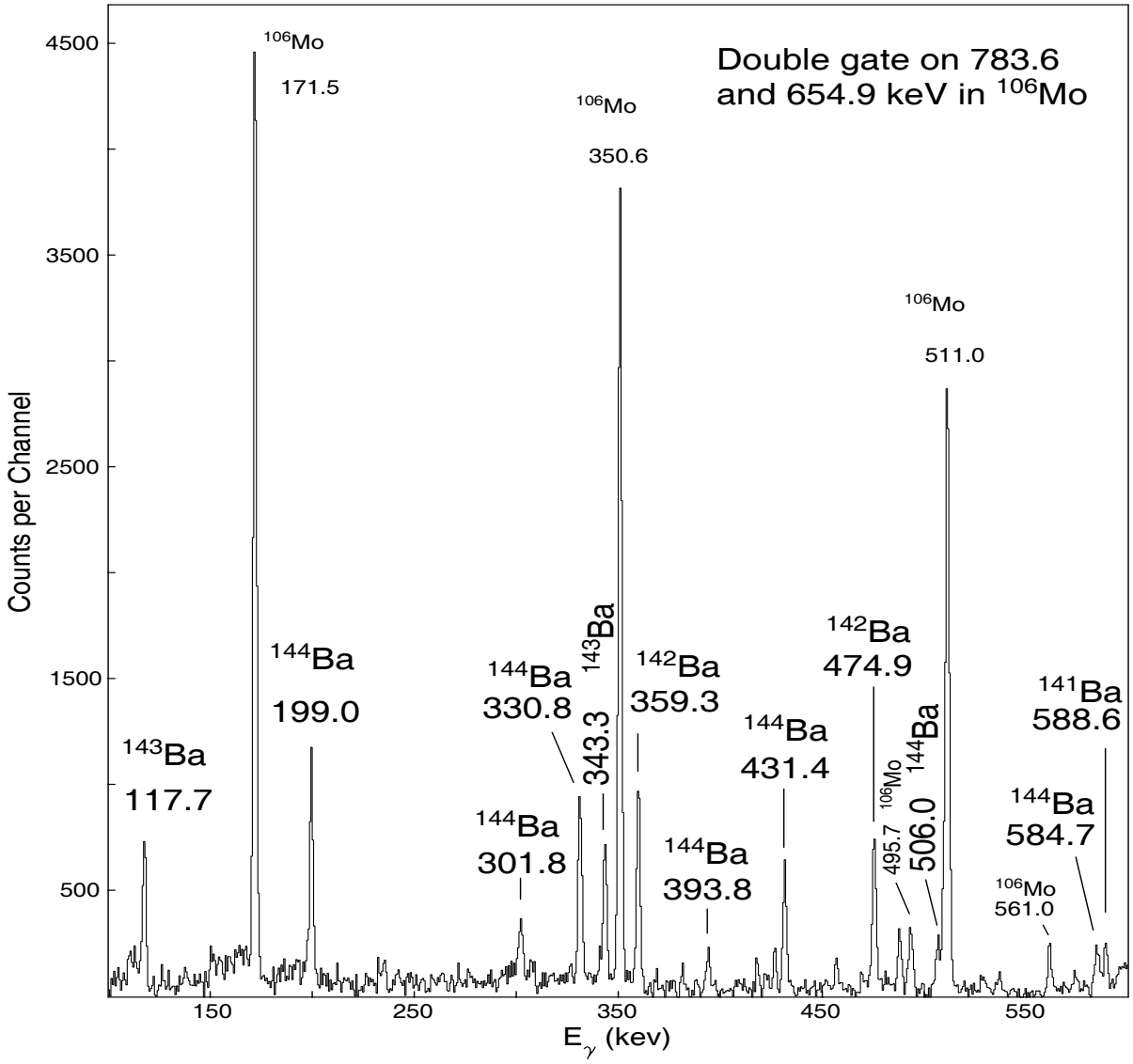

Figure 18: Fission partner identification in ^{106}Mo

Cascade versus parallel

Transitions that are in cascade with each other will appear in coincidence, while transitions belonging to a different cascade parallel to the first one will not appear. A single excited nucleus can only de-excite along one possible path, so parallel transitions will not be emitted by any single nucleus. These different cascades can be built into

multiple excitation bands by gating on transitions in each band. By observing which transitions are in coincidence with each other and which are in parallel, we can identify parallel band structures in addition to ground state bands. There are often crossings between bands and further side bands that can be identified with a careful analysis of several different gate transitions.

X-ray information

The electron orbitals for each element are well known from atomic physics. Transitions between these orbitals by excited electrons result in emission of x-rays. These x-rays carry a characteristic energy that is typical of the element. In fission fragments, the de-excitation of levels can involve emission of a γ-ray as previously discussed. But a competing process is internal conversion, where an electron is excited out of its orbital by the energy released by the excited nucleus. This opens up a hole in the electron orbital for an electron to de-excite and emit an x-ray in transition. By observing these x-rays in coincidence with unknown γ-ray transitions, we can often determine the species of nucleus associated with the transition. An example of x-ray peaks in a γ-ray spectra can be seen in the ^{152}Eu spectra in Figure 12. Europium has K-line x-rays at 41 keV.

Assigning J^{π}

Assigning spins and parities (J^{π}) to nuclear levels is often a difficult process. Ground state spins and parities are deduced using shell structures and regional systematics. From direct measurements of electron conversion coefficients, the multipole

nature of nuclear transitions can be determined. The multipolarity of an electromagnetic transition reflects the spin and parity of the nuclear levels involved in the transition. The intrinsic spin of the photon is one, and thus the angular momentum change for a γ-ray transition must be integral. Between an initial state with a spin j_i and a final state with a spin j_f, the transitions must carry an angular momentum j where $|j_i - j_f| \leq j \leq j_i + j_f$. This angular momentum transfer defines the multipole order of the transition. j = 1,2,3,... are called dipole, quadrupole, octupole, … moments.

If we also examine the parity of the nuclear levels, we can determine the multipole type. For a parity change of $(-1)^j$, the nucleus couples to the electric field of the photon, and it is an electric transition. For a parity change of $-(-1)^j$, the nucleus couples to the magnetic field of the photon, and it is a magnetic transition. The transition type is listed with the electric or magnetic type, followed by the order of the transition. So an electric, j=2 transition is called an E2 transition.

For a given pair of nuclear levels, there are usually many possible multipole orders for the transition. The half-life of the transition can be estimated depending on the type of transition. The lowest order multipole almost always dominates, making the contribution of higher orders very small. Some single-particle estimates can be found later in this chapter. For example, consider a transition between a state with a J^π of 4^+ and a state with a J^π of 2^+. The allowed range of j for the photon is between 2 and 6. Since there is no parity change, the possible multipole transitions are E2, M3, E4, M5, and E6. However, since the lifetime of the higher order transitions will be so much longer, in practice, this will usually be an E2 transition with a possible minor contribution from an M3.

The exact ratio of the competing internal conversion and γ-ray de-excitation is determined by the electromagnetic multipole of the transition. This internal conversion coefficient (α) can be compared to theoretical curves for various types of transitions, as seen in Figure 19 [Fir96].

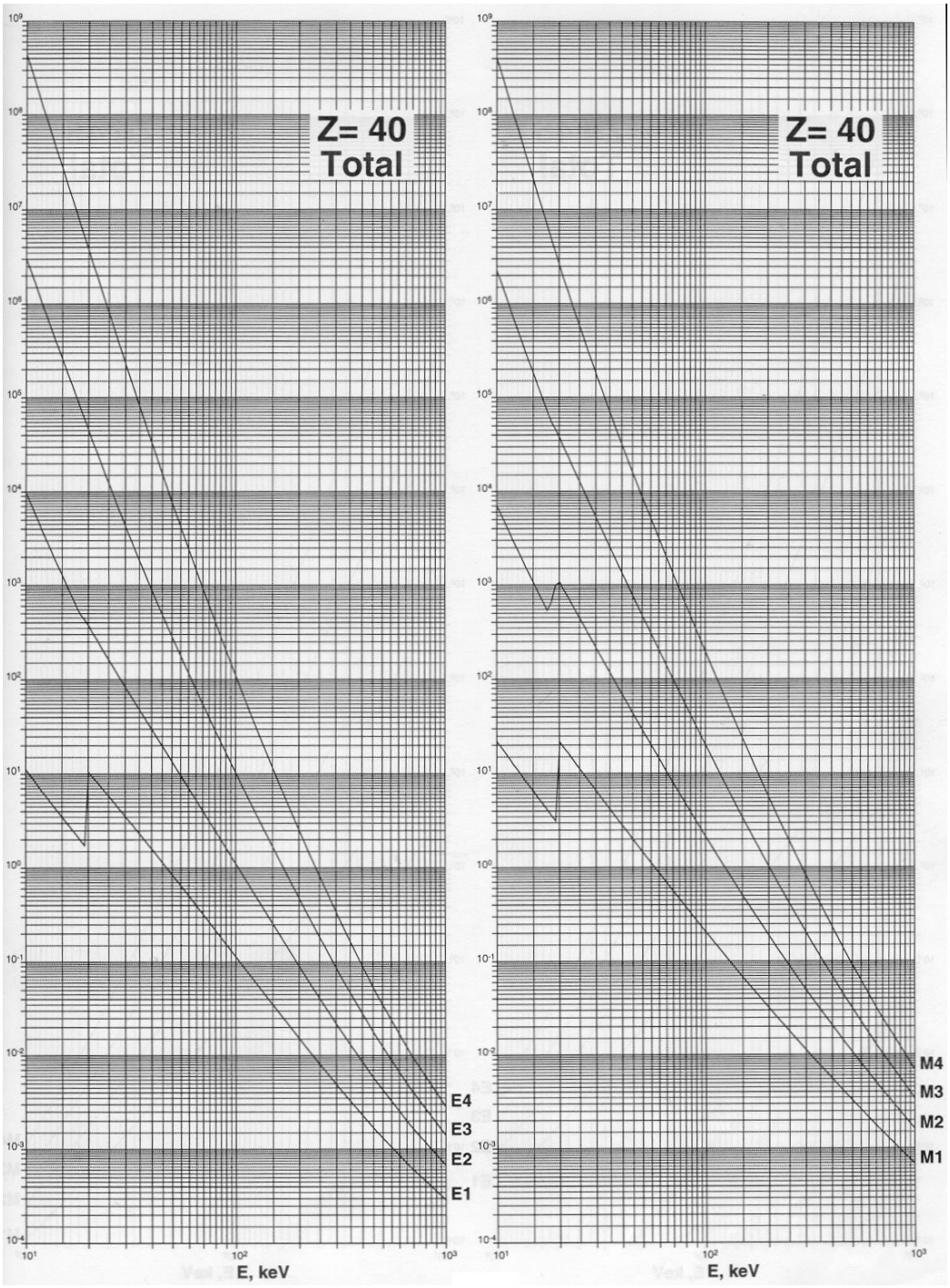

Figure 19: Internal conversion coefficient curve [Fir96]

Transition intensity

Another tool in γ-ray spectroscopy is a careful analysis of transition intensity. The relative intensities of various γ-rays give us important information about their locations in the level scheme. As an example, in a simple cascade like the one shown for ^{144}Ba, transitions out of higher spin states will appear less intense than the ones nearer the ground state. This is due to the fact that a nucleus populated with high spin will transition through all the low spin states on the way to ground. So every nucleus created will go through the bottom transitions, but only the ones statistically created with high spin will emit transitions from higher levels.

Band crossings are usually less intense than transitions within a band. This can be an indicator of how to build up the transitions in correct order. Also, the weaker side bands will be less intense than the stronger ground bands. By carefully comparing transition intensities in addition to the gating patterns, we can determine the positioning of many excited levels giving us a more detailed picture of the nucleus.

Coincident LCP - γ-ray measurements

In the experiments with LCP detectors, we have ternary particle information as well as γ-ray data from Gammasphere. Using coincident gating is also useful with these data. Instead of a γ-γ-γ cube, we construct an γ-γ matrix in coincidence with each type of LCP. The statistics are much lower than the γ-γ-γ cube, but ternary signals are much enhanced. This is easily seen by comparing the signals from a ternary partner. With γ-γ-γ data, the binary fission partner is dominant in the spectra when compared with the rare

ternary partner. Signals from ternary fission are enhanced by using the LCP gated γ-γ matrix.

In a double γ gate on ^{144}Ba, the ternary fission partner that is created along with an α particle are the Zr isotopes. The strongest transition in ^{100}Zr is at 212.6 keV. A pair of spectra is shown in Figure 20. Using the γ-γ-γ cube and double gating on ^{144}Ba (199.0 and 330.8 keV), we see virtually nothing above background at 212.6 keV in the top window. In the bottom window, this is the spectrum from the γ-γ matrix in coincidence with an α particle. Gating on one transition in ^{144}Ba (199.0), we can clearly see a strong peak at 212.6 keV from a transition in ^{100}Zr.

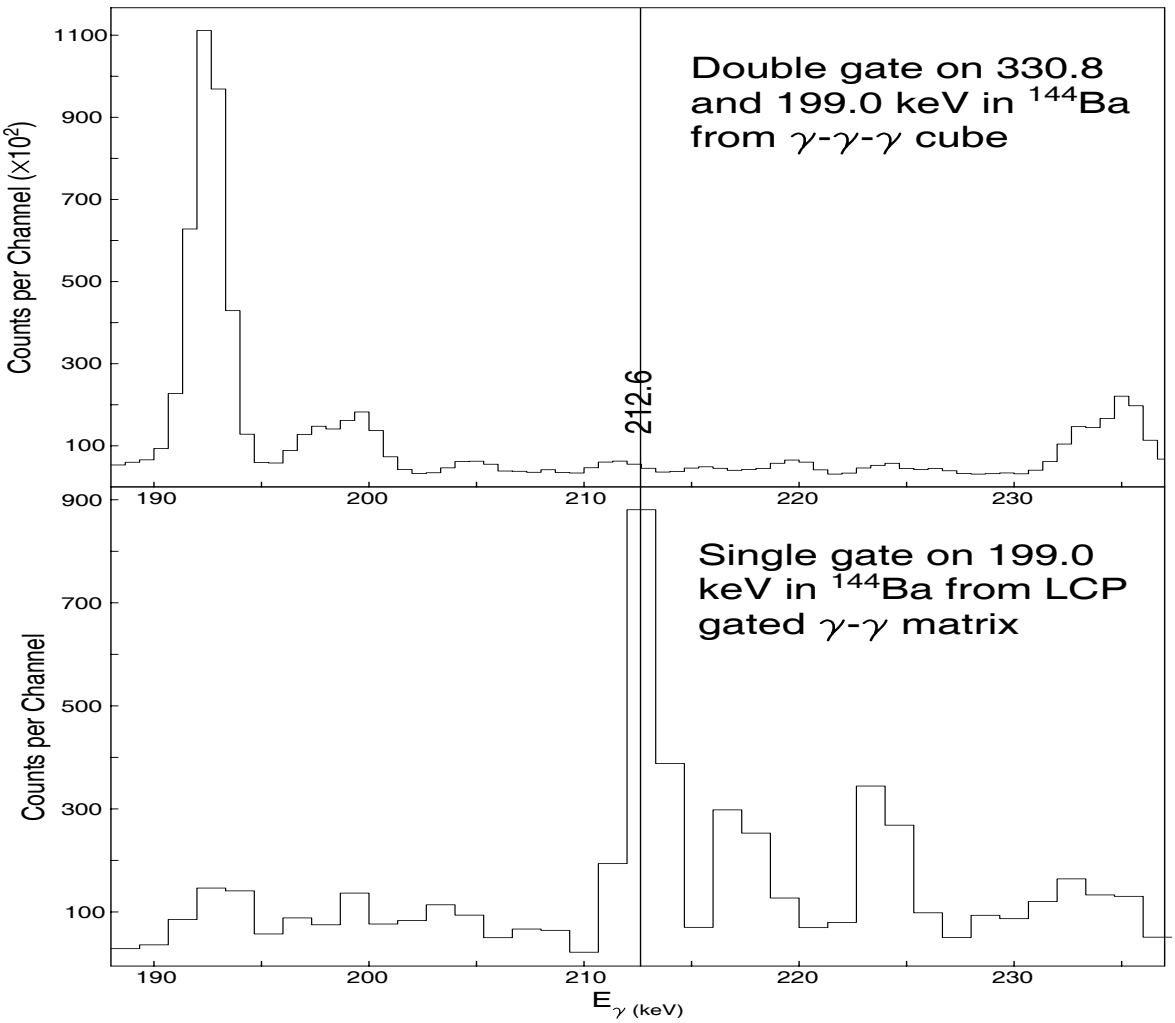

Figure 20: Comparison of γ-γ-γ spectrum with α-gated spectrum showing 212.6 keV transition in ^{100}Zr

Timing analysis

Using time information to construct coincidence gates is a useful analytical tool. Fortunately for the experimentalist, the exact time gate chosen is an offline analysis. Different time gates can be chosen to closely examine and compare signals. By varying the width of the time gate, we can effectively control the balance between background random coincidences and real coincidences. Sometimes narrowing a time coincidence

window will improve our ability to isolate a small peak in the spectrum. The longer time window will have more counts, but the shorter gate may have more clear peaks. This can help resolve weak signals and doublet peaks that might otherwise be difficult to analyze.

In addition to selectively cleaning up spectra, the direct time information is useful for understanding the structure of the nuclei. While most nuclear levels de-excite promptly, some have measurable half-lives of several nanoseconds or greater. Some half-lives can be directly measured from fission data, and others are known from other experiments. These data can be combined with transition intensities and patterns to construct level schemes.

Theoretical calculations of level half-lives are available in reference texts for what are called single particle or Weisskopf estimates [Fir96]. This estimate is based on the behavior of a single excited nucleon completely independent of the rest of the nucleus. These rarely correspond exactly to experimental results, due to shell and collective effects which can hinder or enhance the single particle estimate. However, they are quite useful as a comparison tool. The higher order multipole transitions have a longer half-life than the lower order transitions as mentioned earlier this chapter. A state that only decays via an E3 γ-ray will have a much longer half-life than a similar state than decays via an E2 γ-ray. Electric (E) and magnetic (M) single particle half-life estimates are given by the following equation [Bla52].

$$t_{\frac{1}{2}}(\gamma_E) = \frac{(\ln 2)L[(2L+1)!!]^2\hbar}{2(L+1)e^2R^{2L}}\left(\frac{3+L}{3}\right)^2\left(\frac{\hbar c}{E_\gamma}\right)^{2L+1}$$

$$t_{\frac{1}{2}}(\gamma_M) = \frac{(\ln 2)L[(2L+1)!!]^2\hbar}{80(L+1)\mu_N{}^2R^{2L-2}}\left(\frac{3+L}{3}\right)^2\left(\frac{\hbar c}{E_\gamma}\right)^{2L+1}$$

L = multipole order R = nuclear radius (=1.2x10^{-13}A$^{1/3}$ cm)

μ_N = 1.5922x10^{-39} (keV cm^3) E_γ = energy of the transition (keV)

Level lifetimes provide additional information to help assign nuclear level energies and level spins and parities. Prompt γ-ray transitions usually link levels separated by one or two units of angular momentum. Higher order transitions will usually have longer lifetimes, and thus will be much weaker in narrow time window spectra.

CHAPTER IV

HALF-LIFE MEASUREMENTS OF NUCLEAR STATES

Introduction

An excited nucleus can de-excite through a cascade of γ-ray transitions. These γ-rays carry off energy and angular momentum until the nucleus reaches the ground state. Most nuclear levels are extremely short lived and decay almost instantaneously. In some nuclei, the first excited state has a measurable lifetime. From these lifetimes, the ground state deformation can be calculated. In cases such as strongly non-spherical nuclei, large spin and/or parity changes retard the transition lifetime.

The half-life measurements of first excited states have previously identified nuclei with medium masses that have large ground state deformations. Neutron-rich nuclei with A~100 have been observed with a large deformation [Ham95]. To further probe this region, new measurements are required. Many nuclei can be produced in SF of ^{252}Cf, and with a new analysis technique we are able to measure many half-lives.

Existing measurements

Many of the neutron-rich nuclei have not had any of their excited level half-lives measured. As mentioned before, designing an experiment to study a specific nucleus is time-consuming and expensive. Fission studies can easily populate many isotopes, but timing measurements are more difficult. With an ion beam implantation experiment, the exact time of implantation is directly measured. By examining the timing of the decay

products or the de-excitation emissions, the half-life of a state can be extracted. In a fission experiment, there is no time stamp for the creation of the excited nucleus, so the decay signals do not follow a traditional decay curve.

Many nuclei populated in SF have no measurements on excited level half-lives, while many of the measured half-lives have not been examined recently. Some of the quoted half-lives of states come from experiments done over 30 years ago ([Che70], [Wat70], [Cla73], [Jar74], [Che80], [Sch80]). These results are tabulated in Table 2. While these experiments were advanced for their day, the progress in experimental techniques and equipment makes possible more reliable and accurate measurements. We report more reliable and accurate half-life measurements of both previously measured and previously unknown half-lives. It should be noted that in the case of ^{143}Ba, the ENSDF average reports a measurement that does not correspond to the actual referenced paper. Most likely, the best measurement is therefore 3.8(12) ns.

Table 2: Tabulated previous half-life measurements (in ns)

Nucleus	ENSDF	Literature Values			
^{98}Sr	2.78(8)	2.80(8) [Mac89]	2.74(12) [Ohm87]	4(1) [Sch80]	
^{102}Zr	1.91(25)	1.71(14) [Che80]	3.17(25) [Che73]	1.7(3) [Wat70]	0.86(18) [Che70]
^{137}Xe	8.1(4)	8.1(4) [Cla73]			
^{143}Ba	3.5(8)	3.8(12) [Sch79]	6(2) [Cla73]		

This re-examination becomes even more necessary when the previous measurements are examined in detail. In some cases, no data are shown, only the resulting level half-life. These must be assumed to have large uncertainties. Where data are shown, the statistics are seen to be unimpressive, leaving wide room for interpretation

on the fit. As an example, Figure 21 shows the half-life measurement of the first excited state in ^{143}Ba measured in 1979 [Sch79]. No error bars are included with the points, but the uneven nature of the data is apparent. The resulting half-life has a quoted uncertainty of 30%.

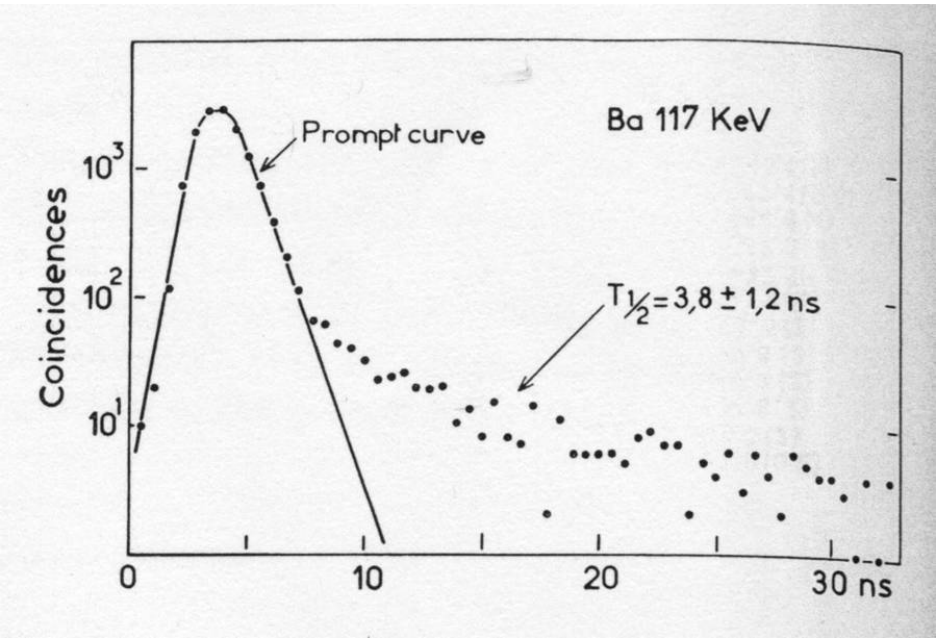

Figure 21: Decay curve of 9/2$^-$ state in ^{143}Ba [Sch79]

Nuclei like ^{143}Ba are not particularly exotic species for our current experimental techniques to reach. We should be able to populate and study many isomeric levels with high statistics. With some of these nuclei having no measurements and others with the above level of uncertainty, new studies of these nuclear level half-lives populated in SF can provide new insights.

Triple γ coincidence technique

With our large data sets from ^{252}Cf fission, we can easily observe the transitions in many nuclei of interest. But the timing spectra do not follow a simple logarithmic decay that would rise from triggering on the creation of the nuclei. Our data cubes are triggered by any γ-ray, so the simple way of fitting the transitions to a decay curve cannot be used. In order to measure the half-lives of the excited levels in nuclei populated in our SF data, a new technique is required.

The triple-γ coincidence technique was developed at Vanderbilt by Dr. Jae-Kwang Hwang. By taking advantage of our γ-γ-γ cube and the timing information of the events, we can use our previous fission data to measure the half-lives of many of the nuclei created. The power of this technique is that the fission data sets include dozens of neutron-rich nuclei that can be examined. This replaces a large number of ion beam experiments and provides powerful new insights by using already recorded data.

Instead of measuring the time between the creation of the excited nucleus and the emission of a de-excitation γ-ray, we have all the γ-rays that are in coincidence with each other. Even though we do not have the "start" trigger, we can rely on the relationship between the timing of γ-rays emitted in cascade with each other. Extremely short lived states will decay promptly, while longer lived states will have a delay. This fact is the key to measuring level half-lives with γ-γ-γ data.

Consider a short cascade of four γ-rays in Figure 22. Now further assume that the three states de-populated by γ_3, γ_2, and γ_1 are very short lived. The state we will measure is the first excited state, the level of interest (L.O.I.). In our γ-γ-γ cube, we can gate on any two of these four transitions and expect to see both the other transitions.

Unfortunately, that will prove only what we already know: that these transitions form a coincident cascade. In order to learn something more about the lifetime of the levels, we need to use the timing information more subtly.

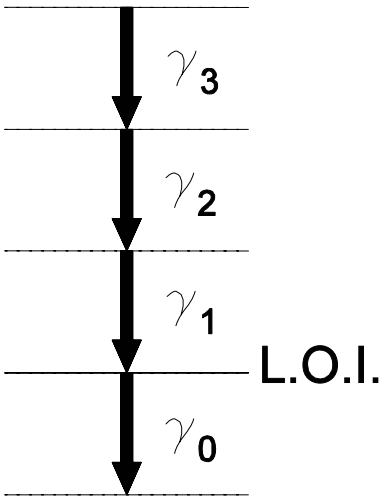

Figure 22: Sample γ-ray cascade

Fortunately, we can construct our coincidence cube using any time window we choose. In fact, we constructed a series of time gated cubes with increasing coincidence windows. These cubes have windows of 8, 16, 20, 28, 48, and 72 ns. This means we can selectively allow more or less time to pass between the detected γ-rays in our coincidence definition. This is then used to measure the half-life of the excited level. With the other transitions all being emitted promptly, the rate limiting step in the cascade is the half-life of the L.O.I. If this is long-lived, γ_0 will be emitted much later than if the level is very short-lived.

We set a double gate on two of the transitions above the level, such as γ_3 and γ_1. In the resulting spectrum, we see both γ_2 and γ_0 strongly. The absolute intensity of γ_0 will be determined by an exponential relationship relative to the intensity of γ_2 and the half-life of the excited level. This is a result of the statistical nature of the decay process. We are effectively setting the condition that the nucleus passes through the excited level of interest by choosing our double gate above that level. The rate of de-excitation is reflected in the detection of the γ_0 transition.

$$\frac{N(\gamma_0)}{N(\gamma_2)} = C(1 - e^{-\lambda t_w})$$

N = intensity C = constant λ = decay constant t_w = time window

By measuring N(γ_0) and N(γ_2) with a series of different time windows, we can extract the half-life of the excited level by fitting the ratio to an exponential growth curve. An extremely convenient point is that we can use the relative intensities of the measured transitions. We do not have to correct for efficiencies or internal conversion because these factors can all be folded into one multiplicative constant C that has no effect on the exponential decay parameter in the fit. The ratio of the efficiencies will be the same for each time window, allowing us to neglect these factors.

A series of time window spectra is shown in Figure 23. The double gate is taken on two transitions in ^{143}Ba (343.3 and 625.7 keV), and the two remaining transitions in the cascade are shown (117.7 and 493.3 keV). As the time window increases, the relative size of the 117.7 keV peak (N_0) increases with respect to the 493.3 keV peak (N_2). Observe how low the level of background is with the double γ gate. The ratio of intensities can then be plotted as a function of the time window to determine the half-life.

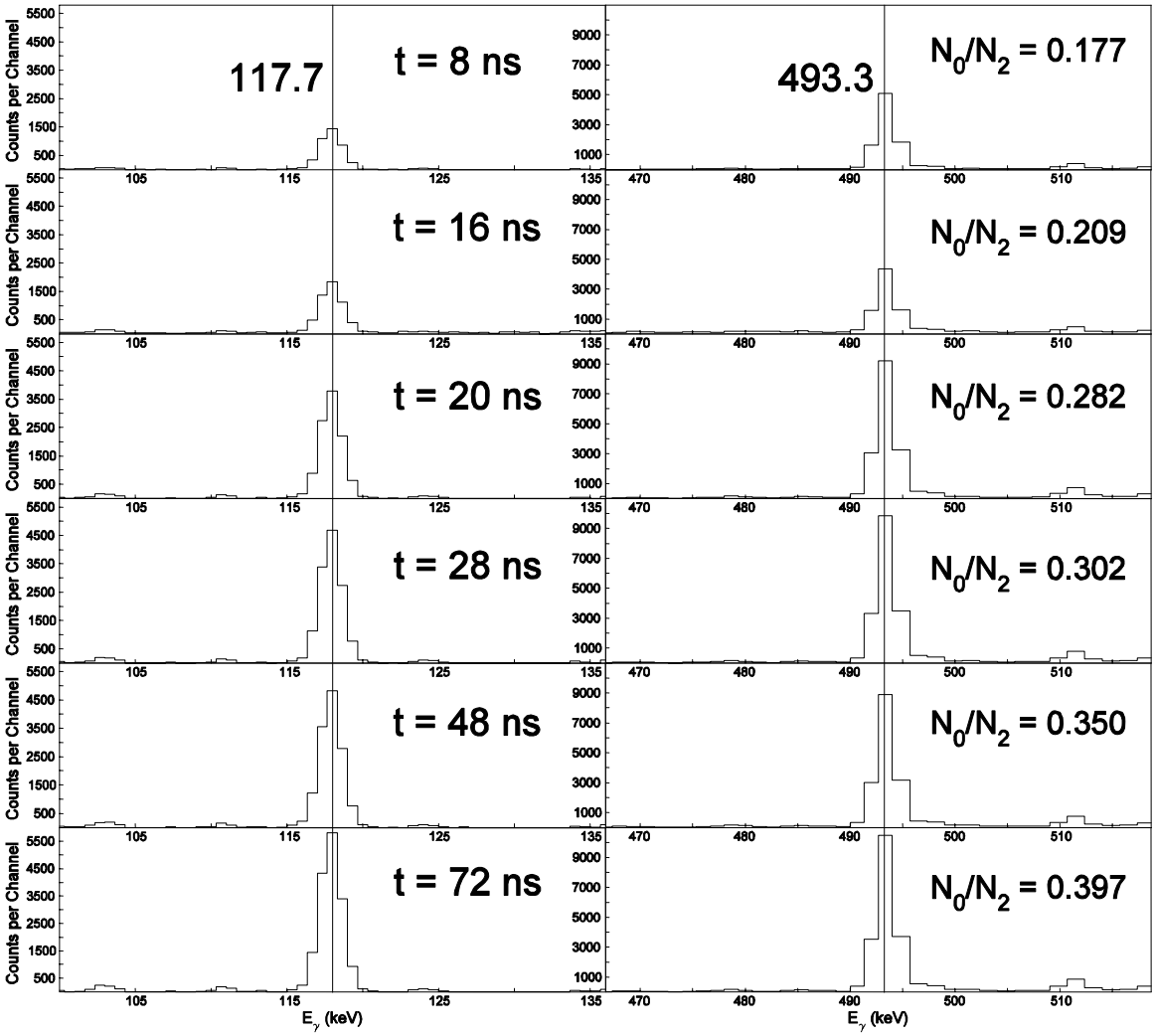

Figure 23: ^{143}Ba peaks (117.7 and 493.3 keV) in 8, 16, 20, 28, 48, 72 ns time windows

New measurements

By using this new triple γ coincidence technique, the half-lives of states in several neutron-rich nuclei were measured. The nuclei selected were known or suspected to have measurable first excited state half-lives, on the order of a few nanoseconds. A half-life measurement was performed on excited states in ^{98}Sr, ^{102}Zr, ^{104}Zr, ^{143}Ba, and ^{152}Ce. In addition, as a longer lived test case, ^{137}Xe was also analyzed, with an excited state half-

life of around 10 ns. For consistency, the results were checked by reversing the gating pattern. Instead of gating on γ_3 and γ_1, the alternate gating pattern is to double gate on γ_3 and γ_2. Reproducing the half-life result is a good systematic verification.

In Figures 24-29, the ratios of the measured γ-ray intensities are plotted as a function of the time coincidence window in nanoseconds. A simple exponential curve is fitted, and the resulting half-life is presented. The energy of the transition and the J^{π} of the states are given in the captions.

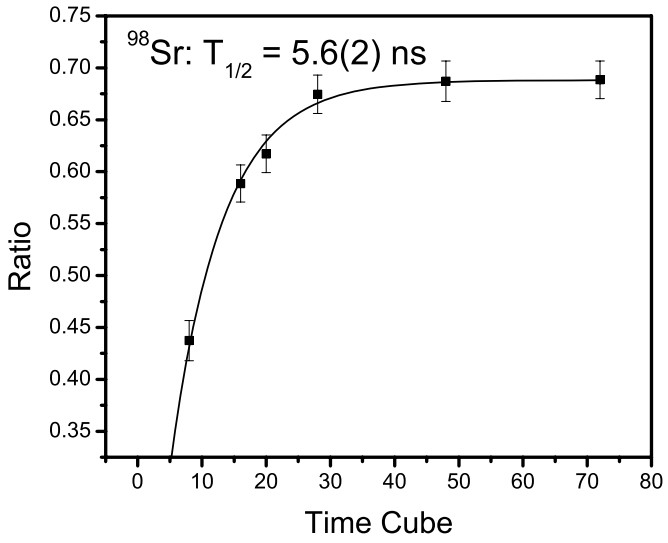

Figure 24: ^{98}Sr half-life curve fitting (E_γ = 144.3keV, $2^+ \rightarrow 0^+$)

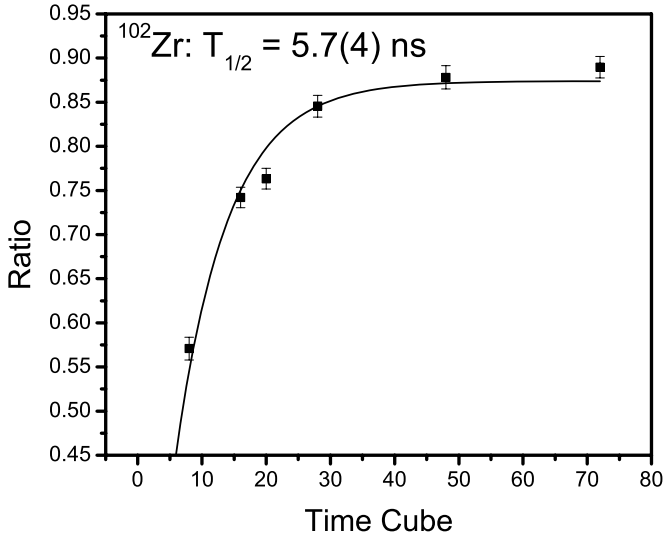

Figure 25: ^{102}Zr half-life curve fitting (E_γ = 151.8 keV, $2^+ \rightarrow 0^+$)

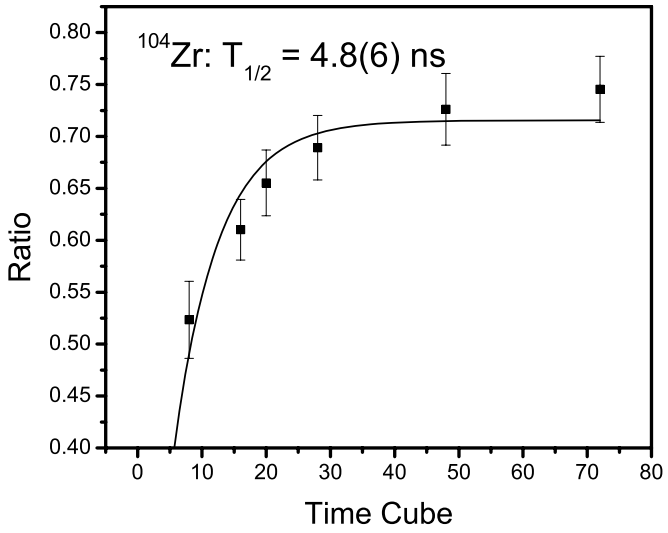

Figure 26: ^{104}Zr half-life curve fitting (E_γ = 140.3 keV, $2^+ \rightarrow 0^+$)

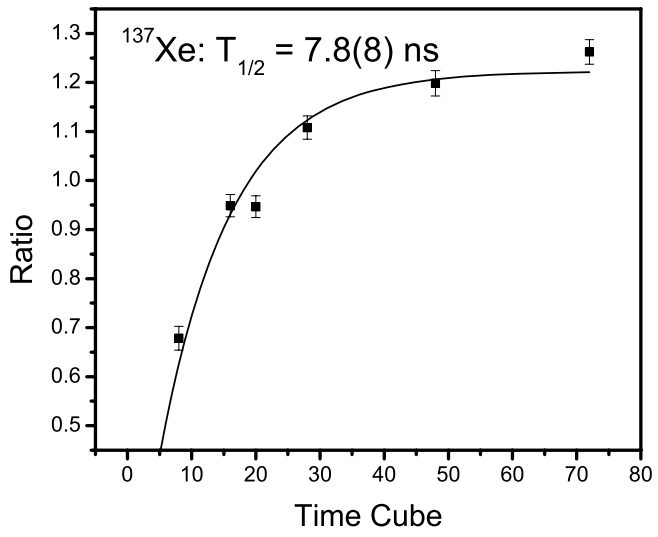

Figure 27: ^{137}Xe half-life curve fitting (E_γ = 314.1 keV, $17/2^- \rightarrow 13/2^-$)

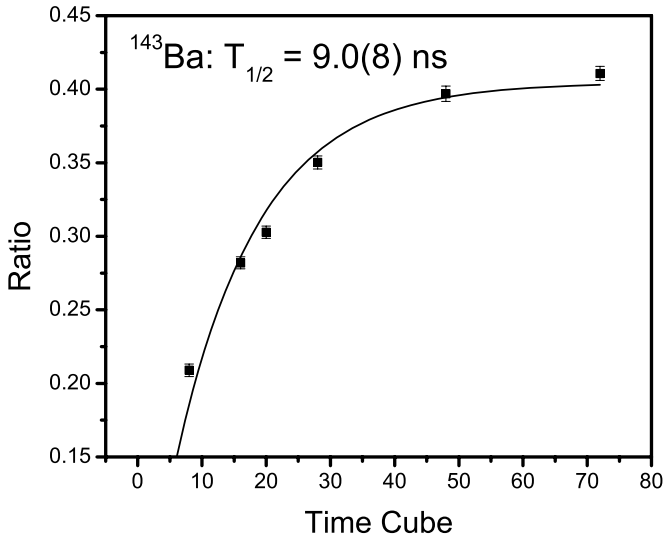

Figure 28: ^{143}Ba half-life curve fitting (E_γ = 117.7 keV, $9/2^- \rightarrow 5/2^-$)

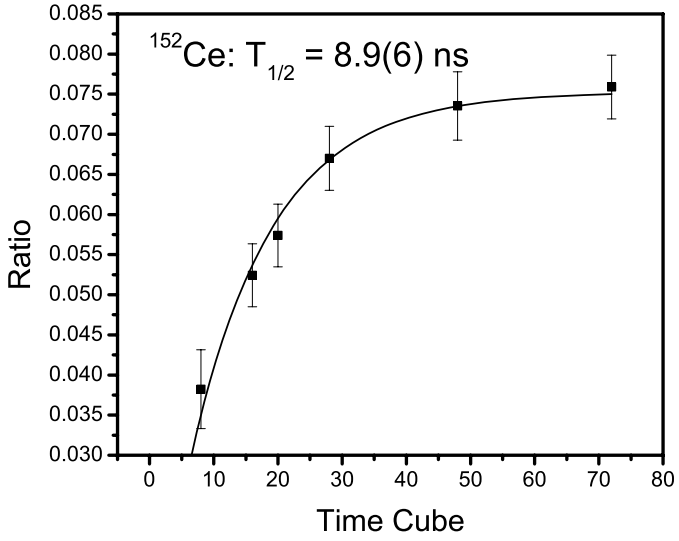

Figure 29: ^{152}Ce half-life curve fitting (E_γ = 81.7 keV, $2^+ \rightarrow 0^+$)

Discussion

It is believed that the short time scale calibrations for low energy transitions have introduced some systematic errors in the timing of the detectors. We applied an exponential curve fit and an alternate linear correction to the data and extracted the experimental half-lives for these excited levels. They are all in the range of 4 – 10 ns. The errors are in the range of 5 – 10% based on the statistical errors from the data, peak fitting, background subtraction, and curve fitting.

A problem arises when we compare our new half-life measurements to the existing literature. Because of to the imprecision of the old measurements, some disagreement was expected. However, one of the experimental half-life measurements, ^{98}Sr, was performed more recently in 1989 with satisfactory precision [Mac89]. Our measured value differs by a factor of two (2.78(8) versus 5.6(2) ns). This, along with the

fact that not all the fits appear perfectly smooth, indicates that a correction needs to be applied to our measurement. We must compensate for the short time scale inaccuracies after performing the measurement, when the transition energies are low, somewhere below 250 keV.

Correction function

Necessity of correction function

The best way to determine the nature of the correction would be to compare a large number of half-life values. However, the original problem of the inaccurate previous measurements prevents us from using this method. Basing a correction curve on highly imprecise data would be no better than not correcting at all. The one accurate point is the short half-life of the 2^+ state in ^{98}Sr (2.80(8) ns) [Mac89]. This by itself may not be enough to create a correction curve. However, we also know that the same data set was used to measure several long half-lives with half-lives greater than 100 ns, and they are in reasonable agreement with previous results [Hwa04]. In fact, for a nucleus with as short a half-life as ^{137}Xe (8.1(4) ns) [Cla74], our result (7.8(8) ns) is in good agreement.

Our data appear to be most suspicious in the very short half-life region of a few nanoseconds. These correspond to very low energies of the excited states being studied. This has a reasonable physical explanation, as the detector timing response is expected to be least accurate for low energy γ-ray events. The timing signals are generated once a voltage threshold is reached. For a linear response detector, this can be delayed for low

energy signals, since the total charge collected will be small. Accordingly, our correction should be parameterized based on the energy of the detected γ-ray. The relevant γ-ray is the transition de-exciting the level of interest, as this is the signal we are measuring.

To visualize the correction curve we need, compare the ratios of the true known half-life ($T_{1/2}$) with our measured half-life ("$T_{1/2}$"). This ratio should approach unity for high energy, long-lived states, as our data from that region correspond well to the literature [Hwa04]. This ratio should be nearly 1.0 for states as low in energy as the ^{137}Xe excited state (314.1 keV). But for even lower energy states such as in ^{98}Sr (144.3 keV), this ratio is measured to be less than 1.0. Our correction function must be able to account for these features, and hopefully correspond well with the other less accurate previous measurements.

Exponential correction function

Expecting low-energy threshold effects to be relevant, the form of the curve is first postulated to be a simple exponential function. In order to fit the data with reasonable accuracy, two free parameters, a threshold α and an exponential constant β are used.

$$\frac{T_{\frac{1}{2}}}{"T_{\frac{1}{2}}"} = 1 - \exp\left(-\frac{E_\gamma - \alpha}{\beta}\right)$$

By forcing the curve to fit the ^{98}Sr and ^{137}Xe data roughly, we end up with the correction function shown below (α = 70 keV, β = 100keV). The parameters are not an exact fit, more a rough compromise between accuracy and a more physical form. These

constants match up to the two data points within 10%, which is acceptable for an estimated correction curve.

$$\frac{T_{\frac{1}{2}}}{"T_{\frac{1}{2}}"} = 1 - \exp\left(-\frac{E_\gamma - 70keV}{100keV}\right)$$

Applying this correction to our measured data, we present the results along with the average values from the Evaluated Nuclear Structure Data Files (ENSDF) from the National Nuclear Data Center [NNDC] in Table 3 below. Observe the significant improvement we see after applying the correction curve. The magnitude of the correction increases as the energy of the transition decreases. With more accurate data points from independent experiments, this curve may be refined further to improve the accuracy. Half-lives that have not been measured previously are marked "N/A". The error bars on the corrected values include a statistical error plus an assumed error of 0.3 – 0.5 ns based on the comparison of the corrected values with known values.

Table 3: Exponential correction function half-life results

Nucleus	E_γ	J_i^π	J_f^π	Measured $T_{1/2}$	Corrected $T_{1/2}$	ENSDF $T_{1/2}$
^{98}Sr	144.3 keV	2^+	0^+	5.6(2) ns	2.9(4) ns	2.78(8) ns
^{102}Zr	151.8 keV	2^+	0^+	5.7(4) ns	3.2(6) ns	1.91(25) ns
^{104}Zr	140.3 keV	2^+	0^+	4.8(6) ns	2.4(7) ns	N/A
^{137}Xe	314.1 keV	$(17/2^-)$	$13/2^-$	7.8(8) ns	7.1(9) ns	8.1(4) ns
^{143}Ba	117.7 keV	$9/2^-$	$5/2^-$	9.0(8) ns	3.4(6) ns	3.5(8) ns
^{152}Ce	81.7 keV	2^+	0^+	8.9(6) ns	1.0(9) ns	N/A

Linear correction function

The other simple way to parameterize the curve is with a straight line correction. The independent variable is still the energy of the excited state. We assume that the ratio of the measured half-life to true half-life passes through the origin, because the half-life of a state with zero excitation energy is definitionally zero. In addition, the function terminates once unity is reached, to account for the fact that the half-lives of high energy states are measured accurately. The function is given below, with only one free parameter, α.

$$\frac{T_{\frac{1}{2}}}{"T_{\frac{1}{2}}"} = \frac{E_\gamma}{\alpha}$$

To fix the free parameter, we trivially use our one accurate data point for ^{98}Sr. This sets the correction constant α = 288.6 keV. This also sets the domain of the correction to be E_γ < 288.6 keV. For higher transition energies, no correction is applied to our measured results. Correcting our measured results, these are displayed with the ENSDF values in Table 4.

Table 4: Linear correction function half-life results

Nucleus	E_γ	J_i^π	J_f^π	Measured $T_{1/2}$	Corrected $T_{1/2}$	ENSDF $T_{1/2}$
^{98}Sr	144.3 keV	2^+	0^+	5.6(2) ns	2.8(4) ns	2.78(8) ns
^{102}Zr	151.8 keV	2^+	0^+	5.7(4) ns	3.0(5) ns	1.91(25) ns
^{104}Zr	140.3 keV	2^+	0^+	4.8(6) ns	2.3(5) ns	N/A
^{137}Xe	314.1 keV	$(17/2^-)$	$13/2^-$	7.8(8) ns	7.8(9) ns	8.1(4) ns
^{143}Ba	117.7 keV	$9/2^-$	$5/2^-$	9.0(8) ns	3.6(7) ns	3.5(8) ns
^{152}Ce	81.7 keV	2^+	0^+	8.9(6) ns	2.5(7) ns	N/A

Comparison

Both of these correction curves bring the known data in much better agreement with known values. The exponential correction has an uncomfortably arbitrary threshold constant. But it is a strongly physical function with an infinite domain. The linear correction relies strongly on the single well-known data point and reproduces the other values remarkably well with no threshold. The trouble with the linear model is the discontinuity at E_γ = 288.6 keV where the correction function abruptly turns off. Further measurements are required to enhance our understanding of this correction function.

Deformation measurements

With new half-life measurements, we can also measure another important aspect of the nuclear structure in these neutron-rich isotopes. We can use the measured half-life to determine the partial width of the level from various decay channels (conversion electrons and γ-rays of various multipolarities). We measured the total width, which is simply the sum of all the partial widths available to the level. To determine the partial half-life ($T_{1/2}(\gamma)$) of the k^{th} photon de-exciting a level, we must apply some corrections to our measured value.

$$T_{\frac{1}{2}}(\gamma) = T_{\frac{1}{2}} \sum_{i=1}^{n} I_i \frac{1+\alpha_i}{I_k}$$

For our simple cascades, this becomes rather simple, as there is only one transition de-exciting the level, making all the intensity (I_i) factors trivial. Also, the multipole mixing is expected to be small, leaving only the internal conversion to be corrected. This gives us the partial half-life for a single multipolarity γ-ray transition.

With this experimental partial half-life, we can calculate the experimental transition strength. For a state that decays by emitting an E2 transition, the formula is given below in terms of the half-life (ps) and the transition energy (MeV) [Fir96].

$$B(E2)\downarrow = \frac{0.05659}{T_{\frac{1}{2}}(E2)E_{\gamma}{}^{5}}(eb)^{2}$$

The deformation parameter β_2 can then be calculated from the transition strength by using the relationship given by [Ram86]. The equation depends on the B(E2) value calculated from the half-life, as well as the atomic number Z and the mass number A.

$$\beta_2 = \frac{4\pi}{3ZR_0{}^2}\sqrt{\frac{5B(E2)\downarrow}{e^2}}$$

$$R_0 = 1.2A^{1/3}\ fm$$

β_2 is used as a measure of the quadrupole deformation of the nucleus. The mathematical relationship is given by the following [Fir96]. Q_0 is the intrinsic quadrupole moment.

$$Q_0 = \sqrt{\frac{16\pi}{5}}ZeR_0{}^2\beta_2$$

The shape of the deformation is reflected in the value of Q_0, as seen below in Figure 30.

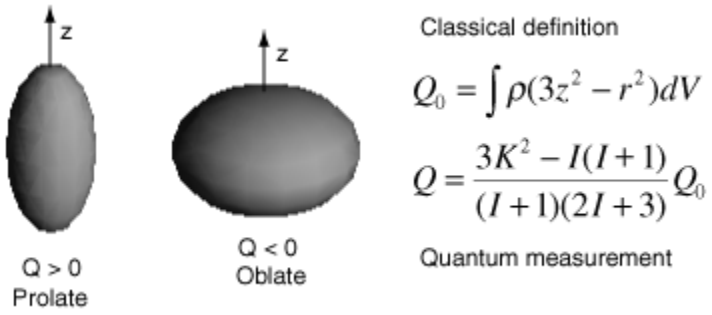

Figure 30: Quadrupole deformation schematic

The β_2 values for the nuclei measured in this experiment are listed in Table 5, along with their half-lives and transition strengths. The half-lives used in this table are from the linear correction function.

Table 5: Deformation parameter calculations

Nucleus	E_γ (keV)	$T_{1/2}$ (ns)	J_i^π	J_f^π	B(E2)↓	β_2
^{98}Sr	144.3	2.8	2^+	0^+	0.26	0.41
^{102}Zr	151.8	3.0	2^+	0^+	0.19	0.32
^{104}Zr	140.3	2.3	2^+	0^+	0.34	0.43
^{137}Xe	314.1	7.8	$(17/2^-)$	$13/2^-$	0.0023	0.02
^{143}Ba	117.7	3.6	$9/2^-$	$5/2^-$	0.0005	0.01
^{152}Ce	81.7	2.5	2^+	0^+	1.17	0.43

Conclusions

By examining our ^{252}Cf fission data, we can study many features of nuclear structure. With the sophisticated time gating available to us, the details of the timing information are valuable in understanding more about the nature of nuclear levels. In

addition to constructing level schemes, with the new triple γ coincidence technique, we can also measure the half-life of some states. These measurements can improve on some old studies, and provide completely new information on others. The first reported half-lives of the 2^+ excited states are reported here for ^{104}Zr and ^{152}Ce.

While the exact half-life depends on the correction function, the measured results can be compared with other results from this same measurement set. In our measurements, the first 2^+ state in ^{102}Zr has a "$T_{1/2}$" of 5.7 ns while the same state in ^{104}Zr has a "$T_{1/2}$" of 4.8 ns. With similar transition energies, this will result in a somewhat shorter true half-life for the 2^+ state in ^{104}Zr even after a correction is applied. This will then lead to a greater deformation in ^{104}Zr compared to ^{102}Zr as seen in Table 4. The first 2^+ state in ^{152}Ce has a measured "$T_{1/2}$" of 8.9 ns, but with a transition of such low energy (81.7 keV), the correction will be substantial. With the linear correction, the half-life is estimated to be as low as 2.5 ns, leading to a large deformation.

With new measurements for the first E2 excited states, we can also calculate the deformation of the nucleus. The deformation parameter β_2 is often used to quantify the quadrupole nature of the nucleus. Some of these nuclei exhibit highly deformed shapes. ^{102}Zr is strongly deformed with $\beta_2 \sim 0.3$. For ^{98}Sr, ^{104}Zr, and ^{152}Ce their ground states are even more deformed, with $\beta_2 \geq 0.4$. These represent the largest ground state deformations in this region of the nuclear landscape and are in the range of what is called super deformation. A recent measurement of ^{102}Sr indicates $\beta_2 = 0.5(1)$ [Lhe95], which is in the same range as these new measurements.

The large deformations in the lower mass region are not unexpected. As mentioned, ^{102}Sr has been known to have a super deformed ground state. In this region,

the gaps between energy levels of nucleon orbitals create regions of shape coexistence. If there is a shell gap for both the proton and neutron orbitals, it has been pointed out that they reinforce each other to drive the nucleus into a deformed shape [Ham89]. This can be seen in Figure 31, with the single particle energy levels plotted as a function of deformation. At large deformation ($\beta_2 > 0.3$), there are noticeable gaps at Z = 38 and 40, and gaps at N = 60, 62, and 64. These gaps correspond to Sr and Zr nuclei in this region. Note ^{104}Zr has 40 protons and 64 neutrons, which have shell gaps at $\beta_2 \sim 0.4$, so their reinforcing shell gaps drive ^{104}Zr to super deformation. The ^{152}Ce deformation is not as clear. There is a shell gap at very large deformation ($\beta_2 > 0.4$) for Z = 58, but the N = 94 region is not well understood. The ε_2 parameter in Figure 31 is related to β_2 by the following. As an example, for ε_2=0.3, β_2=0.35.

$$\beta_2 = \sqrt{\tfrac{\pi}{5}}\left(\tfrac{4}{3}\varepsilon_2 + \tfrac{4}{9}\varepsilon_2^2 + \tfrac{4}{27}\varepsilon_2^3 + \tfrac{4}{81}\varepsilon_2^4 + \ldots\right)$$

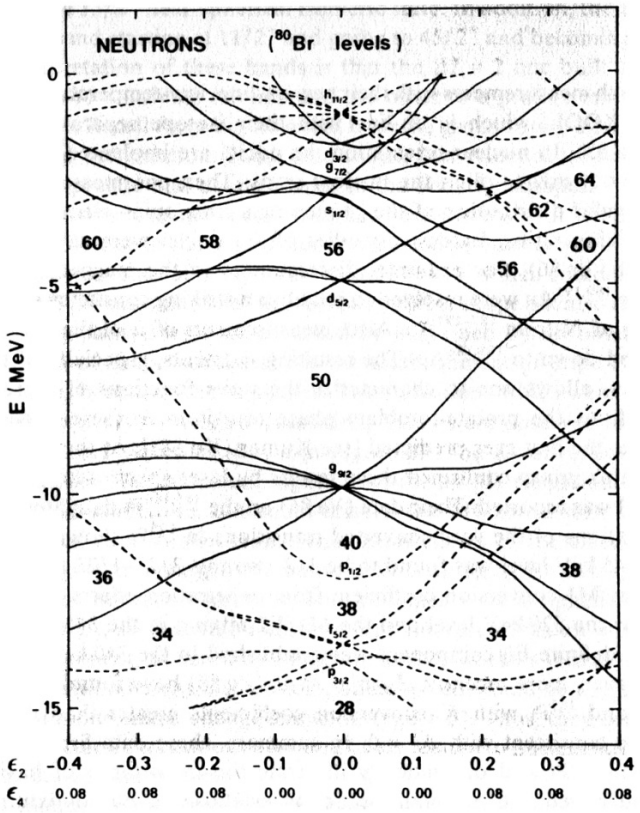

Figure 31: Single particle energy levels showing shell gaps at high deformation (Z = 38, 40 and N = 60, 62, 64) [Ham89]

Theoretical calculations of the β_2 values for ^{102,104}Zr and ^{152}Ce were carried out at Vanderbilt. The Hartree-Fock-Bogoliubov (HFB) equations were solved for the mean field and pairing field in coordinate space using the Vanderbilt HFB code [Ter03]. This code was specifically designed to study ground state properties of deformed axially symmetric nuclei far from stability. The calculation was solved on a two-dimensional grid in cylindrical coordinates using a Basis-Spline representation of wavefunctions and operators. The numerical mesh extends from 0 to 18 fm in the radial direction and from -18 to +18 fm along the axis of cylindrical symmetry. Angular momentum states up to

Ω_{max} = 21/2 and quasi-particle states up to 60 MeV were taken into account. Further details may be found in [Ter03]. The theoretical β_2 values were found to be 0.43 for ^{102}Zr, 0.45 for ^{104}Zr, and 0.32 for ^{152}Ce. This can be compared to our results of β_2 = 0.32, 0.43, and 0.43 respectively. While not in perfect agreement, there is strong evidence for the super deformation of ^{104}Zr and a strong deformation in ^{152}Ce as well.

These improved half-life measurements improve our ability to map out these deformed regions. By updating decades-old results, the regional systematics can be re-examined. The technique is also applicable to many other cases. With over 100 populated nuclei in our data sets, there will be a great deal of room for further studies to probe the deformations of more exotic neutron-rich nuclei.

CHAPTER V

EXCITED LEVELS IN ^{113,115,117}PD

Introduction

As experimental equipment and techniques have become more and more sophisticated, our ability to probe nuclear structure has advanced as well. We are able to study neutron-rich nuclei from SF of ^{252}Cf with greater and greater detail. Often re-visiting a previously studied nucleus can lead to surprising and interesting results. One area of recent interest has been the region just beyond the subshell closure at N=64 in the neutron-rich nuclei.

The lighter odd-A ^{109,111}Pd nuclei have prolate ground state deformations [Kut98]. Theoretical calculations suggest a gradual shift to an oblate deformation beyond ^{111}Pd [Mol95]. Some recent experiments in the region have found evidence for yrast structures in ^{113,115,117}Pd that indicate continued prolate deformation ([Hou99], [Kru99], [Zha99]). These nuclei exhibit rotational bands that arise from a prolate nuclear shape. It is believed that the $h_{11/2}$ neutron shell is an important factor in this behavior, and a new study with our high statistics data provides a better understanding of the structure in these Pd nuclei.

Previous studies

These nuclei have been studied with γ-ray spectroscopy from fission studies as well as beta decay experiments. The beta decay experiments have probed the ground

states and levels in the positive parity ground bands ([Fog90], [Pen91], [Pen93]). They also identified an isomeric level in each of ^{113}Pd, ^{115}Pd, and ^{117}Pd. The fission studies were able to identify rotational bands in each of the nuclei ([Hou99], [Kru99], [Zha99]). These were constructed with negative parity states built on these isomers. The isomeric level in each nucleus was assigned a spin and parity (J^{π}) of $11/2^-$. This assignment was largely based on the presence of the $h_{11/2}$ neutron that was presumed to be the source of this negative parity band. All experiments are in agreement for levels in the odd-A series of Pd nuclei up through ^{111}Pd.

^{113}Pd

There is a disagreement in the J^{π} of the isomeric state in this nucleus. Two of the reports assign $11/2^-$ as the isomer, with a rotational band constructed above ([Kru99] and [Zha99]). The other fission experiment places the rotational band on an $11/2^-$ side band, with a J^{π} of $9/2^-$ for the isomer [Hou99]. The original work assigned $9/2^-$ to the isomer [Pen93].

The beta decay experiment is quite conclusive. The ground state of ^{113}Pd is observed to decay to a $7/2^+$ excited state in ^{113}Ag with a 75% branching ratio as shown in Figure 32 [Fog87]. The log *ft* value of 5.4 indicates the transition is a pure Gamow-Teller transition. This indicates the parent state, which is the ground state in ^{113}Pd, has a J^{π} of $5/2^+$.

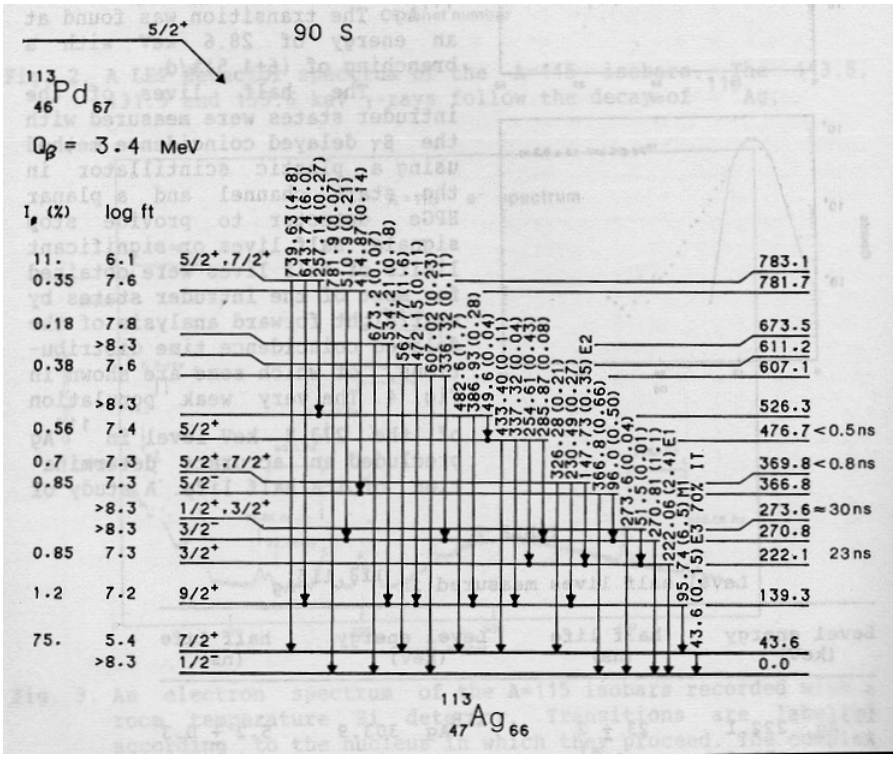

Figure 32: Beta decay of ^{113}Pd [Fog87]

^{115}Pd

In all previous experiments, the negative parity rotational band was built on the isomeric state in ^{115}Pd ([Hou99], [Kru99], [Zha99]). This state is assigned a J^{π} of $11/2^-$. The beta decay experiments provide additional insight about the isomer. The isomeric level at 89.3 keV is observed to decay to an excited state in ^{115}Ag in Figure 33 [Fog90]. This excited state subsequently decays by an electromagnetic transition to the $1/2^-$ ground state. This is highly unusual, as the highest spin we would expect for a level that decays to a $1/2^-$ state would be $5/2^-$. That would then indicate the isomeric parent state in ^{115}Pd should not have a spin higher than 7/2.

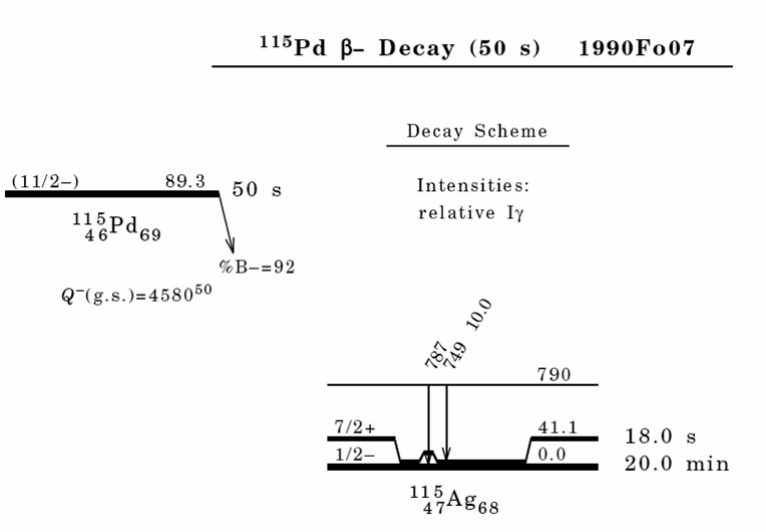

Figure 33: Beta decay of ^{115}Pd [Fog90]

^{117}Pd

A negative parity rotational band is built on the $11/2^-$ isomeric state in previous work [Zha99]. The beta decay experiment measured the conversion coefficients for transitions below the isomeric state ([Pen 90] and [Pen91]). From beta decay of ^{117}Rh, conversion coefficient measurements of transitions between excited positive parity levels and the ground state led to an assignment of $11/2^-$ for the J^π of the isomer. The ground state was assigned a J^π of either $3/2^+$ or $5/2^+$. In Figure 34, the beta decay scheme from [Pen91] is shown with a tentative $5/2^+$ ground state.

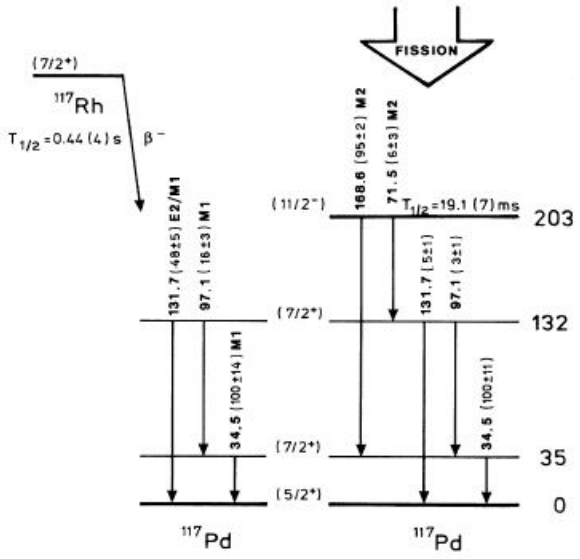

Figure 34: Beta decay of ^{117}Rh [Pen91]

Systematics

Examining the systematics of this series, we can understand the previous J^{π} assignments. Each of the odd-A nuclei from $^{97\text{-}117}$Pd are assigned a $5/2^{+}$ ground state. With that as an assumed starting point, the isomeric state can easily have a J^{π} of $11/2^{-}$. Recall the estimates of level half-lives based on transition multipolarity. The higher the order of the transition required to de-excite a level, the longer the half-life. Also, a change in parity tends to lead to a longer half-life. An isomeric state is defined as having a long half-life, so it seems logical to assign a negative parity and a spin of more than 2 units greater than 5/2 for these isomeric states.

The reason a J^{π} of $11/2^{-}$ seems favorable can be understood by examining the nuclear shell structure in the region. The negative parity states are believed to come from the $h_{11/2}$ neutron shell. Recall the single particle levels in Figure 31. For a deformation

range of $\beta_2 \sim 0.15 - 0.25$, neutrons above N = 60 occupy the $h_{11/2}$ orbital. The transitions found in fission work were assigned to form decoupled rotational bands. These rotational bands would proceed upward from the $11/2^-$ band head. Therefore, assigning a J^π of $11/2^-$ to the isomeric state and placing the negative parity rotational band above the isomer presents the most consistent picture. The negative parity systematics in the odd-A Pd nuclei are shown to appear self-consistent in Figure 35.

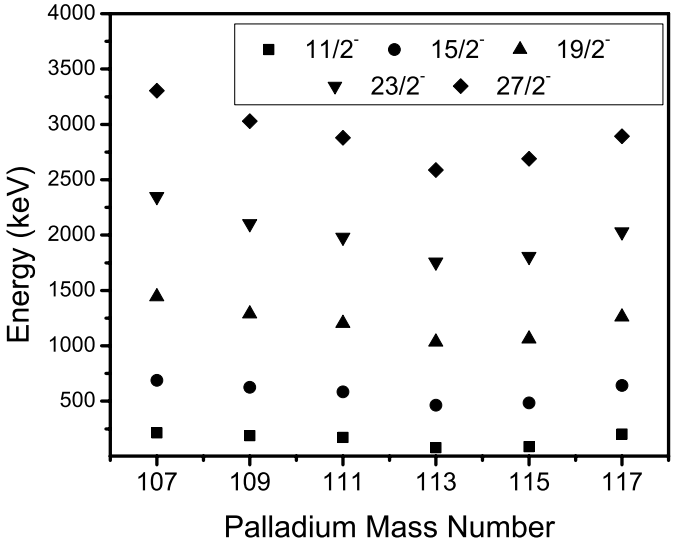

Figure 35: Previous odd-A Pd negative parity systematics

Experimental details

Our new analysis of these Pd nuclei uses the SF data from the 2000 experiment at LBNL. The γ-γ-γ cube was constructed with low channel compression and a low energy threshold of ~35 keV. This allowed us to examine closely spaced peaks in more detail and study the low energy region of the spectrum that had previously been unavailable.

With the low energy part of the spectrum available, new transitions were found in the negative parity cascade for each of the nuclei. These were completely unexpected, as none of the other experiments had reported them. As can be seen in a double gate on transitions in the negative parity band in ^{117}Pd, a new low energy transition is strikingly intense (Figure 36). The top spectrum shows the appearance of a 63.7 keV transition along with the other transitions in the negative parity band (617.9 and 863.9 keV). The bottom spectrum has a double gate set on the new 63.7 keV transition and one of the transitions from the top spectrum. The other transitions in cascade are clearly seen.

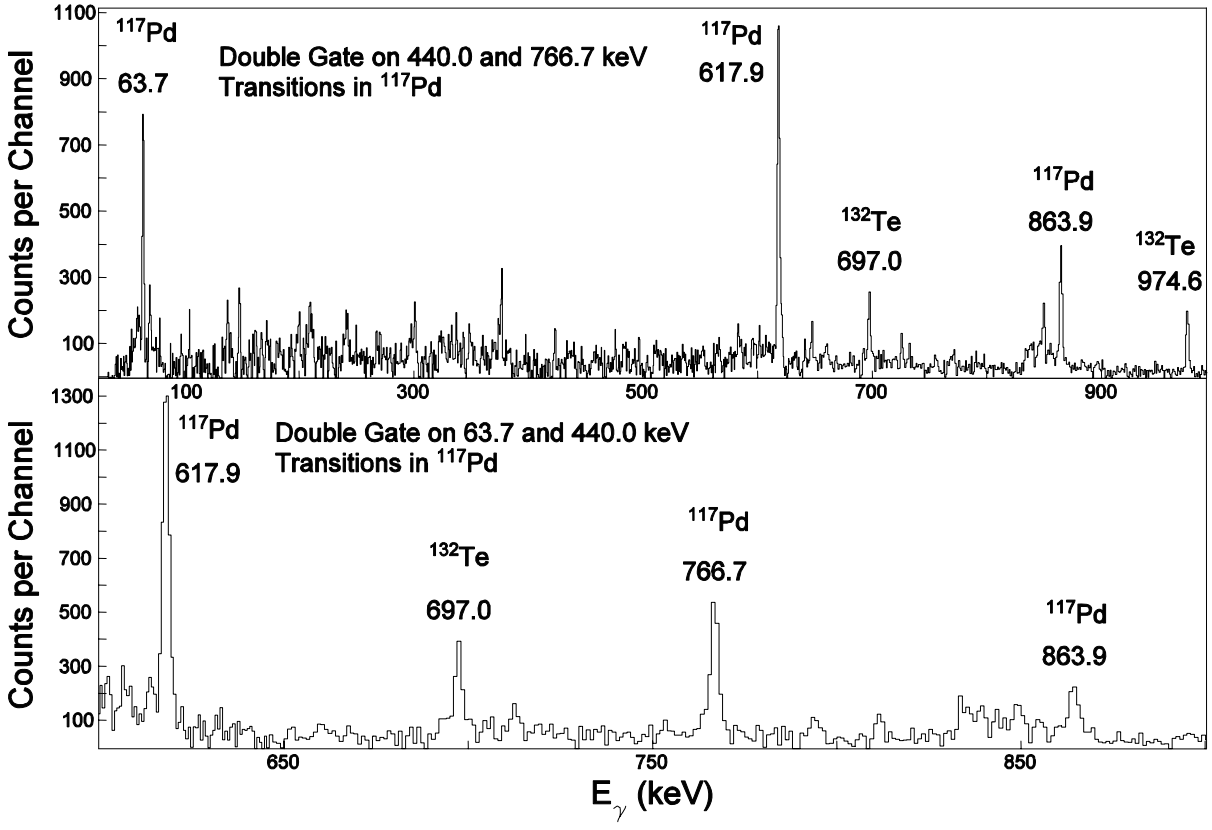

Figure 36: Top spectrum has a double gate on two known transitions in the negative parity band of ^{117}Pd. Note the strong new 63.7 keV transition. The bottom spectrum has a double gate with one common transition and the new 63.7 keV transition.

The low energy transition appears strongly coincident with all the known transitions in the negative parity band. Based on intensity measurements, it is placed directly below the previously known transitions.

In ^{115}Pd, two new low energy transitions were found (39.0 and 49.0 keV). Both were placed in cascade below the existing transitions. In ^{113}Pd, a low energy transition was found with energy 85.1 keV. These transitions greatly change the nature of the level schemes in the negative parity bands and require a re-examination of the entire structure.

Discrepancy with concurrent paper

While this analysis was being prepared for presentation at the November 2004 Southeastern Section of the American Physical Society meeting, a concurrent report was published. This study also examined the structure of ^{115,117}Pd and presents many of the same results [Urb04]. However, in ^{115}Pd, there is a disagreement in the placement of transitions and assignment of J^{π}.

The Urban et al. group places the 39.0 and 49.0 keV transitions in ^{115}Pd in parallel [Urb04]. They report no coincidence between the two. This leads them to conclude that the ground state J^{π} is $3/2^{+}$. Taking a closer look at our data, we find compelling evidence that the 39.0 and 49.0 keV transitions are indeed in coincidence. The intensities of the peaks are low because of the low efficiency of detection at such low energies. But in the spectrum shown in Figure 37, the 39.0 keV peak can clearly be observed standing above background in a double gate on the 49.0 keV and another transition in ^{115}Pd. The inset

shows the low energy range in more detail. Notice this is just above the low energy threshold of 35 keV.

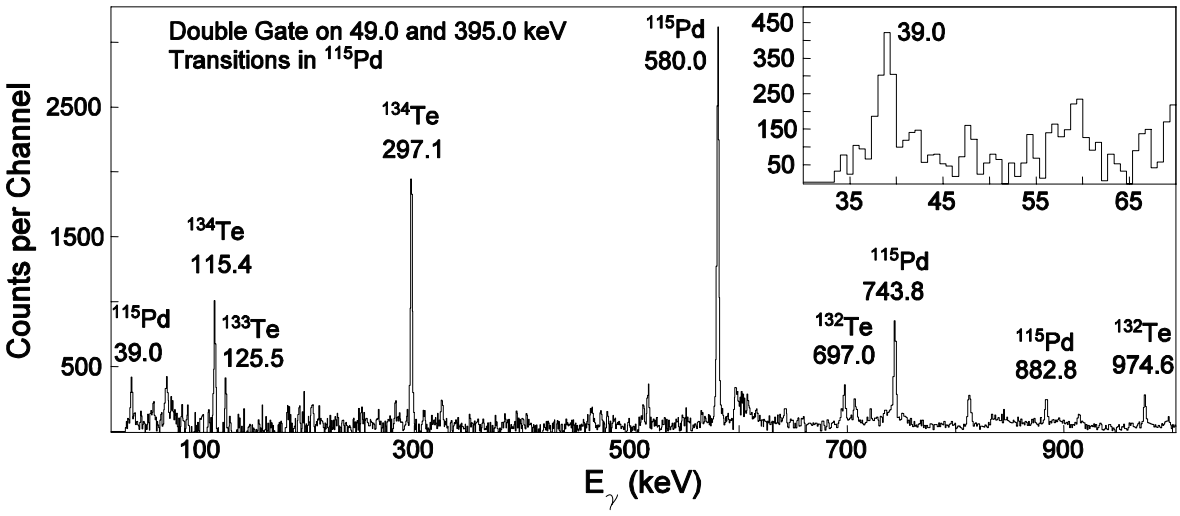

Figure 37: Double gate in ^{115}Pd showing coincidence relation between 39.0 and 49.0 keV transitions

New level schemes

The discovery of these new low energy transitions requires revising the level schemes of these Pd nuclei. While in principle, the addition could be done by simply inserting the low energy transition(s) at the bottom of the cascade, this approach was ruled out. The negative parity bands as previously understood were interpreted as rotational bands. This interpretation still appears correct, but this would strongly indicate the band should begin at an $11/2^-$ level. If we insert the low energy transition, the spins of all the levels in the band must shift up at least one unit of angular momentum. This would lead to the decoupled rotational band being built on $13/2^-$ or $15/2^-$ states which would be difficult to explain.

Our conclusion was that in addition to inserting the low energy transitions into the negative parity cascades, some of the positive parity structures also must be re-examined. Changing the J^{π} assignments of the ground state and isomeric state lead to much more self-consistent level schemes for each of these nuclei.

^{113}Pd

The new low energy transition in ^{113}Pd is 85.1 keV. This is placed above the isomeric state, with the other negative parity levels shifted up by 85.1 keV. The ground state J^{π} is left as $5/2^{+}$. The isomeric state is assigned a J^{π} of $9/2^{-}$ with the rotational band beginning at the $11/2^{-}$ state.

Four new transitions at high energy were also found, and assigned to a negative parity side band. In Figure 38, the transitions new to this work are marked with an asterisk (*). Level spin and parity assignments are marked as tentative.

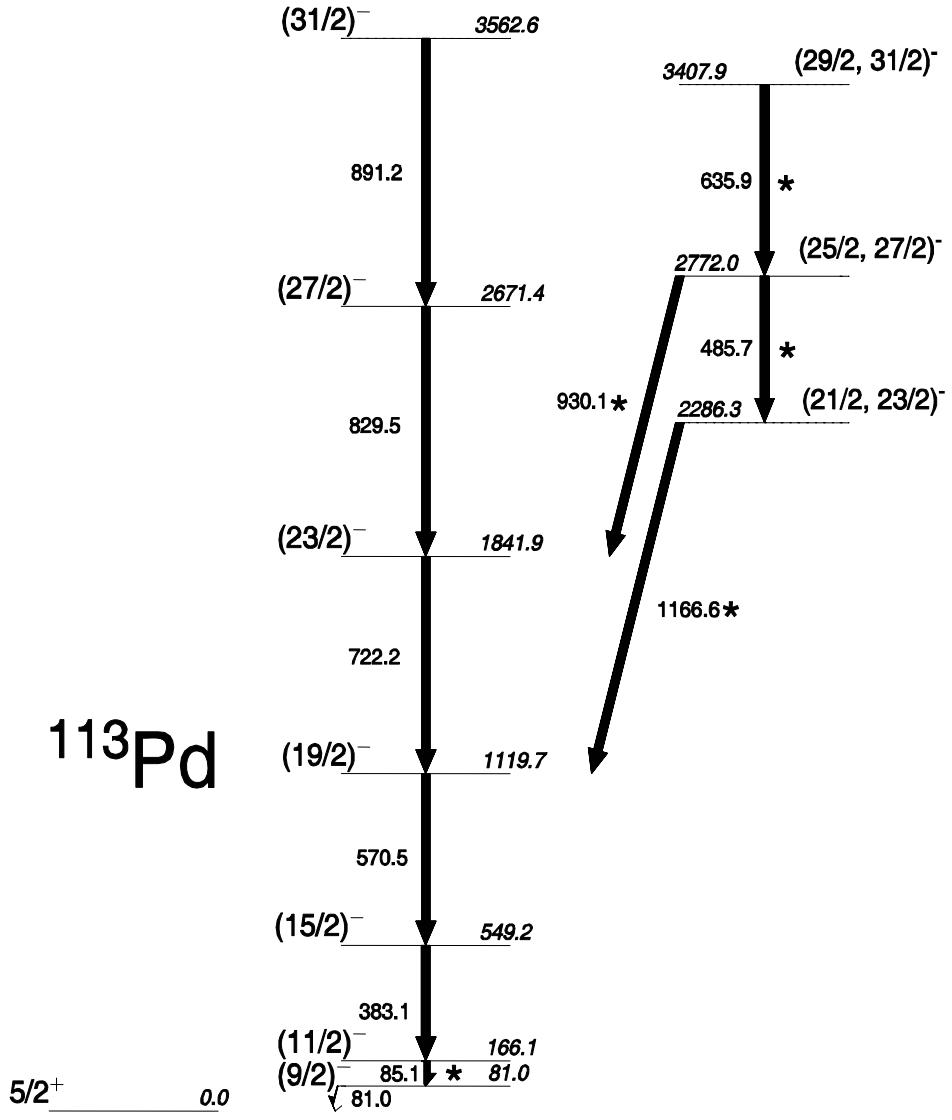

Figure 38: New scheme of negative parity levels in ^{113}Pd

^{115}Pd

In ^{115}Pd, we found two new low energy transitions of 39.0 and 49.0 keV. Since we observe them in coincidence, we place them in cascade above the isomeric state. The rotational band levels are shifted up correspondingly by 88.0 keV. The ground state and isomer spins are shifted down two units of angular momentum, to $1/2^+$ and $7/2^-$

respectively. Two new transitions of high energy are placed in a negative parity side band. These were not seen by Urban et al. The low energy levels in the Urban et al. paper are shown as well in Figure 39. The 39 and 49 keV transitions are placed in parallel, with a different J^{π} for the ground state and isomer.

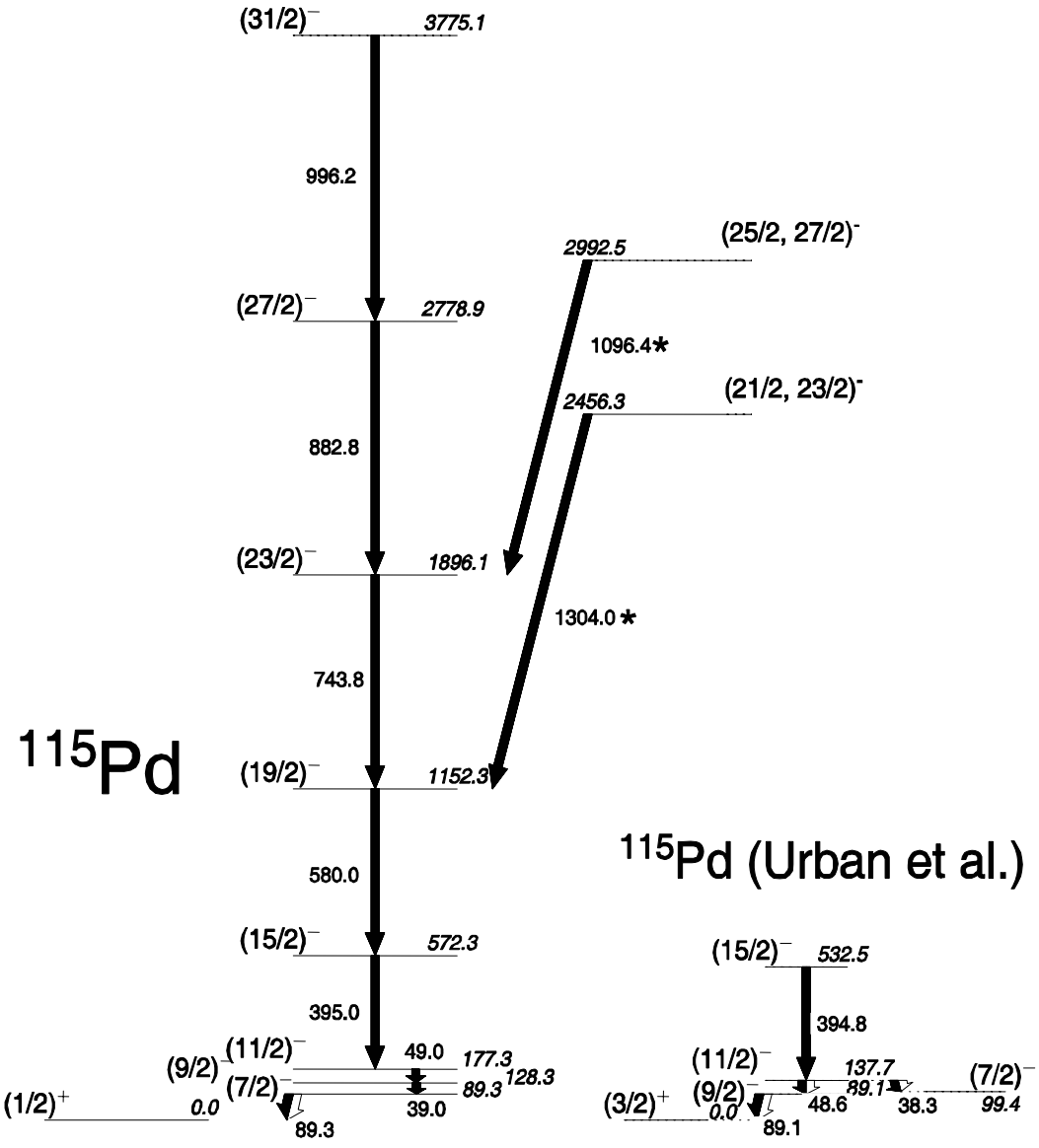

Figure 39: New scheme of negative parity levels in ^{115}Pd, with inset from [Urb04]

^{117}Pd

In ^{117}Pd, the low energy transition of 63.7 keV is placed directly above the isomeric state, shifting the rotational band levels up 63.7 keV. The J^{π} of the ground state, low lying positive parity levels, and isomer are shifted down one unit of angular momentum. Two new high energy transitions not observed by Urban et al. are placed in a negative parity side band (Figure 40).

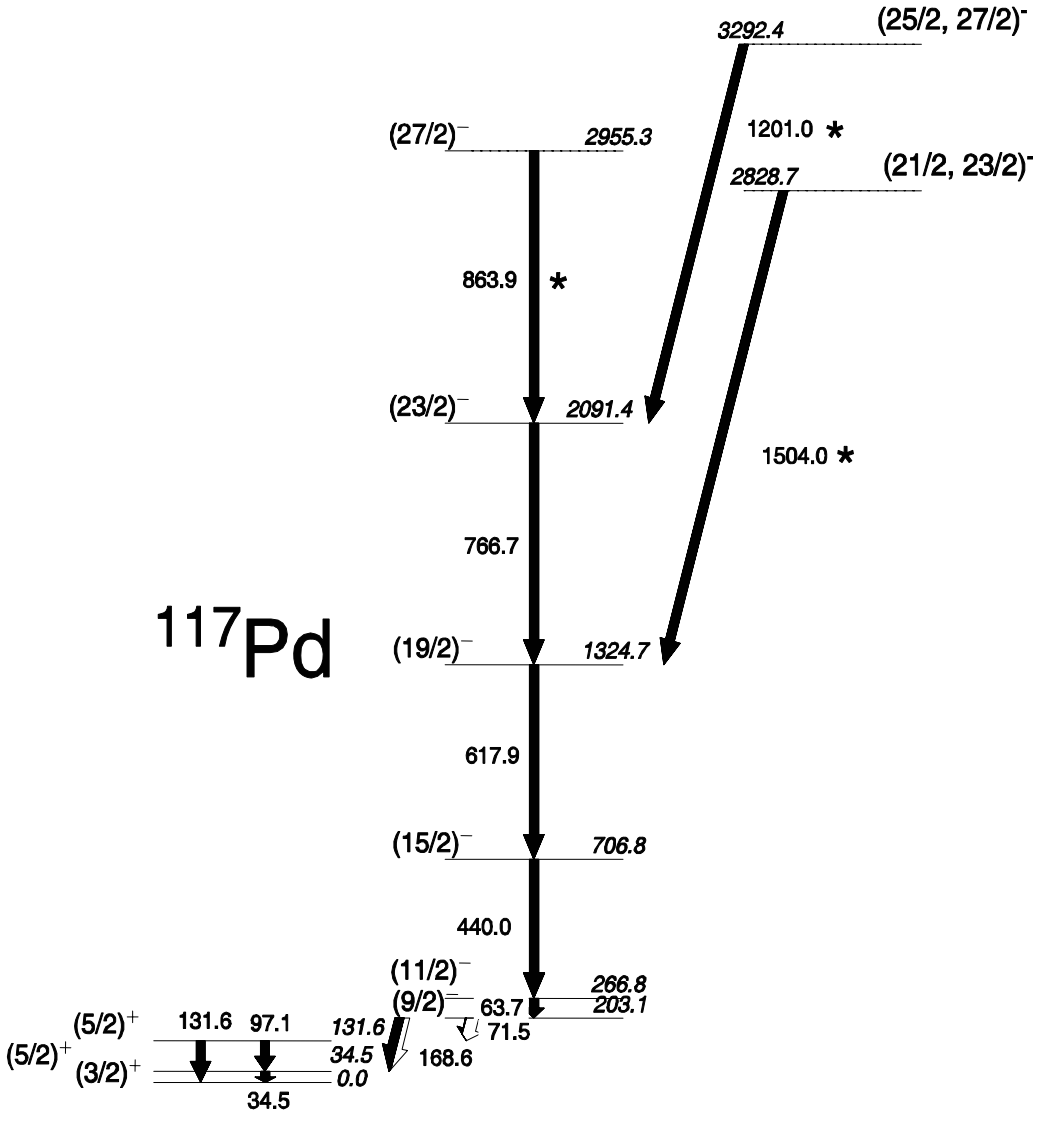

Figure 40: New scheme of negative parity levels in ^{117}Pd

Re-examination of ground states

The inclusion of the low energy transitions requires that either the rotational bands be reconsidered or the J^{π} of some of the lower energy levels be changed. The nature of the rotational band seems to be more conclusive. In addition, the negative parity side band feeds into levels with the same spin and parity for each nucleus. These facts point at the J^{π} of the ground state as the likely candidate for revision. A careful investigation of the systematics and other experiments will demonstrate whether or not this seems consistent.

^{113}Pd

The ground state is left unchanged for this nucleus. The beta decay work is very strongly supportive of a $5/2^{+}$ ground state [Fog87]. The isomeric state is changed to a J^{π} of $9/2^{-}$ instead of $11/2^{-}$. This makes the isomeric transition an M2 instead of an E3. Looking up the theoretical half-life (Weisskopf estimates) for these multipole transitions, one sees that an E3 type transition should have a half-life longer than 1 s, while an M2 type should have a half-life under 1 s. The measured half-life for the isomer is 0.3 s, which supports a M2 assignment. With this small change from the new low energy transition, all the aspects of this nucleus are consistent with each other.

^{115}Pd

The situation in ^{115}Pd is much less clear. The previous beta decay experiment seems to point to a J^{π} for the isomeric state as $7/2^{-}$. The half-life of this state is measured to be 50 s. This indicated a large change of spin between the isomer and ground state. In

fact, for such a long half-life, we would most likely expect to observe an E3 isomeric transition, making the ground state $J^{\pi} = 1/2^{+}$.

The level systematics in this region are shown in Figure 41 [Pen93]. We find strong supporting evidence for a $1/2^{+}$ ground state J^{π}. In the series of odd-A Pd nuclei, we see a $1/2^{+}$ state above the $5/2^{+}$ ground state for $^{107\text{-}113}$Pd. It descends smoothly from over 100 keV above the $5/2^{+}$ level in ^{107}Pd to only 35 keV above the $5/2^{+}$ level in ^{113}Pd. It is quite likely that the $1/2^{+}$ state descends below the $5/2^{+}$ state in ^{115}Pd, becoming the new ground state.

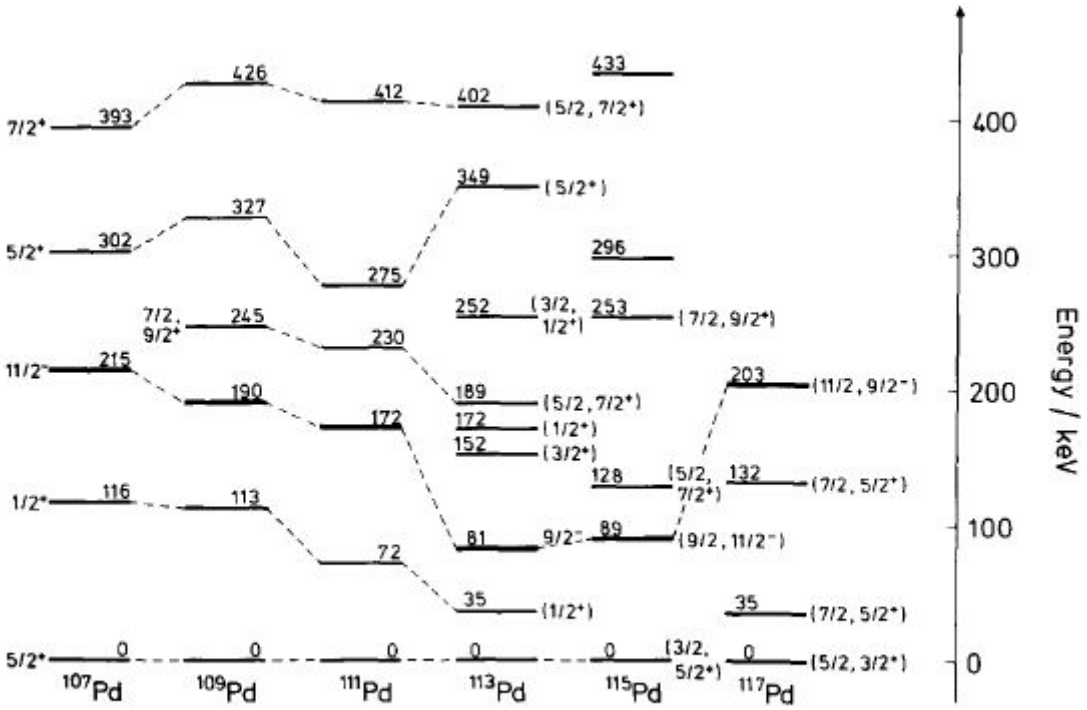

Fig. 5. The systematics of the low-lying levels in odd Pd isotopes from $A = 107$ to $A = 117$.

Figure 41: Level systematics in odd-A Pd nuclei [Pen93]

In addition, we see a strikingly similar pattern of levels in the nearby ^{123}Xe nucleus. This has the same number of neutrons (N=69), which we expect to be responsible for these negative parity states. In the level scheme of ^{123}Xe, we observe a negative parity triplet of states above a $1/2^+$ ground state. Comparing the lowest negative parity levels in ^{123}Xe with ^{115}Pd, we see the same pattern of three closely spaced levels with J^π of $7/2^-$, $9/2^-$, and $11/2^-$. The next lowest negative parity level is several hundred keV higher in energy. The ground state and three lowest negative parity levels are shown in Figure 42.

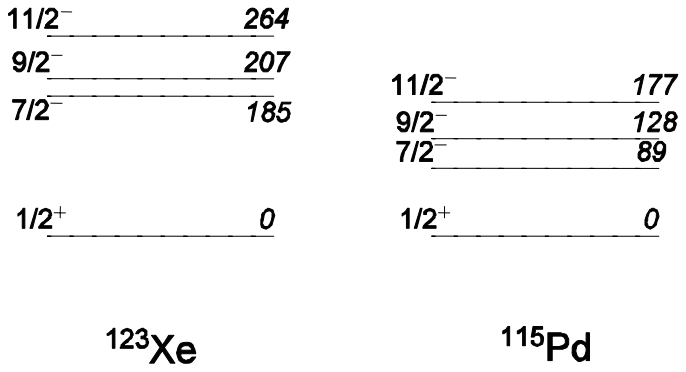

Figure 42: Comparison of negative parity levels in ^{123}Xe and ^{115}Pd

With a ground state changed to $1/2^+$, we are able to preserve the higher spin structure of ^{115}Pd. The rotational band begins at $11/2^-$ and progresses upwards, and the side band feeds into the $19/2^-$ and $23/2^-$ levels, just as in ^{113}Pd. Our ground state J^π is now in agreement with the beta decay work, and the overall picture is much improved.

^{117}Pd

The addition of the 63.7 keV transition to the level scheme does not present us with any difficulty in this case. The beta decay studies were unable to conclusively identify the J^{π} of the ground state, allowing for either a $3/2^+$ or $5/2^+$ assignment. The neighboring nuclei with the same number of neutrons (N=71) both have $3/2^+$ ground states. With our new negative parity band structures, the $3/2^+$ assignment seems very well supported, as the rotational band would again begin at $11/2^-$ and the two side band transitions feed the $19/2^-$ and $23/2^-$ states. The new level energy systematics of the negative parity levels are shown in Figure 43.

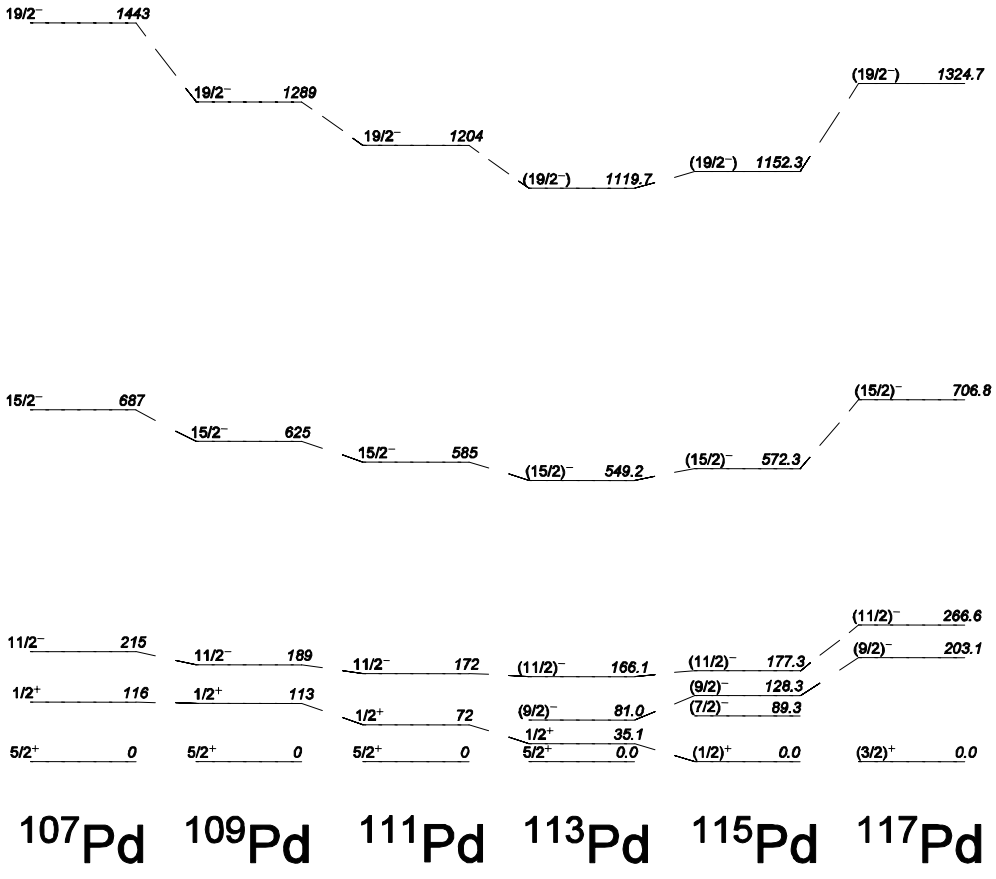

Figure 43: Negative parity levels in odd-A $^{107\text{-}117}$Pd

High spin side bands

In each nucleus, new high energy transitions were also discovered in coincidence with the negative parity bands. New levels ($21/2^-$, $25/2^-$, and $29/2^-$) were placed in high spin side bands. Three of these levels were identified in ^{113}Pd (2286.3, 2772.0, and 3407.9 keV), two were identified in ^{115}Pd (2456.3 and 2992.5 keV), and two were identified in ^{117}Pd (2828.7 and 3292.4 kev). Coincidence gates show that the side bands populate the $19/2^-$ and $23/2^-$ levels in the rotational band. This consistency supports our J^π assignments for these levels. In addition, the energy systematics follow the same trend as the other negative parity levels, descending towards a minimum at ^{113}Pd (Figure 44).

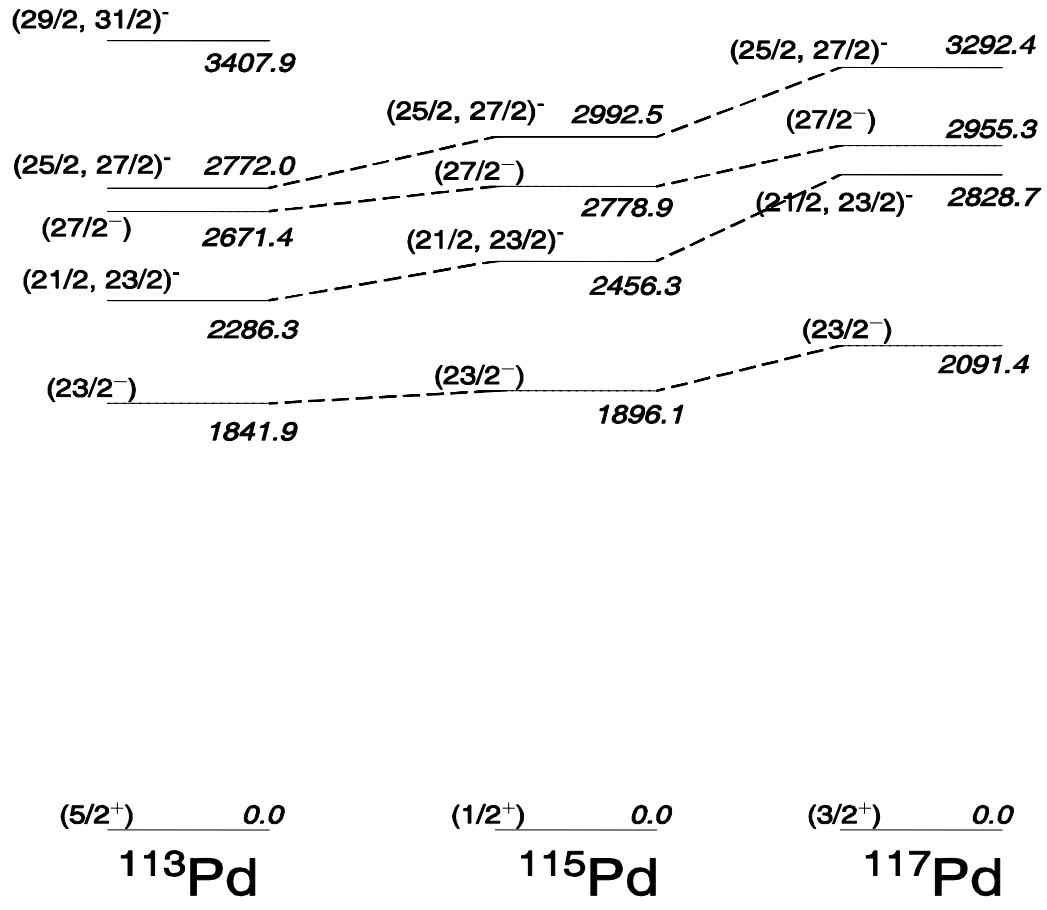

Figure 44: High spin negative parity side bands in ^{113,115,117}Pd

Conclusions

The re-examination of these odd-A Pd nuclei resulted in surprising findings. While we had hoped to extend the negative parity bands upwards in spin, we found new transitions that belonged at the bottom of these cascades. These previously unobservable low energy transitions forced a revision of the level scheme for each of these nuclei. This in turn suggested a modification to the J^{π} assignments below the rotational band.

The ground state is left as $5/2^{+}$ for ^{113}Pd while the isomer is assigned a J^{π} of $9/2^{-}$. Five new transitions are reported. The ground state in ^{115}Pd is changed to a J^{π} of $1/2^{+}$ and the isomer to $7/2^{-}$. The two low energy transitions are distinctly observed in cascade, and they connect the isomeric state to the $11/2^{-}$ rotational band head. Two new transitions are reported here, in addition to the 39.0 and 49.0 keV low energy transitions. In ^{117}Pd, the ground state is assigned a J^{π} of $3/2^{+}$ to fit the systematics. The isomer is also changed by one unit of angular momentum, to a $9/2^{-}$ state. Three new transitions are reported here, in addition to the new 63.7 keV transition.

These new results greatly change the picture of these nuclei. The ground state J^{π} is now an interesting point to study, as new levels have fallen below the 5/2+ state from lower mass nuclei. The isomerism results from levels with different J^{π} as well, and the rotational bands do not begin on these levels. These features require further study, to continue to understand the behavior of the $h_{11/2}$ neutron shell in this region.

CHAPTER VI

NEUTRON YIELDS IN BINARY AND TERNARY FISSION

Introduction

During the process of spontaneous fission, primary fission fragments are formed in an unstable state. These fragments evaporate neutrons to become excited secondary fission fragments that can be identified by their emitted γ-rays. The distribution of the final products is of course directly connected to the number of neutrons evaporated. The ^{252}Cf fission parent has exactly 154 neutrons to be distributed between the daughter fragments. By identifying both of the fragments, simple subtraction gives the number of neutrons evaporated.

This is a statistical process, governed by the excitation of the fragments. If the nucleus is formed in an excited state, it becomes unstable, and since it is neutron-rich, the nucleus "boils off" excess neutrons. The number of neutrons evaporated depends on the excitation energy of the nucleus. Early studies measured the distribution of neutrons emitted in the SF of ^{252}Cf for different charge splits and found a Gaussian shape centered between 3-4 neutrons [Hof80].

More recent studies have extended this work to measure yields of specific fission pairs, related to the advance in resolving power of detector arrays and coincidence gating techniques. The species of fission fragment is identified by detecting its characteristic γ-ray transitions. With this technique, an unusual second fission mode was found in only

one pair of fission fragments. With our high statistics γ-γ-γ data, we further investigated this hot fission mode and extended the study of neutron multiplicities to ternary fission.

Previous ^{252}Cf neutron studies

Before 1994, the only measurements of neutron multiplicities came from neutron detector experiments. These were able to measure total yields and unfolded the data with some assumptions about the expected shape of the distribution. The broad result was that the neutron multiplicity curve follows a Gaussian distribution for 1-8 neutrons, centered at 3.7 neutrons [Hof80]. Some more detailed measurements of the distribution for different mass regions were also performed, but there was no way to identify the exact species of the fragments involved in the fission.

The first study to isolate individual fission fragment pairs was done in 1994 by Ter-Akopian et al [Ter94]. By using the γ-γ-γ coincident data, the fission fragments created in the SF could be directly identified. With the atomic mass of each daughter nucleus, the missing number of neutrons can be inferred. It was found that the distributions of neutron multiplicities follow a Gaussian shape for several different individual charge-split fission partners as well as the overall ^{252}Cf yield. This is shown in Figure 45 from [Ter97].

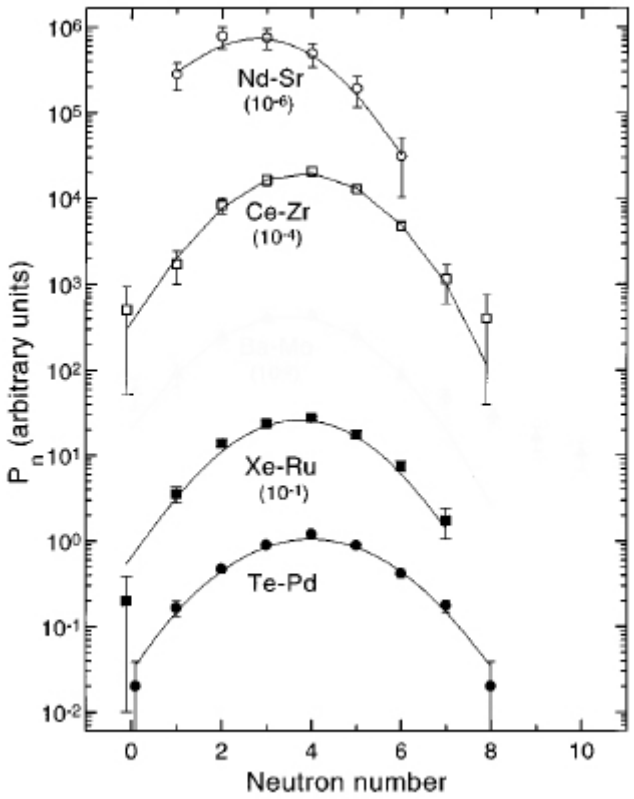

Figure 45: Previous neutron multiplicity measurements [Ter97]

However, in one (and only one) fission pairing, the distribution was observed not to follow a single Gaussian shape. In the splitting of ^{252}Cf into Ba and Mo isotopes, additional yields were measured associated with more neutrons being evaporated. Yields were found with up to 10 neutrons evaporated, where the other pairs extend only to 8 neutrons evaporated. This can be described with a two Gaussian fit, one centered between 3-4 neutrons and the second around 8 neutrons, as seen in Figure 46 from [Ter97].

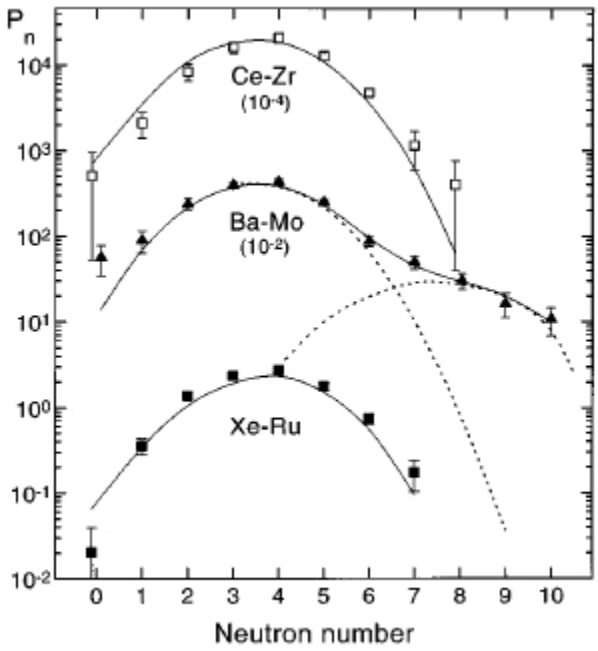

Figure 46: Previous Ba-Mo neutron multiplicity measurement [Ter97]

This result was a very surprising finding, as this Ba-Mo split was the only fission pair exhibiting this dual distribution. Two other groups investigated this peculiar phenomenon ([Bis00] and [Wu00]). They both reported a weaker intensity for the large neutron multiplicity part of the distribution. The neutron multiplicity curve from [Wu00] is shown in Figure 47, where the second Gaussian contribution is much reduced.

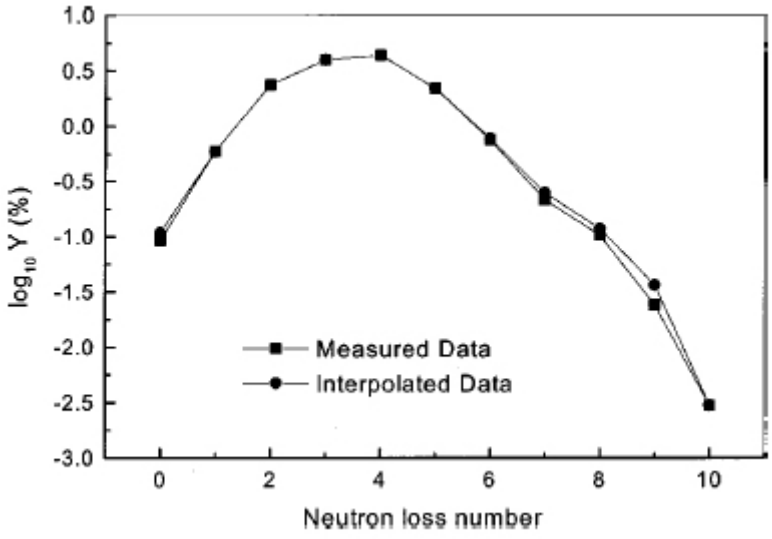

Figure 47: Ba-Mo neutron multiplicity measurement from [Wu00]

Hot fission mode

The theoretical interpretation of the two-Gaussian distribution is that a second mode of fission is involved in the Ba-Mo split. Multiple fission modes for a single nucleus have been theorized based on asymmetric deformation calculations [Pas71]. In heavy nuclei such as ^{258}Fm, ^{258}No, and ^{259,260}Md, a bimodal energy distribution has been observed [Hul86]. This was characterized by a large difference in the average total kinetic energy (<TKE>) between the two distribution groups with the new mode having a higher <TKE>.

Measurements of the fission fragment energies from SF of ^{252}Cf by Ter-Akopian et al. [Ter97] resulted in an excellent fit that yielded two such fission modes. One mode had <TKE> = 189 MeV while the other mode had <TKE>=153 MeV. The first mode corresponds to the familiar fission mode for ^{252}Cf. The second mode corresponds to events with a larger number of neutrons emitted, with an intensity for the second mode of

1/14 times that of the first mode [Ter97]. This excess internal energy indicated that one of ^{144,145,146}Ba had a hyperdeformed shape ($\beta_2 \sim 1.0$) at scission.

In simple terms, the second mode of fission is theorized to represent a fission pathway that results in a much lower kinetic energy taken up by the fragments. This in turn leads to larger internal excitation energy. The fragments that are created with more excitation energy evaporate more neutrons from their deformed shapes. A schematic of this process is shown in Figure 48.

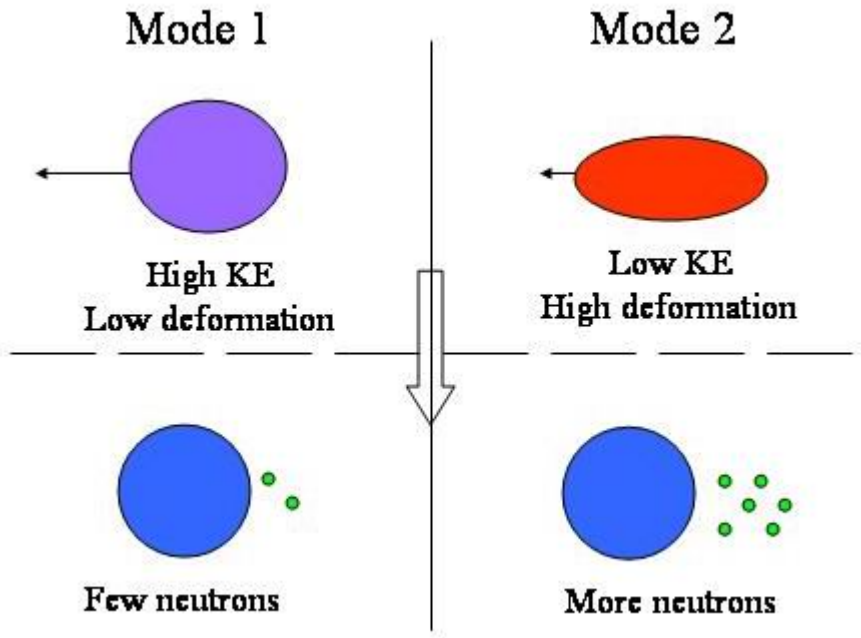

Figure 48: Schematic of two coexisting fission modes in ^{252}Cf

Measuring neutron multiplicities

To measure the neutron multiplicities for various fission splits, we used our γ-γ-γ coincidence cube to identify the γ-ray transitions in the fission fragments. These allow us to determine which pair of nuclei was created in each fission event. With this measurement, we can compare the yields from different splits. Each is associated with the number of neutrons evaporated. We then compile these results into a yield matrix that can be summed to find the total neutron multiplicity distribution.

In order to measure transition intensities from fission partners, we perform a double gate on one series of nuclei. In these gates, we will see transitions from all the partner nuclei. For example, if we choose double gates on the Xe nuclei, we will observe transitions from all the Ru nuclei in coincidence. These peaks will have different intensities according to the distribution in coincidence with our gating nucleus. As an example, in Figure 49, we have double gated on the $4^+ \Rightarrow 2^+$ and $2^+ \Rightarrow 0^+$ transitions in ^{138}Xe (483.8 and 588.9 keV).

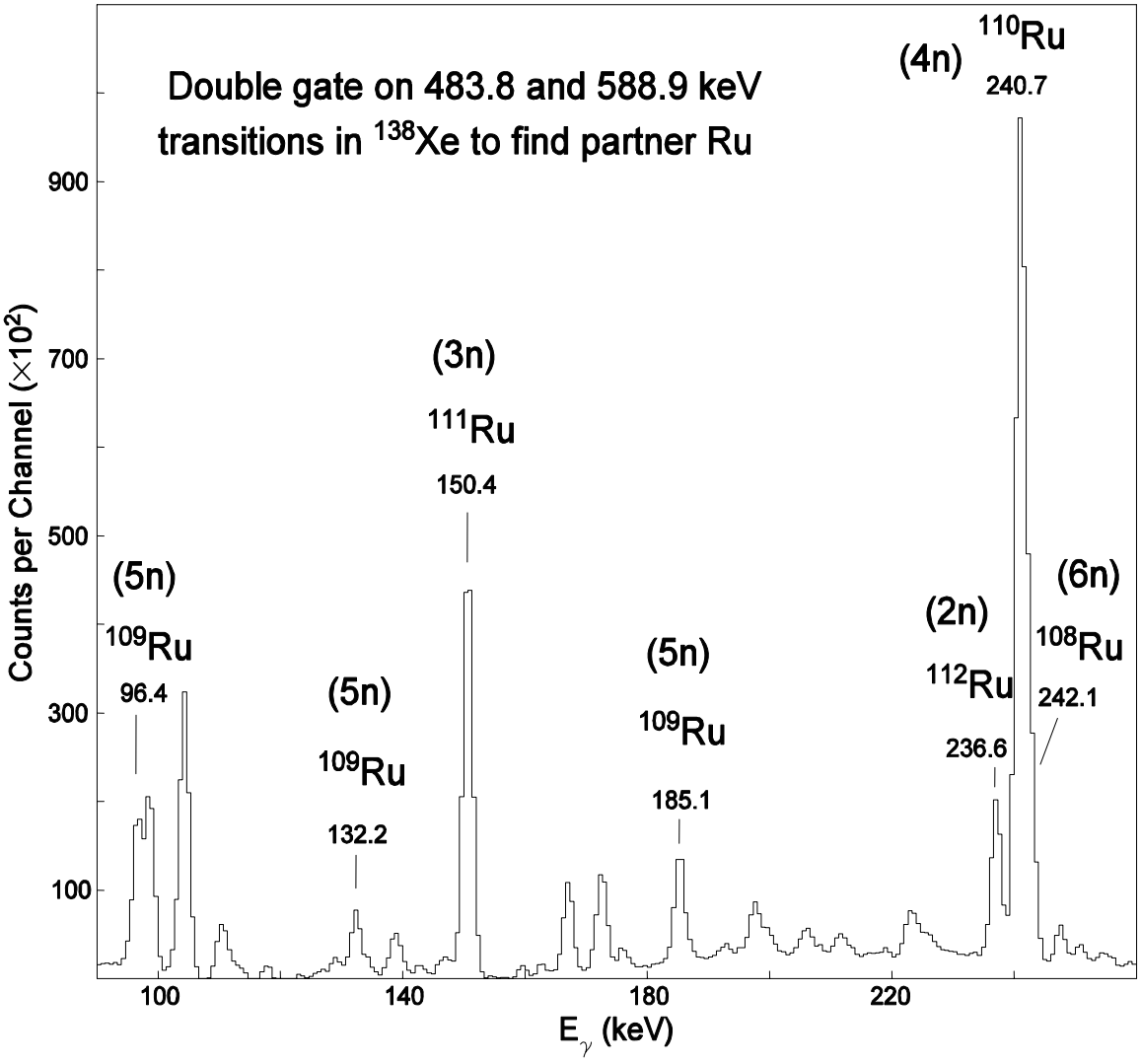

Figure 49: Sample spectrum gated on ^{138}Xe showing partner Ru nuclei

The intensities of transitions to the ground state in the partner Ru isotopes are measured. To be sure we do not miss any partner population, we sum the contributions of each transition to the ground state. This ensures that we measure every created nucleus, regardless of its de-excitation path. This is also necessary in the gating nucleus. We sum all the possible gate pairs that contain a transition to the ground state, to make sure we have gate spectra that contain all the populated fragments from the first partner.

All the peak intensities corresponding to a fission partner are measured. Efficiency and internal conversion corrections must then be applied. In some cases, a peak or gate may be contaminated by an accidental coincidence. In such cases, we rely on some of the other gates to determine the relative effect of the contamination and eliminate it. The yields are thus measured for each possible fission pair.

Once this is completed, we must normalize the yields based on the total binary fission yield. If a particular species of gate nucleus is created with less population than another gating isotope, the distribution will disproportionately favor the partners of the more-populated gate nucleus. This tends to be the case with even-even nuclei being more intensely populated than the odd-odd nuclei of the same element. For this measurement, we are concerned with the shape of the total neutron distribution summed over all possible nucleus combinations. Therefore, we normalize our measured yield for each gate nucleus to the total yield of that nucleus in binary fission. The total yield is taken from [Wah88].

New binary fission results

Analysis of our high-statistics γ-γ-γ data allows us to perform a more accurate measurement of the neutron multiplicity yield. In Table 6, the yield matrix for the Xe-Ru binary fission split is presented. The units are in events per 100 SF events.

Table 6: Neutron yield matrix for Xe-Ru

	^{106}Ru	^{107}Ru	^{108}Ru	^{109}Ru	^{110}Ru	^{111}Ru	^{112}Ru
^{136}Xe	0	0	0.007(4)	0.156(7)	0.18(1)	0.171(6)	0.216(9)
^{137}Xe	0	0	0	0.47(2)	0.88(2)	0.57(1)	0.51(1)
^{138}Xe	0.009(3)	0.036(7)	0.22(10)	0.50(2)	1.08(5)	0.438(5)	0.229(6)
^{139}Xe	0.019(7)	0.15(3)	0.73(11)	0.86(3)	1.47(6)	0.299(7)	0.082(5)
^{140}Xe	0.091(5)	0.39(1)	0.94(9)	0.68(2)	0.55(12)	0.058(2)	0
^{141}Xe	0.066(3)	0.32(1)	0.32(2)	0.148(7)	0.12(3)	0.075(3)	
^{142}Xe	0.060(2)	0.150(3)	0.120(4)	0.024(1)	0		

The compiled neutron multiplicity curve is derived from this matrix by simplying adding the components that are associated with the same number of neutrons. For instance, the yields of ^{108}Ru-^{141}Xe and ^{109}Ru-^{140}Xe are both associated with 3 neutrons evaporated in the fission. Calculating the total yield associated with each neutron channel results in the distribution found in Figure 50. The data are well fit with a single Gaussian. The zero neutron channel is not included in the fit, as it is associated with cluster radioactivity, which is an independent process.

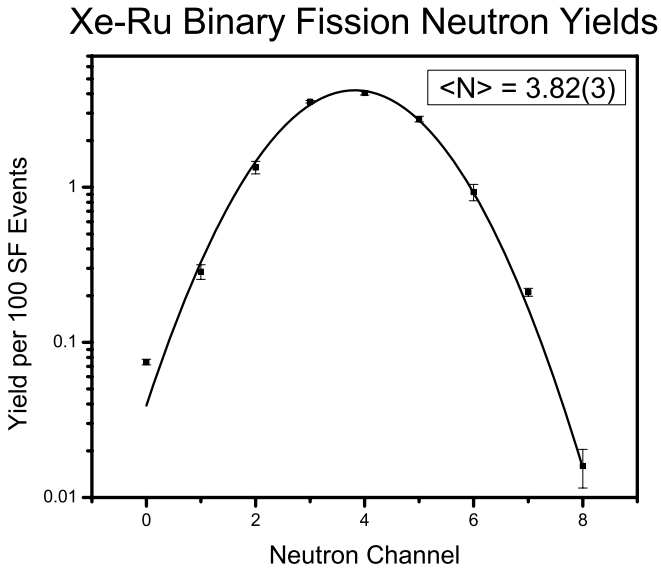

Figure 50: Xe-Ru neutron multiplicities

In Table 7, the yield matrix from the Ba-Mo split is presented. The resulting neutron multiplicity curve is shown in Figure 51.

Table 7: Neutron yield matrix for Ba-Mo

	^{102}Mo	^{103}Mo	^{104}Mo	^{105}Mo	^{106}Mo	^{107}Mo	^{108}Mo	^{109}Mo
^{138}Ba	0	0	0	0	0	0	0.012(1)	0
^{139}Ba	0	0.009(2)	0.014(1)	0	0.014(2)	0.037(4)	0.038(1)	0.011(1)
^{140}Ba	0	0.017(2)	0.010(5)	0.030(3)	0.094(5)	0.17(1)	0.162(4)	0.019(2)
^{141}Ba	0.026(2)	0.158(6)	0.146(7)	0.085(5)	0.28(1)	0.31(2)	0.19(1)	0.025(2)
^{142}Ba	0.012(3)	0.083(5)	0.220(6)	0.416(7)	0.88(4)	0.66(3)	0.36(2)	0.048(2)
^{143}Ba	0.05(1)	0.26(1)	0.64(1)	0.91(2)	1.18(3)	0.64(11)	0.081(1)	0.030(7)
^{144}Ba	0.122(5)	0.61(1)	1.28(3)	1.03(3)	0.19(3)	0.14(1)	0.06(1)	
^{145}Ba	0.198(7)	0.57(1)	0.76(1)	0.40(1)	0.21(1)	0.07(1)		
^{146}Ba	0.167(6)	0.304(6)	0.404(4)	0.102(3)	0.040(3)			
^{147}Ba	0.048(2)	0.130(4)	0.062(3)	0.018(2)				
^{148}Ba	0	0.032(3)	0.009(1)					

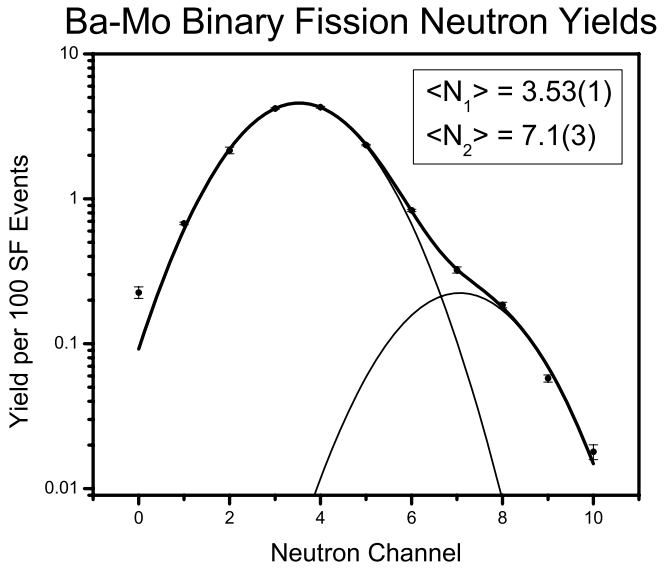

Figure 51: Ba-Mo neutron multiplicities

Discussion of binary fission neutron yield results

In the two binary fission splits studied here, the resulting neutron multiplicity curves are noticeably different. In the Xe-Ru pairing, we observe a pure single Gaussian distribution for the neutron yield. This was the expected result and verifies that the measurement technique does not have any obvious systematic abnormalities. The Ba-Mo split, on the other hand, shows clear signs of a second Gaussian shape. This is somewhat of a surprise, since the more recent analyses of ^{252}Cf data ([Biw00] and [Wu00]) showed a trend towards a weaker and weaker intensity for this second fission mode.

In the single-Gaussian Xe-Ru split, the center of the Gaussian curve is at 3.8 neutrons evaporated. In the Ba-Mo split, the dominant fission mode is centered at 3.5 neutrons evaporated, while the hot mode is centered at 7.1 neutrons. The fit was performed with the width fixed to be the same for both curves. This led to a strong fit, excluding the 0n channel that is associated with cluster radioactivity. Comparing the total yield in each mode, we find the hot mode to account for just under 5% of the yield compared to the main fission mode.

This level of yield for the hot mode is less than the original report of around 8% [Ter97]. The more recent reports by Wu et al. [Wu00] and Biswas et al. [Bis00] show very small signs of this mode, with an upper limit of perhaps 5%. In this light, our new results lie in between these two values. However, our statistics are far superior to these experiments. The Biswas experiment recorded 0.8×10^9 coincident events, while the Wu experiment recorded 9.8×10^9 coincident events. Our experimental coincidence cube was built with 5.7×10^{11} triple coincident events. This increase in statistics is reflected in the small statistical error and smooth fit in the neutron multiplicity measurement. Thus we

conclude that the "hot" fission mode is real, with an intensity on the order of 5% of the main fission mode. This hot fission is associated with a hyperdeformed shape for one of ^{144,145,146}Ba. The single particle energy levels have a shell gap at Z=56 and N = 88 for $\beta_2 \sim 1$, making ^{144}Ba possibly a doubly magic hyperdeformed nucleus at scission.

Ternary fission studies

This hot fission mode in the binary fission of ^{252}Cf led us to consider the possibility of studying the neutron yields in ternary fission. This would be the first measurement of individual neutron yield distributions in ternary fission. Our experiment in 2001 recorded 1.7×10^7 ternary events, which should provide a relatively large statistics data set for such an analysis.

In ternary fission, our coincidence measurement is defined as a light charged particle (LCP)-γ-γ event. Since the most common LCPs by far are α particles, this measurement was performed with a γ-γ matrix in coincidence with a detected α. We gate on transitions to the ground state in one fragment nucleus, and measure the intensity of transitions in the partner fragment nuclei. The yield measurement can be visualized in the following three-dimensional plot in Figure 52. One axis is for the transition energies in the gated fission fragment, and the other axis is for the transition energies of the corresponding partner fragments. The volume under each coincident peak represents the yield for that pairing. The peaks are labeled by the gating transitions. For example, Peak 1 in Figure 52 represents a gate on the $4^+ - 2^+$ transition and a gate on the $2^+ - 0^+$ transition in ^{100}Zr. These pairwise yields are then tabulated in a yield matrix and compiled according to the associated number of neutrons.

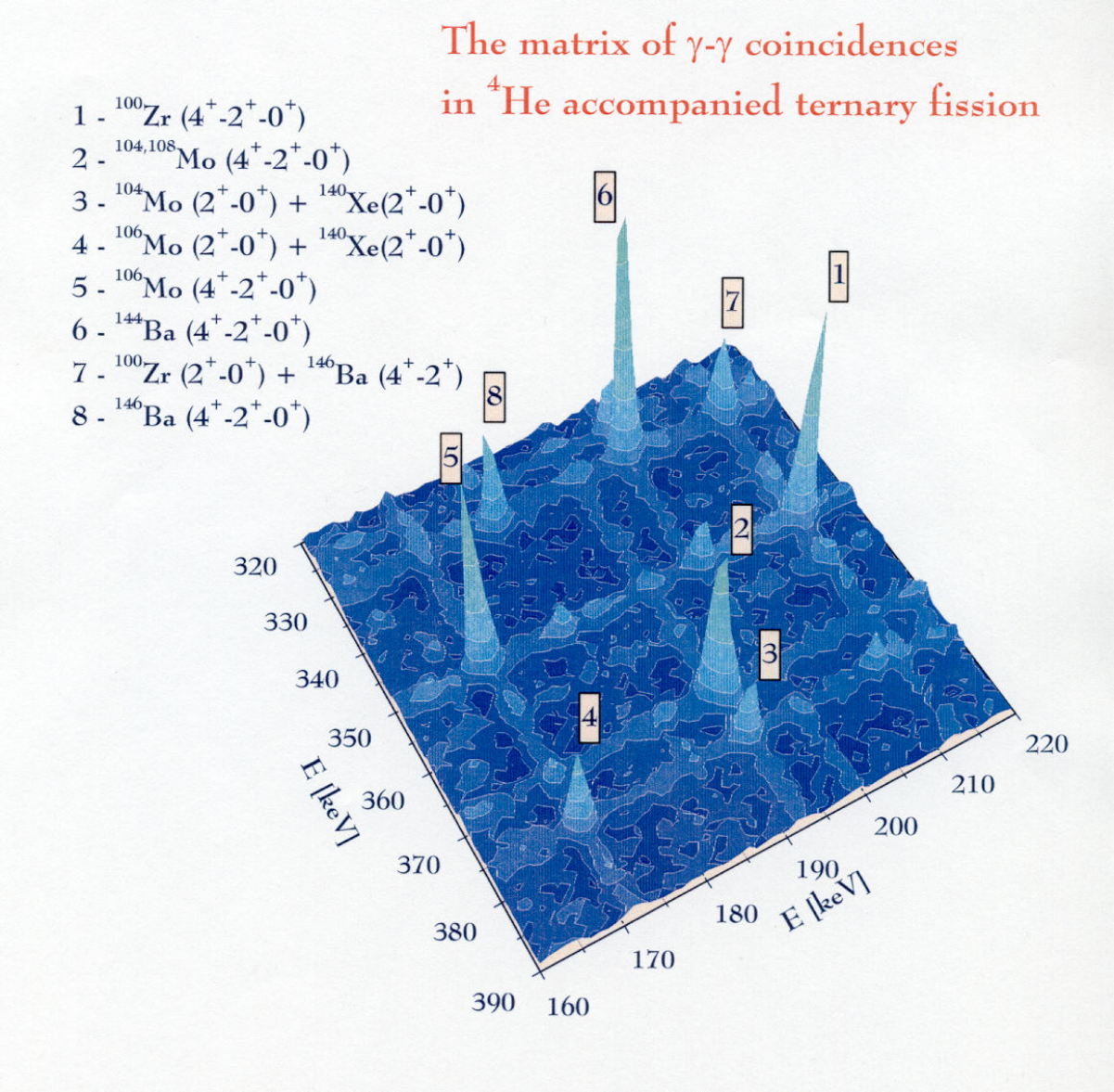

Figure 52: 3D yield intensity plot for a selected energy range in ternary fission of ^{252}Cf

New ternary fission results

Measurements were performed on three alpha ternary fission pairings: Ba-α-Zr, Xe-α-Mo, and Ru-α-Te. The yield matrix results are presented in Tables 8-10, and the resulting neutron multiplicity distributions are shown in Figures 53-55.

Table 8: Neutron yield matrix for Ba-α-Zr

	^{97}Zr	^{98}Zr	^{99}Zr	^{100}Zr	^{101}Zr	^{102}Zr	^{103}Zr	^{104}Zr
^{138}Ba	0.00	0.17(15)	0.00	1.2(4)	0.00	0.28(18)	0.5(2)	0.00
^{139}Ba	0.00	1.2(7)	0.7(2)	0.00	0.4(2)	0.4(2)	0.00	0.9(4)
^{140}Ba	0.00	0.26(15)	3.2(15)	5.10	1.8(9)	5.5(14)	0.00	0.00
^{141}Ba	0.2(1)	1.8(6)	0.00	1.9(6)	2.6(8)	7.0(19)	2.6(10)	1.0(5)
^{142}Ba	0.6(3)	0.5(3)	1.7(8)	6(2)	2.0(7)	12(3)	3.2(1.4)	3.5(14)
^{143}Ba	0.5(3)	0.6(3)	0.9(5)	3.3(13)	5.0(9)	4.9(19)	2.6(9)	0.00
^{144}Ba	0.00	1.2(6)	4.1(1.8)	15(2)	14(2)	14(2)	0.7(4)	0.00
^{145}Ba	0.00	0.7(3)	2.9(8)	11(2)	5.7(11)	1.7(9)	1.0(6)	
^{146}Ba	0.6(2)	1.8(9)	3.2(9)	12(2)	7.5(1.3)	0.00		
^{147}Ba	0.00	0.00	2.5(7)	6.1(16)	6.5(13)			
^{148}Ba	0.00	0.5(3)	5.0(13)	0.00				

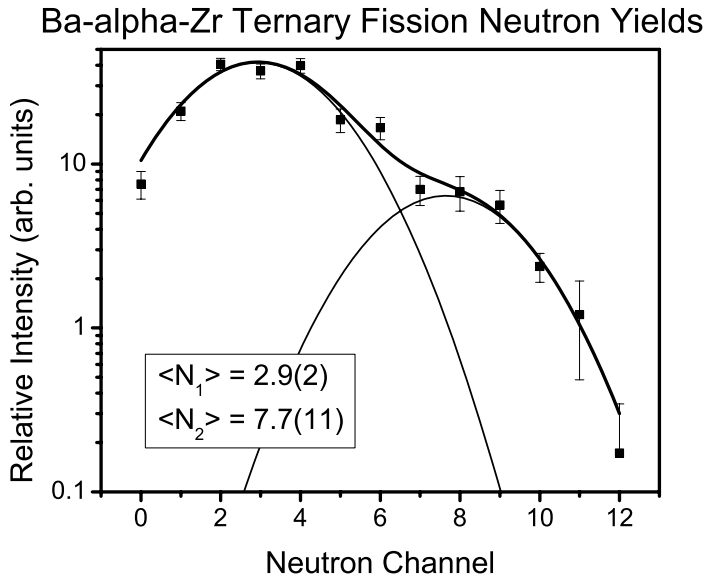

Figure 53: Ba-α-Zr neutron multiplicities

Table 9: Neutron yield matrix for Xe-α-Mo

	^{102}Mo	^{103}Mo	^{104}Mo	^{105}Mo	^{106}Mo	^{107}Mo	^{108}Mo	^{109}Mo
^{136}Xe	0	0	0.4(2)	0.22(8)	0	2.9(7)	0.8(3)	0.6(2)
^{137}Xe	0	1.0(3)	1.2(7)	0	4.7(10)	6(1)	3.7(14)	0
^{138}Xe	0	0.5(3)	8.1(27)	3.3(6)	19(3)	17(4)	15(4)	0
^{139}Xe	2.3(6)	2.5(5)	7.4(25)	6.1(11)	22(2)	18(4)	10(6)	0
^{140}Xe	0	0.8(4)	11(3)	13(3)	19(3)	2.3(9)	4.7(20)	
^{141}Xe	1.4(4)	7.2(24)	9.5(18)	4.3(9)	4.0(8)	0		
^{142}Xe	4.2(6)	3.7(11)	6.5(13)	1.0(4)	2.2(6)			

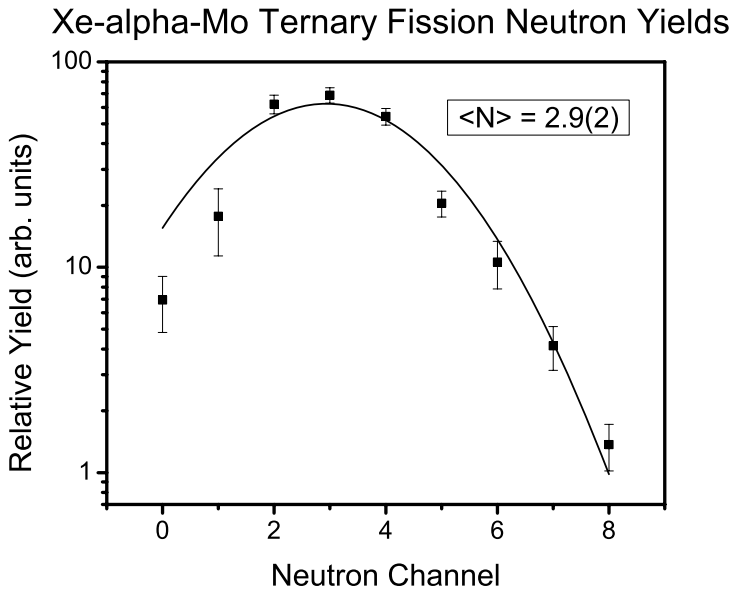

Figure 54: Xe-α-Mo neutron multiplicities

Table 10: Neutron yield matrix for Te-α-Ru

	^{106}Ru	^{107}Ru	^{108}Ru	^{109}Ru	^{110}Ru	^{111}Ru	^{112}Ru
^{132}Te	0.00	0.00	0.00	0.8(4)	1.9(7)	0.7(2)	0.19(13)
^{133}Te	0.00	0.00	0.00	1.9(4)	0.39(19)	1.1(2)	0.63(13)
^{134}Te	0.00	0.00	0.27(19)	1.6(3)	7.4(13)	2.6(3)	3.3(7)
^{135}Te	0.00	0.6(2)	1.3(7)	0.00	2.3(10)	1.5(8)	0.8(2)
^{136}Te	1.8(13)	5.6(20)	5.9(29)	5.5(17)	10(4)	3.4(17)	0.00

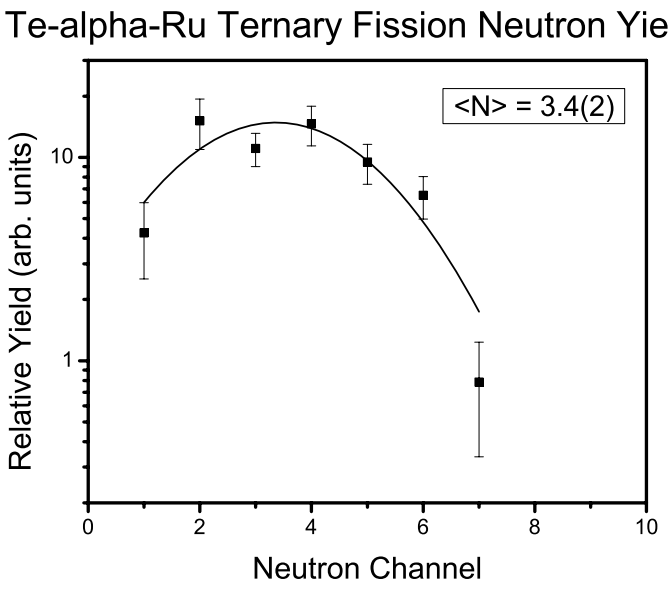

Figure 55: Te-α-Ru neutron multiplicities

Discussion

The ternary fission data set was much smaller than the binary fission γ-γ-γ cube. This results in a much larger statistical error for the measurement. The points do not fall as smoothly on the curve as in the binary fission results. This is reflected in the neutron multiplicity curves. In the binary fission distributions, the error bars are extremely small,

whereas for the ternary fission, many of the points in the distribution have rather large statistical uncertainties.

Normalization problems

However, the primary problem with the ternary fission analysis is the lack of normalization. Recall that in the binary fission measurement, the total yield of each fission fragment was normalized to the independent total yield from ^{252}Cf fission. This is impossible for α-gated ternary fission because no such total yield is known for each α-ternary pair.

Ba-α-Zr discussion

Nevertheless, we seek to explain the features that are observed in our measurement. The Ba-α-Zr split displays the two-Gaussian distribution that indicates a bi-modal fission process as seen in the binary Ba-Mo split. The first mode is centered at 2.9(2) neutrons evaporated and the second mode at 7.7(11) neutrons. The first mode is associated with less neutrons than in binary fission, where the distribution is centered between 3.5-4.0 neutrons. The hot mode has on the other hand, a higher neutron number 7.7(11) compared to the binary fission hot mode with 7.1(3), but they overlap given the uncertainties. The intensity of the second mode is approximately 15% of the first mode. This is distinctly stronger than in the binary Ba-Mo split, though the uncertainty in this result is higher. The higher intensity is related to the fact that the distribution was measured out to 12n compared to 10n in binary fission.

Xe-α-Mo discussion

In the Xe-α-Mo split, there is no indication for a second fission mode. Here, the data are fit well with a single Gaussian centered again at 2.9 neutrons. The width of the distribution is fixed to match the width in the Ba-α-Zr curve.

Te-α-Ru discussion

For the Te-α-Ru split, there appears to be no evidence for a second fission mode. There are no events associated with more than 7 neutrons evaporated, and the distribution is fit well with a single Gaussian centered at 3.4 neutrons. The width is also fixed to match that of the Ba-α-Zr curve.

Ternary fission versus binary fission

The strength of the hot second fission mode appears to be enhanced in the α-gated ternary fission. This can be explained in three ways. Remember that the heavy fissioning ^{252}Cf nucleus is on the neutron-rich side of the N=Z line. The fission products are thus created with an excess of neutrons. If we require that an α be also created, 2 less protons and 2 less neutrons are available for the larger fission fragments. This makes them more relatively neutron-rich. Consider an extreme example subtracting 80 neutrons and 80 protons from ^{252}Cf, leaving 18 protons and 74 neutrons! With more neutron-rich fragments populated in the ternary fission, it is thus likely that we would observe a higher number of neutrons evaporated.

The second explanation is based on energy considerations. Recall that the postulated hot fission mode is associated with the fission fragments being created with

low kinetic energy, allowing more energy to internally excite the nuclei into highly deformed shapes. The presence of the LCP may restrict the kinematic range of energies that can be imparted to the larger fragments. This may in turn lead to greater excitation energy and a greater number of evaporated neutrons.

Thirdly, the requirement of a ternary fission event may be creating a selection bias towards this hot fission mode. Ternary particles are associated with a highly deformed "neck" during the fission process. This larger deformation of the fissioning nucleus allows the creation of the ternary particle in the rare cases when it is produced. The greater deformation of the parent nucleus is likely to be associated with greater deformations for the fragment nuclei as well. This in turn would favor the observation of a hot fission mode.

Source of excess neutrons

In the binary fission, only the Ba-Mo split resulted in any observation of a hot fission mode. This was then interpreted as arising from a softness in the nuclear shape of one of those nuclei [Ham95]. Ba was suspected to be the source of most of this deformation. With our new ternary fission results, we are more equipped to address this question.

The Ba-α-Zr split shows a strong signature for the hot mode, while the Xe-α-Mo and Te-α-Ru show no evidence. This indicates that the effect is not likely to be an artifact of the analysis, since a systematic bias towards a high neutron mode would have resulted in a bimodal distribution for Xe-α-Mo and Te-α-Ru. The Ba nucleus does

appear to be created in two fission modes, as the hot mode appears in Ba-Mo binary fission and Ba-α-Zr ternary fission.

Conclusions

With our new ^{252}Cf fission experiments, we have revisited a surprising nuclear discovery. The hot bimodal fission first discovered in the Ba-Mo fission split was observed with higher statistics and found to exist at a 5% intensity level. Some recent papers have restricted the intensity to the level of a few percent, but our superior statistics strongly supports the positive identification of this second fission mode.

Since this hot mode is likely to be associated with larger deformation (super deformation $\beta_2 \sim 1$), the ternary fission process provides another way to examine this question. We can study different fission partners to isolate the source of the excess neutrons. By comparing Ba-α-Zr and Xe-α-Mo yields, we show that the deformation arises in the Ba nuclei and not the Mo nuclei.

The signature of this hot mode is in fact stronger in the α-gated ternary data, which may be related to the energy distribution being different in the ternary fission process. However, the lower statistics and lack of yield renormalization make the uncertainty substantial in the ternary measurement.

CHAPTER VII

SUMMARY

With several experiments using Gammasphere and a spontaneously fissioning ^{252}Cf source, we have accumulated a large amount of data for detailed nuclear structure analyses. The coincident γ-ray studies with our new higher statistics data allow for observation of previously unavailable features. This has led to new results and revisions of some previous results.

A new triple γ coincidence technique was developed to use our γ-γ-γ data to measure excited level half-lives. This is a powerful tool because in concert with our SF data, we can measure half-lives in many new nuclei. The intensity of transitions in cascade with each other will follow an exponential relationship based only on the half-life of the long-lived state in the cascade. Here we report half-lives for ^{98}Sr, ^{102}Zr, ^{137}Xe, and ^{143}Ba. These are brought into agreement with previous values using a simple correction curve.

The first measurements of the half-lives for ^{104}Zr and ^{152}Ce are reported as well (2.3 and 2.5 ns respectively). The experimental half-life results were used to calculate ground state deformations. The ^{104}Zr and ^{152}Ce nuclei have quite large super deformations ($\beta_2 = 0.43$ for both). This is attributed to shell gaps for both proton and neutron single-particle levels reinforcing one another, driving the nucleus towards large deformation.

The odd-A ^{113,115,117}Pd nuclei have been re-examined. Surprisingly, new transitions were found with high intensity at low energy (<90 keV). These fell below the low energy cutoff from previous experiments. With the discovery of these new transitions, the negative parity bands in each of these nuclei had to be revised. By examining the ground state systematics and earlier β^- decay studies, we re-assign J^π for many of the levels in these nuclei. In addition, several transitions between new high-spin levels were found.

The level scheme for ^{113}Pd has a new transition of 85.1 keV added to negative parity band, shifting the J^π of the isomeric state down by one unit of angular momentum. In ^{115}Pd, two transitions (39.0 and 49.0 keV) are discovered and found to be in prompt coincidence with each other. The ground state J^π is lowered by two units of angular momentum to bring the fission studies and β^- studies into agreement. A 63.7 keV transition was found in the cascade of ^{117}Pd. The J^π of the ground state and low-lying positive parity levels are shifted down one unit of angular momentum.

By measuring the yields of every possible correlated pair of fission fragments in certain fission splits, we are able to calculate the distribution of neutrons in binary fission. We find evidence to support a second mode of fission corresponding to a “hot” fission fragment formed with high excitation in the Ba-Mo split. This mode is centered around 7 neutrons evaporated, compared to 3 neutrons for the regular mode, and has an intensity of 5% of the regular mode. This mode does not appear in other splits, such as Xe-Ru.

Using our new ternary fission data, we performed a measurement on neutron yields in α-ternary fission. The low statistics and inability to normalize the measured yields to the independent ternary fission yields lead to substantial uncertainty in the

ternary measurements. The results for Ba-α-Zr show an enhancement of the hot mode, while Te-α-Ru and Xe-α-Mo show no evidence for the second fission mode. The intensity of the hot mode is approximately 15% for Ba-α-Zr. This result supports the theoretical conclusion that the hot fission mode is a result of super deformation in Ba nuclei.

REFERENCES

[Bis00] Biswas, D.C., Choudhury, R.K., Cinauscro, M., Fornal, B., Shetty, D.V., Vicsti, D.V., Fabris, D., Fioretto, E., Lunardon, M., Nebbia, G., Prete, G., Bazzacco, D., DePoli, M., Napoli, D.R., Ur, C.A., and Vedovato, G. (2000) Study of the Mo-Ba partition in ^{252}Cf spontaneous fission. *Eur. Phys. J. A*, **7**, 189-195.

[Bla52] Blatt, J.M., and Weisskopf, V.F. (1952) Theoretical Nuclear Physics.

[Che70] Cheifetz, E., Jared, R.C., Thompson, S.G., and Wilhelmy, J.B. (1970) Experimental Information Concerning Deformation of Neutron Rich Nuclei in the A~100 Region. *Phys. Rev. Lett*. **25**, 38-43.

[Che80] Cheifetz, E., Selic, H.A., Wolf, A., Chechik, R., and Wilhelmy, J.B. (1980) Even-even neutron-rich isotopes. *Proc. Conf. Nucl. Spectr. Fission Products*, 193-207.

[Cla74] Clark, R.G., Glendenin, L.E., Tallbert Jr., W.L., (1973) Fission Fragment Isomers from Spontaneous Fission of ^{252}Cf. *Proc. Symp. Phys. Chem. Fission, 3rd, Rochester, NY Intern. At. En. Agency, Vienna*, **2**, 221-237.

[Cot86] Cottingham, W. and Greenwood, D. (1986) An Introduction to Nuclear Physics.

[ENSDF] National Nuclear Data Center – Evaluated Nuclear Structure Data Files. http://www.nndc.bnl.gov/index.jsp

[Fir96] Firestone, R., Shirley, V., Baglin, C., Chu, S., and Zipkin, J. (1996) Table of Isotopes.

[Fog87] Fogelberg, B., Lund, B., Ye, Z., and Ekstrom, B. (1987) Transition Probabilities between Intruder Levels in Heavy Ag Isotopes. *Contrib. Proc. 5th Int .Conf. Nuclei Far from Stability, Rosseau Lake, Canada.*

[Fog90] Fogelberg, B., Zongyuan, Y., Ekstrom, B., Lund, E., Aleklett, K., and Sihver, L. (1990) Isomerism, total decay energies, and absolute γ-ray intensities of the heavy Pd and Ag isotopes. *Z. Phys. A*, **337**, 251-255.

[GAM] Gammasphere home page - http://nucalf.physics.fsu.edu/~riley/gamma/

[Ham89] Hamilton, J.H. (1989) Structures of Nuclei Far From Stability. Treatise on Heavy-Ion Science Vol. **8**. 3-98.

[Ham95] Hamilton, J.H., Ramayya, A.V., Wu, J., Ter-Akopian, G. M., Oganessian, Y.T., Cole, J. D., Rasmussen, J.O., and Stoyer, M.A. (1995) New Insights from Studies of Spontaneous Fission with Large Detector Arrays. *Prog. Part. Nucl. Phys.*, **35**, 635-704.

[Hwa04] Hwang, J.K., Ramayya, A.V., Hamilton, J.H., Fong, D., Beyer, C.J., Gore, P.M., Jones, E.F., Luo, Y.X., Rasmussen, J.O., Zhu, S.J., Wu, S.C., Lee, I.Y., Fallon, P., Stoyer, M.A., Asztalos, S.J., Ginter, T.N., Cole, J.D., Ter-Akopian, G.M., and Donangelo, R. (2004) Half-lives of several states in neutron-rich nuclei from spontaneous fission of ^{252}Cf. *Phys. Rev. C*, **69**, 057301.

[Jar74] Jared, R.C., Nifenecker, H., and Thompson, S.G. (1973) Measurements of Prompt Gamma-Ray Lifetimes of Fission Fragments of ^{252}Cf. *Proc. Symp. Phys. Chem. Fission, 3rd, Rochester, NY (1973) Intern. At. En. Agency, Vienna*, **2**, 211-219.

[Hof80] Hoffman, D.C., Ford, G.P., Balagna, J.P., and Vesser, L.R. (1980) Neutron multiplicity measurements of Cf and Fm isotopes. *Phys. Rev. C*, **21**, 637-646.

[Hou99] Houry, M., Lucas, R., Porquet, M.-G., Thiesen, C., Girod, M., Aiche, M., Aleonard, M.M., Astier, A., Barreau, G., Becker, F., Chemin, J.F., Deloncle, I., Doan, T.P., Durell, J.L., Hauschild, K., Korten, W., Le Coz, Y., Leddy, M.J., Perries, S., Redon, N., Roach, A.A., Scheurer, J.N., Smith, A.G., and Varley, B.J., (1999)
Structure of neutron rich palladium isotopes produced in heavy ion induced fission. *Eur. Phy. Jour. A* **6**, 43-48.
of ^{109,111}Pd observed in heavy-ion induced fission. *Phys. Rev. C*, **58**, 1966-1969.

[Hul86] Hulet, E.K., Wild, J.F., Dougan, R.J., Lougheed, R.W., Landrum, J.H., Dougan, A.D., Schadel, M., Hahn, R.L., Baisden, P.A., Henderson, C.M., Dupzyk, R.J., Summerer, K., and Bethune, G.R. (1986) Bimodal Symmetric Fission Observed in the Heaviest Elements. *Phys. Rev. Lett.*, **56**, 313-316.

[Kru99] Krucken, R., Asztalos, S.J., Clark, R.M., Delanque, M.A., Diamond, R.M., Fallon, P., Lee, I.Y., Macchiavelli, A.O., Schmid, G.J., Stephens, F.S., Vetter, K., and Zhang, J.Y. (1999) $\nu h^{11/2}$ bands in ^{113}Pd and ^{115}Pd. *Phys. Rev. C*, **60**, 031302.

[Kut98] Kutsarova, T., Minkova, A., Porquet, M.-G., Deloncle, I., Gueorguieva, E., Azaiez, F., Bouneau, S., Bourgeois, C., Duprat, J., Gall, B.J.P., Gautherin, C., Hoellinger, F., Lucas, R., Schulz, N., Sergolle, H., Venkova, T., and Wilson, S. (1998) Neutron $\nu h^{11/2}$ band structures

[Leo87] Leo, W. (1987) Techniques for Nuclear and Particle Physics Experiments.

[Lhe95] Lhersonneau, G., Pfeiffer, B., Huhta, M., Wohr, A., Klockl, I., Kratz, K.L., and Aysto, J. (1995) First evidence for the 2^+ level in the very neutron-rich nucleus Sr-102. *Z. Phys A*, **351**, 357-358.

[Mac89] Mach, H., Moszynski, M., Gill, R.L., Wohn,, F.K., Winger, J.A., Hill, J.C., Molnar, G., and Sistemich, K. (1989) Deformation and Shape Coexistence of 0^+ States in ^{98}Sr and ^{100}Zr. *Phys. Lett. B*, **230**, 21-26.

[Ohm87] Ohm, H., Lhersonneau, G., Sistenich, K., Pfeiffer, B., and Kratz, K.-L. (1987) The Ground-State Deformation of ^{98}Sr. *Z. Phys A*, **327**, 483.

[Pas71] Pashkevich, V.V. (1971) On the Asymmetic Deformation of Fissioning Nuclei. *Phys. Lett. A*, **169**, 275-293.

[Pen90] Penttilla, H., Aysto, J., Jauho, P., Jokinen, A., Parmonen, J.M., Taskinen, P., Eskola, K., Leino, M., Dendooven, P., and Davids, C.N. (1990) New Neutron-Rich Nuclei and Isomers Produced in Symmetric Fission. *Physica Scripta*, **T32**, 38-42.

[Pen91] Penttilla, H., Jauho, P.P., Aysto, J., Decrock, P., Dendooven, P., Huyse, M., Reusen, G., Van Duppen, P., and Wauters, J. (1991) Identification of the rare neutron-rich isotope ^{117}Rh. *Phys. Rev. C*, **44**, 935-938.

[Pen93] Pentilla, H., Enqvist, T., Jauho, P.P., Jokinen, A., Leino, M., Parmonen, J.M., Aysto, J., and Eskola, A. (1993) β-decay of ^{113}Rh and the observation of ^{113m}Pd : Isomer systematics in odd-A palladium isotopes. *Nuc. Phys. A*, **561**, 416-430.

[Rad95] Radford, D. (1995) ESCL8R and LEVIT8R: Software for interactive graphical analysis of HPGe coincidence data sets. *Nucl. Instrum. Methods Phys. Res. A*, **361**, 297-305.

[Ram89] Raman, S. et al. (1989) Predictions of B(E2; $0^+ \rightarrow 2^+$) Values. *At. Data and Nuc. Data Tables*, **42**, 2-11.

[Sch79] Schussler, F., Blachot, J., Monnand, E., Fogelberg, B., Feenstra, S.H., Van Klinken, J., Jung, G., and Wunsch, K.D. (1979) Nuclear Spectroscopy of Neutron-Rich A=143 Nuclei. *Z. Phys A*, **290**, 359-370.

[Sch80] Schussler, F., Pinston, J.A., Monnand, E., Moussa, A., Jung, G., Koglin, E., Pfeiffer, B., Janssens, R.V.F., and Van Klinken, J. (1980) Discovery of a Very Low-Lying 0^+ State in ^{98}Sr and Shape Coexistence Implication in ^{98}Sr. *Nuc. Phys. A*, **339**, 415-428.

[Ter03] Teran, E., Oberacker, V.E., and Umar, S. (2003) Axially symmetric Hartree-Fock-Bogoliubov calculations for nuclei near the drip lines. *Phys. Rev. C*, **67**, 064314.

[Ter94] Ter-Akopian, G.M., Hamilton, J.H., Oganessian, Y.T., Kormicki, J., Popeko, G.S., Daniel, A.V., Ramayya, A.V., Lu, Q., Butler-Moore, K., Ma, W.-C., Deng, J.K., Shi, D., Kliman, J., Polhorsky, V., Morhac, M., Greiner, W., Sandulescu, A., Cole, J.D., Aryaeinejad, R., Johnson, N.R., Lee, I.Y., and McGowan, F.K. (1994) Neutron Multiplicities and Yields of Correlated Za-Ce and Mo-Ba Fragment Pairs in Spontaneous Fission of ^{252}Cf. *Phys. Rev. Lett.*, **73**, 1477-1480.

[Ter96] Ter-Akopian, G.M., Hamilton, J.H., Oganessian, Y.T., Daniel, A.V., Kormicki, J., Ramayya, A.V., Popeko, G.S., Babu, B.R.S., Lu, Q.-H., Butler-Moore, K., Ma, W.-C., Cwiok, S., Nazarewicz, W., Deng, J.K., Shi, D., Kliman, J., Morhac, M., Cole, J.D., Aryaeinejad, R., Johnson, N.R., Lee, I.Y., McGowan, F.K., and Saladin, J.X. (1996) New Spontaneous Fission Mode for ^{252}Cf: Indication of Hyperdeformed ^{144,145,146}Ba at Scission. *Phys. Rev. Lett*., **77**, 32-35.

[Ter97] Ter-Akopian, G.M., Hamilton, J.H., Oganessian, Y.T., Daniel, A.V., Kormicki, J., Ramayya, A.V., Popeko, G.S., Babu, B.R.S., Lu, Q.-H., Butler-Moore, K., Ma, W.-C., Jones, E.F., Deng, J.K., Shi, D., Kliman, J., Morhac, M., Cole, J.D., Aryaeinejad, R., Johnson, N.R., Lee, I.Y., and McGowan, F.K. (1997) Yields of correlated fragment pairs in spontaneous fission of ^{252}Cf. *Phys. Rev. C*, **55**, 1146-1161.

[Urb04] – Urban, W., Zlomaniec, A., Simpson, G., Pinkston, J.A., Kurpeta, J., Rzaca-Urban, T., Durrell, J.L., Smith, A.G., Varley, B.J., Schulz, N., and Ahmad, I. (2004) New spins for ground states and isomers in ^{115}Pd and ^{117}Pd. *Eur. Phys. J*., **A**, 1-5.

[Wah88] Wahl, A. (1988) Nuclear-charge distribution and delayed-neutron yields for thermal-neutron-induced fission of ^{235}U, ^{233}U, and ^{239}Pu and for spontaneous fission of ^{252}Cf. *At. Data and Nuc. Data Tab.*, **39**, 1-156.

[Wat70] Watson, R.L., Wilhelmy, J.B., Jared, R.C., Rugge, C., Bowman, H.R., Thompson, S.G., and Rasmussen, J.O. (1970) A Study of the Low-Lying Transitions Arising from the Prompt De-excitation of Fission Fragments. *Nuc. Phys. A*, **141**, 449 - 480.

[Wu00] Wu, S.-C., Donangelo, R., Rasmussen, J.O., Daniel, A.V., Hwang, J.K., Ramayya, A.V., and Hamilton, J.H. (2000) New determination of the Ba-Mo yield matrix for ^{252}Cf. *Phys. Rev. C*, **62**, 041601.

[Wu02] Wu, S.-C., Donangelo, R., Rasmussen, J.O., Daniel, A.V., Hwang, J.K., Ramayya, A.V., and Hamilton, J.H. (2002) Resolution of complex g spectra from triple-coincidence data: Ba-Mo split in ^{252}Cf spontaneous fission. *Nucl. Instr. and Meth. A*, **480**, 776-781.

[Zha99] – Zhang, X.Q., Hamilton, J.H., Ramayaa, A.V., Zhu, S.J., Hwang, J.K., Beyer, C.J., Kormicki, J., Jones, E.F., Gore, P.M., Babu, B.R.S., Ginter, T.N., Aryaeinejad, R., Butler-Moore, K., Cole, J.D., Drigert, M.W., Jewell, J.K., Reber, E.L., Gilat, J., Rasmussen, J.O., Daniel, A.V., Oganessian, Y.T., Ter-Akopian, G.M., Ma, W.C., Vermette, P.G., Bernstein, L.A., Lougheed, R.W., Moody, K.J., and Stoyer, M.A. (1999) Identification of high spin states in neutron-rich ^{113,115,117}Pd nuclei. *Phys. Rev. C*, **61**, 014305.